Engineering Materials

Mahesh Sachithanadam
Sunil Chandrakant Joshi

# Silica Aerogel Composites

## Novel Fabrication Methods

Springer

# Engineering Materials

More information about this series at http://www.springer.com/series/4288

Mahesh Sachithanadam
Sunil Chandrakant Joshi

# Silica Aerogel Composites

## Novel Fabrication Methods

Springer

Mahesh Sachithanadam
Nanyang Technological University
Singapore
Singapore

Sunil Chandrakant Joshi
Nanyang Technological University
Singapore
Singapore

ISSN 1612-1317 ISSN 1868-1212 (electronic)
Engineering Materials
ISBN 978-981-10-0438-4 ISBN 978-981-10-0440-7 (eBook)
DOI 10.1007/978-981-10-0440-7

Library of Congress Control Number: 2015960417



Printed on acid-free paper

This Springer imprint is published by SpringerNature
The registered company is Springer Science+Business Media Singapore Pte Ltd.

# Preface

The proposed monograph is about silica aerogel composites. Silica aerogels are known for their excellent thermal insulation properties in many industrial applications. This monograph explores novel but practical approach to fabrication of silica aerogel composites so as to push their application boundaries beyond thermal insulation.

Protein-based silica aerogel composites are fabricated via inexpensive and feasible methodologies. These products exhibit polymeric foam-like behavior consisting of high compressibility, superhydrophobicity, and excellent strain recovery in addition to the low thermal conductivity and density. The fabrication methodologies are explained in detail and comprehended as flowcharts for reference. This monograph will give readers another perspective to composite fabrication other than the known traditional ones and explore the endless ways of altering the compositions to modify the properties of the silica aerogel composites. Applications of these new and novel composites could be diverse and range from pharmaceutical to aerospace to oil and gas industries.

This monograph comes with detailed schematic illustrations, experimental techniques employed, and results and predictive models to tailor a specific property for the composites. Detailed analysis of experimental results with theoretical models and numerical simulations are one of the features of this monograph. Schematic diagrams on the ductile 'phenomenon'; not usually associated with brittle silica aerogels are explained providing details on the mechanism and rationale for such material behavior. The monograph ends aptly with the study on sound absorption quality of the novel composites.

Mahesh Sachithanadam
Sunil Chandrakant Joshi

# Contents

# Abbreviations and Symbols

## Abbreviations

| | |
|---|---|
| ANOVA | Analysis of variance |
| APD | Ambient pressure drying |
| CS | Compressive strain |
| CNT | Carbon nanotubes |
| EDX | Energy dispersive X-ray spectrometer |
| EVA | Ethylene-vinyl acetate |
| FD | Freeze drying |
| FESEM | Field emission scanning electron microscopy |
| FM | Froth and mix |
| FMWNTs | COOH functionalized multiwall carbon nanotubes |
| FTIR | Fourier transform infrared spectroscopy |
| GF | Gelatin film |
| GSA | Gelatin–silica aerogel |
| HMWSP | Hydrophobic-modified water-soluble polymers |
| HSZ | High-strain zone |
| LSZ | Low-strain zone |
| PG | Porous gelatin |
| SA | Silica aerogel |
| SCD | Supercritical drying |
| SDS | Sodium dodecyl sulfate |
| SR | Strain recovery |
| Srate | Strain rate |
| STP | Standard temperature and pressure |
| TMS | Trimethylsilyl |
| XPS/ESCA | X-ray photoelectron spectroscopy/electron spectroscopy for chemical analysis |

## Symbols

| | |
|---|---|
| $\alpha$ | Acoustic absorption coefficient |
| $\lambda$ | Thermal conductivity in W/m K |
| $\theta$ | Contact angle |
| $\rho_{\text{air}}$ | Density of air at STP |
| $\rho_b$ | Bulk density |
| $\rho_S$ | Skeletal density |
| $E_f$ | Compressive modulus of foam |
| $E_s$ | Compressive modulus of solid |
| $T_m$ | Melting temperature (K) |
| $T_{\text{mean}}$ | Mean temperature between CP1 and CP3 |
| $T_g$ | Glass transition temperature (K) |
| $T_r$ | Transmission loss coefficient |
| $\dot{\text{Q}}$ | Quantity of heat flowing in watts |
| $C_{\text{th}}$ | Thermal mass |
| $c_p$ | Isobaric specific heat capacity |
| $c_{\text{air}}$ | Speed of sound in air |
| $d_i$ | Aerogel granule size |
| $z_{\text{com}}$ | Normal specific acoustic impedance |
| $Ai$ | % SDS |
| $Di$ | Density factor |
| $Ø_a$ | Aerogel material bulk property |
| $v_i$ | Sound velocity of material or medium |
| $w_i$ | Two-term weighted Gaussian function |

# Chapter 1
# Introduction

## 1.1 What Is Aerogel???

Aerogels were first discovered by an American scientist Samuel Stephens Kistler in the 1930s (Hunt et al. 1991) but the interest in these materials was renewed during 1970s and 1980s as a catalyst to enhance greener environment. These materials present enormous opportunities in the fields of engineering. Aerogels are a group of very light solid materials, highly porous and known to possess significantly higher thermal insulation properties (Rao et al. 2003). They appear as 'foam like' translucent substance referred to as "Frozen Smoke". Aerogels are intriguingly and complexly networked that contain approximately 99.98 % volume of air with a large internal surface area (Soleimani Dorcheh and Abbasi 2008). These interesting features make aerogels an ideal material for commercial and industrial applications such as thermal and acoustics insulators or for functional applications in the areas of optical, electrical and energy storing devices (Gesser and Goswami 1989; Hunt et al. 1991; Schmidt and Schwertfeger 1998; Rao et al. 2003; Soleimani Dorcheh and Abbasi 2008). Chapter 2 of this monograph primarily discusses the history and current state of aerogel technology and applications. It also touches upon the methods of aerogel fabrication such as super-critical drying and freeze drying.

Further exploitation of the silica aerogels as a viable commercial product is primarily inhibited by two factors—brittleness and volumetric shrinkage (Parmenter and Milstein 1998; Rao et al. 2003). The brittleness of the silica aerogel makes their processing and handling extremely difficult. Volumetric shrinkage occurs during production of the aerogels and it becomes more apparent at elevated temperatures (Rao et al. 2005). These limitations hinder any form of post-synthesis treatment of the aerogels, and as a result, increase difficulty to mix with other materials of interest to provide adequate mechanical properties for structural, thermal, and acoustics applications. Furthermore, the potential problem of having to compromise its ultralow density due to possible infiltration of these additional elements into the nanopores of the silica surface structure that would affect the physical and



M. Sachithanadam and S.C. Joshi, *Silica Aerogel Composites*,
Engineering Materials, DOI 10.1007/978-981-10-0440-7_1

mechanical properties (Gupta and Ricci 2008). Nevertheless, neat aerogels were extensively used in high energy physics in Cherenkov radiation detectors (Soleimani Dorcheh and Abbasi 2008) and in certain specialized applications such as catalytic supports, super capacitors, acoustic barriers and thermal insulators (Schmidt and Schwertfeger 1998).

Silica aerogels as composites with organic and inorganic materials have been researched extensively over the last decade (Capadona et al. 2006; Santos et al. 2006; Fidalgo et al. 2007; Vivod et al. 2008). These composites were prepared in the same way as monolithic aerogels except that the second constituent was added to the wet gel prior to the drying process. Thus, homogenous composites of aerogels with various polymers, metals, and other inorganic compounds are synthesized to achieve the desired properties (Capadona et al. 2006; Katti et al. 2006; Santos et al. 2006; Fidalgo et al. 2007; Xu et al. 2007). These "hybrid" composites exhibit high strength, flexibility and high modulus-to-weight ratio. However, the production of such composites is costly due to extensive equipment used and as well as long and tedious processes involved in the preparation of the aerogels (Gerard 2006).

Although, there are numerous publications on the hybrid composites, very little research on post-synthesis-binder-treated silica aerogels as composites have been conducted. One of the major hindrances in deploying binder treatment is the impact of the second constituent material on the ultralow density and low thermal conductivity of the aerogels.

This monograph covers the novel work and research carried out by the authors on binder-treated silica aerogel composites.

## 1.2 How It All Started…

This development of aerogel composites started with the basic measurements of the silica aerogel properties. Density and thermal conductivity were the key properties that were of initial interest. These granular silica aerogels were poured into hollow sandwich composite panels and evaluated for thermal properties. Over the past 4 years, the thought of developing these granular aerogels into solid blocks of composites to extend their applications played a key role in directing this research. The tedious task was to identify a suitable binder that could bond using simple techniques without compromising density and thermal conductivity of the aerogels, which proved to be a genuine challenge. Traditional composite resins and other material were trialed, but were not successful. After numerous experiments with various types of binders, gelatin, a water-soluble polymer, was selected. Upon selecting the binder, suitable fabrication methodologies were devised based on the techniques listed in the Chap. 3. Microstructural analysis, presented in Chap. 4, was performed on the constituent materials for further understanding on how gelatin was able to bind with the relatively 'inert' silica aerogels. The first composites produced showed adequate binding between the aerogel granules and gelatin.

Subsequently, other variants of gelatin–silica aerogel (GSA) composites were developed using certain additives such as SDS and CNTs to achieve specific properties. The rationale of using these additives and how they affected the composites' response in terms of mechanical, thermal and acoustics behavior are elaborated in Chaps. 5–7.

## 1.3 Uniqueness of the Book

The uniqueness of the work detailed in this monograph may be summarized as below.

(i) Use of water-soluble polymer as the route for binder treatment for producing the aerogel composites.
(ii) Establishment of a right set of processing parameters for producing aerogel-binder composites using the FD and FM fabrication techniques.
(iii) Addition of negligible amount of surfactant resulting in cellular solid-like compression behavior of binder–surfactant–aerogel composites.
(iv) Exhibition of high strain post-compression recovery in the binder–surfactant–aerogel composites, which is an unusual phenomenon associated with extremely brittle silica aerogels.
(v) Mixing a small amount of carbon nanotube as additives leading to a hydrophobic and water-repellent composite product.
(vi) Finally, the composites have shown to possess lower thermal conductivity and density as compared to the neat aerogel granules in certain configurations.

This book shall provide an excellent base for researchers who wish to study various unexplored aspects of aerogels and aerogel composites. Engineers and material scientists will also get necessary information and insight into fabrication and choice of aerogel composites, would they decide to adopt them. This shall also give rise to new applications areas for aerogel composites.

## References

Capadona, L.A., M.A.B. Meador, A. Alunni, E.F. Fabrizio, P. Vassilaras, and N. Leventis. 2006. Flexible, low-density polymer crosslinked silica aerogels. *Polymer* 47(16): 5754–5761.

Fidalgo, A., J.P.S. Farinha, J.M.G. Martinho, M.E. Rosa, and L.M. Ilharco. 2007. Hybrid silica/polymer aerogels dried at ambient pressure. *Chemistry of Materials* 19(10): 2603–2609.

Gerard, P. 2006. *Aerogel Synthesis. Catalyst Preparation*. Boca Raton: CRC Press, 31–43.

Gesser, H.D., and P.C. Goswami. 1989. Aerogels and related porous materials. *Chemical Reviews* 89(4): 765–788.

Gupta, N., and W. Ricci. 2008. Processing and compressive properties of aerogel/epoxy composites. *Journal of Materials Processing Technology* 198(1–3): 178–182.

Hunt, A. J., C. A. Jantzen and W. Cao (1991). Aerogel. A high performance insulating material at 0.1 bar. In *Insulation materials: testing and applications*, October 10, 1991–October 12, 1991, Gatlinburg, TN, USA: ASTM.

Katti, A., N. Shimpi, S. Roy, H. Lu, E.F. Fabrizio, A. Dass, L.A. Capadona, and N. Leventis. 2006. Chemical, physical, and of isocyanate cross-Linked amine-modified silica aerogels. *Chemistry of Materials* 18(2): 285–296.

Parmenter, K.E., and F. Milstein. 1998. Mechanical properties of silica aerogels. *Journal of Non-Crystalline Solids* 223(3): 179–189.

Rao, A.P., G.M. Pajonk, and A.V. Rao. 2005. Effect of preparation conditions on the physical properties of two step dried silica aerogels. *Journal of Materials Science* 40(13): 3481–3489.

Rao, A.V., M.M. Kulkarni, G.M. Pajonk, D.P. Amalnerkar, and T. Seth. 2003. Synthesis and characterization of hydrophobic silica aerogels using trimethylethoxysilane as a co-precursor. *Journal of Sol-Gel Science and Technology* 27(2): 103–109.

Santos, A., J.A. Toledo-Fernández, R. Mendoza-Serna, L. Gago-Duport, N. de la Rosa-Fox, M. Piñero, and L. Esquivias. 2006. Chemically active silica aerogel-wollastonite composites for $CO_2$ fixation by carbonation reactions. *Industrial and Engineering Chemistry Research* 46(1): 103–107.

Schmidt, M., and F. Schwertfeger. 1998. Applications for silica aerogel products. *Journal of Non-Crystalline Solids* 225: 364–368.

Soleimani Dorcheh, A., and M.H. Abbasi. 2008. Silica aerogel; properties. *Journal of Materials Processing Technology* 199(1–3): 10–26.

Vivod, S.L., M.A.B. Meador, L.A. Capadona, R.M. Sullivan, L.J. Ghosn, N. Clark and L. McCorkle. 2008. *Carbon nanofiber incorporated silica based aerogels with di-isocyanate cross-linking*. United States: 3p.

Xu, Z., L. Gan, Y. Jia, Z. Hao, M. Liu, and L. Chen. 2007. Preparation of silica-titania aerogel-like balls drying. *Journal of Sol-Gel Science and Technology* 41(3): 203–207.

# Chapter 2
# Aerogels Today

## 2.1 Introduction

The term "aerogel" is not a name associated with a specific mineral or material with a specific formula, but rather a term that encompasses certain materials with unique geometry and structure. Aerogels are a special class of nanoporous solids with complex interconnectivity and branched structure of a few nanometers. It comes in variety of forms, colors, and shapes from monolithic to powders. Aerogels have very little solid component and almost made up of 99.8 % of air which gives the product an almost ghostly appearance.

Aerogels are synthesized via sol-gel technique, where the liquid in a gel is removed above its critical temperature and pressure and replaced with air, thus forming a skeletal solid (i.e., networked structure). At the critical parameters, there is no liquid–vapor phase, and thus no surface tension present on the gel. This allows the gel matrix to remain intact without large shrinkage (Rao et al. 2005).

## 2.2 Aerogels Today

Earlier, aerogels were made from silica. In this modern era, technological advancement has made it possible to make aerogels from various materials. Alumina aerogels which appear in rust-like color were synthesized via hydrated aluminum salts, and aluminum alkoxides have tremendous potential for high-temperature storage systems and catalysts (Zu et al. 2011). Carbon aerogels are used as supercapacitors in electronic circuits and battery-powered portable device providing bridging power for days (Juzkow 2002). Aerogels have been studied as a superinsulator used in embedded garments for cold water diving by the US Navy (Nuckols et al. 2005). Similar work by Erik et al. (2006) to determine performance of aerogel blanket coupled with synthetic foam revealed having 35 % greater thermal resistance



M. Sachithanadam and S.C. Joshi, *Silica Aerogel Composites*,
Engineering Materials, DOI 10.1007/978-981-10-0440-7_2

compared with underwater pipeline insulation. Aerogels made from plants' cellulose fiber extract have shown to be flexible, transparent, and possess good mechanical toughness (Kobayashi et al. 2014). Hybrid aerogels made as a result of combining two or more constituent materials are fast creating a niche in science for specific applications. CNT-graphene composites decorated with sodium alginate have potential application in heavy metal ion detection (Wang et al. 2015). Aerogels made from chalcogens, the column of elements on the periodic table beginning with oxygen, such as sulfur, selenium, cadmium, and platinum are called chalcogels. Scientists have shown that chalcogel preferentially absorbs heavy metals and pollutants such as mercury and lead from water (Bag et al. 2007). AeroSand, a ceramic-based core material using resorcinol–formaldehyde (RF) aerogel as a binder for foundry sand (Ratke and Brück 2006) is an example of industrial application of the aerogels today. Recent works by Hong et al. (2013) on synthesizing silica aerogel with freeze cast porous zirconia ceramics revealed high compressive strength with reasonably low thermal conductivity ranging from 0.041 to 0.098 W/m-K. The varied applications in several industries from building and construction to dielectrics in integrated circuits are explicitly detailed in a review paper by Gurav et al. (2010).

## 2.3 Market Outlook

While the prospects and potential of aerogels seem exuberating, researchers are still hesitant to put these varieties of aerogels for commercial and business use. The most practical use of aerogels now is thermal insulation. Insulation materials made of aerogels are gaining popularity in the United States and the coldest regions of Europe. Besides thermal insulation, aerogels are also used for acoustic and optical insulation (Gibiat et al. 1995; Schmidt and Schwertfeger 1998) in the buildings. Allied Market Research has done an extensive coverage on the global aerogel market, which in 2013 was valued at $221.8 million. It is estimated to reach $1896.6 million by 2020 with a reported compound annual growth rate (CAGR) of 36.4 %. The report evaluated that recyclability, reusability, and fire protection will be key drivers for upswing in commercial success for the aerogels providing thinner and lighter alternatives to convectional insulation materials as described in Fig. 2.1. Koebel et al. predicted that aerogel-based thermal superinsulators market will grow more rapidly than the "conventional" insulators for at least a decade up to the point when markets will begin to saturate (Koebel et al. 2012). The main drawbacks for aerogels are the high cost of production and the ever-changing global economic conditions. Even so, with advancing methods and technology, the production cost of aerogels is expected to reduce from US$4000 to US$1500 per cubic meter (Koebel et al. 2012).

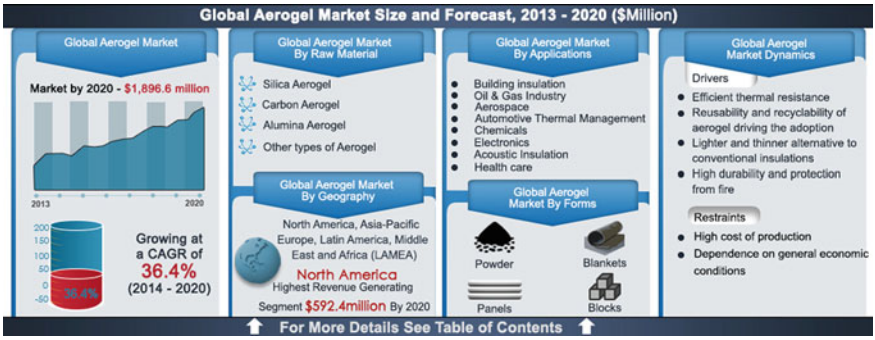


**Fig. 2.1** Global aerogel market size (*Source* Allied Market Research)

## 2.4 Silica Aerogels

Silica aerogels are probably the most researched and investigated aerogels amongst the class of aerogels. They are primarily prepared via the solution-gelation (sol-gel) chemistry technique. This technique basically involves two steps: 1) formation of the wet gel and 2) drying of the wet gel with an intermediate aging process. The first step involves hydrolysis of silicon alkoxide precursors, suitable solvents, catalysts, and water stirred into a homogenous solution (Pajonk 1998). This forms colloidal dispersion of particles and over a period of time the solution will form a three-dimensional grid of solid and liquid phases. This process is called ***gelation***. Gesser and Goswami (1989) described the process of sol-gel as shown in Fig. 2.2 in their paper in great details.

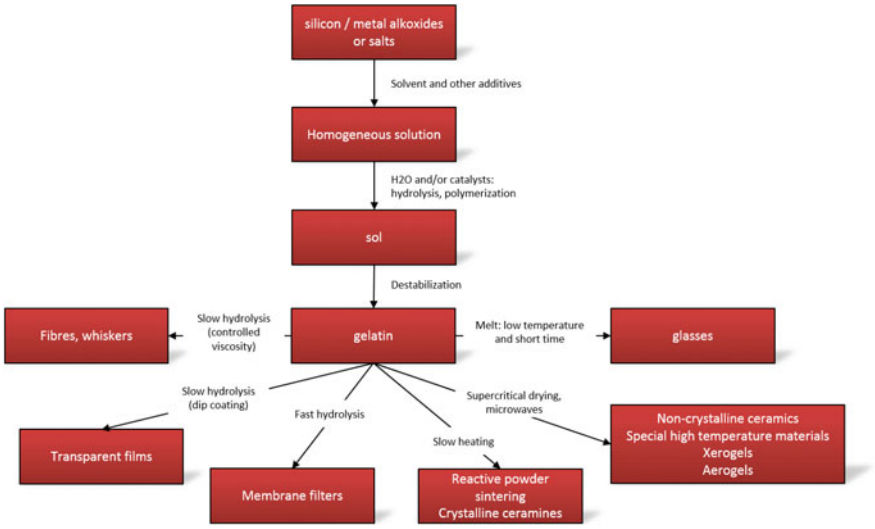


**Fig. 2.2** Sol-gel process redrawn from Gesser and Goswami (1989)

The gel formed could be of polymer chain-like or colloidal-like gel depending on the pH value of the medium used. The solvent will then be distilled leaving a viscous fluid that is redissolved in an alcohol-based liquid such as ethanol (Gerard 2006). It would take a few cycles to accomplish complete wash out of the residual solvent and water when redissolving in alcohol. The second step involves drying. This is a critical step in the making of aerogel as the properties of the material are greatly influenced by pressure and temperature as explained previously (Lee et al. 1995). This step generally purges the remaining liquid in the pores and at the same time prevents the gel structure from collapsing. Figure 2.3 explains the general steps involving the production of aerogels. The aging process can be considered as the intermediate step between gelation and drying process (Lee et al. 1995).

Over the decades since it was first discovered, researchers have studied extensively to improve the properties of the final product and as well as reduce the high cost of production by synthesizing with alternative materials (Morris et al. 1999). The evolution of the silica aerogels over the past three decades will be discussed in the following sections.

## 2.5 Evolution of Silica Aerogels

Soleimani Dorcheh and Abbasi (2008) reviewed the properties and characterization of silica aerogels since its invention in the 1930s. They had categorically written about the evolution of silica aerogels in each of the key processes and the corresponding improvements that were made in producing these aerogels safely and effectively. The flowchart in Fig. 2.3 shows the general processes involved in the synthesis of aerogels.

### *2.5.1 Formation of Wet Gel*

Silica aerogels are available in variety of forms such as powders, chunks, granulates, and others. Their properties can be customized to suit the applications required. The basis for the formation of wet gel is through hydrolysis in sol-gel technique using varying molar ratios of precursors, solvents, and catalysts.

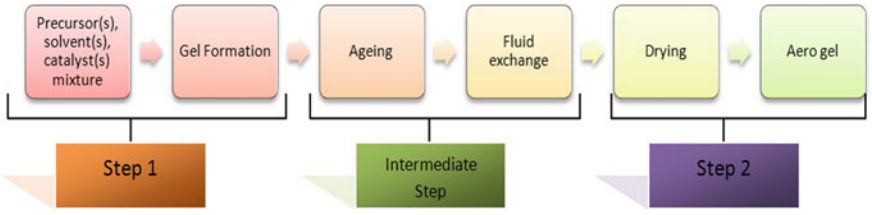


**Fig. 2.3** Overview of key processes in making aerogels

#### 2.5.1.1 Precursors, Solvents, and Catalysts

The precursors used in the sol-gel technique are mainly silicon alkoxides that possess high degree of purity. Many of these silicon derivatives are used in various types of solvents and catalysts to produce silica aerogels. Each of these produces varying degrees of physical, thermal, mechanical and optical properties in the aerogels. Some of these precursors used are Tetramethoxysilane (TMOS), tetraethoxysilane (TEOS), polyethoxydisilane (PEDS), methyltriethoxysilane (MTES), and many others (Rao et al. 2003, 2005; Soleimani Dorcheh and Abbasi 2008; Wei et al. 2011). However, they are very expensive and hazardous materials that are known to cause blindness.

The current commercial synthesis of silica aerogels is produced using water-glass (sodium silicate) solution by ambient pressure drying (Lee et al. 2002; Bhagat et al. 2007a, b). Water glass is cheap and has high stiffness and large pore size (Lee et al. 2002). Typical solvents used are ethanol, methanol, acetone, and to a small degree, ethyl acetate. Catalysts are added in the sol-gel technique to control the rate of gelation. The catalysts used in the preparation are acid catalysts, base catalysts, or two-step acid–base catalysts (Lee et al. 2002; Bhagat et al. 2007a, b, c). The pH levels and duration of gelation process needs to be monitored and controlled in order to achieve optimal results. Generally, it has been reported that base catalysts or two-step acid–base catalysts produce better quality silica aerogels in terms of uniform distributions (Lee et al. 1995), reduced shrinkage, and increased ability for cross-linking (Bhagat et al. 2007a, b).

### *2.5.2 Aging and Fluid Exchange of Wet Gel*

The "ageing" process has great influence on the microstructure, porosity, surface area, pore size, and volume shrinkage of the aerogel. The effects of prolonged aging duration and concentration were studied by various researchers (Rao et al. 2005, Bhagat and Rao 2006; Mahadik et al. 2012). The period of aging has significant effects resulting in increased optical transmittance, density, and surface area with increased strength and stiffness.

### *2.5.3 Drying*

Drying determines the nature of the final product and it is governed by surface tension of the gel. Volume shrinkage is most evident in this step as the pressure and temperature play important roles. Three types of drying method have been employed by researchers: supercritical drying (SCD), ambient pressure rying (APD) and freeze drying (FD).

#### 2.5.3.1 Supercritical Drying (SCD)

High-temperature supercritical drying (HTSCD) was first used by Kistler in 1931, and is still being used widely for silica aerogel production (Gesser and Goswami 1989, Hunt et al. 1991). HTSCD is carried out using any organic solvent such as methanol or ethanol placed in an autoclave raising the temperature slowly resulting in corresponding pressure increase.

Thereafter, the pressure is adjusted to reach above the critical pressure of the solvent and kept constant for a period of time. The solvent or fluid is then vented slowly at constant temperature resulting in pressure drop. When the ambient pressure is reached, the autoclave is cooled down to room temperature (Rao et al. 2003). The biggest disadvantage using this method is the potential fire hazard that the solvents pose due to the high operating temperature and pressure (Gerard 2006). An alternative means called low-temperature supercritical drying (LTSCD) utilizes liquid $CO_2$ since it has a critical point that is very near to the ambient temperature (Bhagat and Rao 2006, Soleimani Dorcheh and Abbasi 2008). The silica aerogels produced in this manner are less expensive but usually hydrophilic (water absorbing), though they can be modified to be hydrophobic via surface functionalization (Bhagat and Rao 2006).

#### 2.5.3.2 Ambient Pressure Drying (APD)

APD is seen with great interest as both HTSCD and LTSCD are considered relatively expensive processes. APD is a cheaper alternative process that involves surface chemical modification, manipulating the contact angle, and network strengthening with a silylating agent (Rao et al. 2005). Silylation is carried out in the water phase of gel, which involves the replacement of Si–OH groups by the hydrolytically stable Si–R (R-alkyl) groups through oxygen bond, thereby resulting in the hydrophobic aerogels (Lee et al. 2002, Rao et al. 2005, Bhagat et al. 2007a, b, c). Figure 2.4 shows the silylation process of the silica aerogel. An interesting feature of silylation is the "spring back" (Fig. 2.5) phenomenon. The trimethylsilyl (TMS) groups that are introduced during the silylation process effectively terminate further interaction between the solid structure and the solvent. Thereafter, the gel begins to shrink during

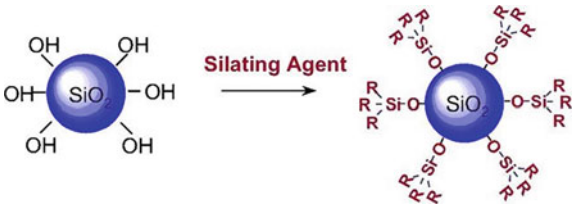


**Fig. 2.4** Silylation process of silica aerogel (Soleimani Dorcheh and Abbasi 2008)

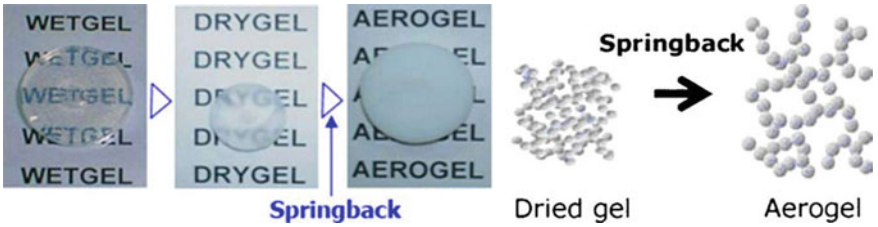


**Fig. 2.5** "Spring back" phenomenon (Rao et al. 2005)

the drying process due to capillary forces since this is treated at ambient pressure. However, when the liquid phase within the gel starts to evaporate, the chemically inert surface silyl groups prevent further infusion of liquid.

Hence, the gel is able to re-expand as shown in Fig. 2.5. Rao et al. (2005) prepared two-step acid–base ambient pressure-dried silica aerogels successfully. He reported that aerogels obtained from APD have improved properties in terms of low thermal conductivity, low density, high porosity, and high optical transmittance than aerogels produced by HTSCD.

However, the realization of finished product takes about four to seven days and require enormous amount of solvents and materials. Therefore, it is too costly for large-scale production of silica aerogels. Bhagat et al. (2007a, b) investigated the effect of using co-precursors on water-glass solution for rapid surface modification. He and his co-workers had reduced the processing time (one day) using trimethylcholorosilane (TMCS) and hexamethyldisilazane (HMDZ) on water-glass solution and reportedly showed improvement in properties such as low density and higher thermal stability of up to 500 °C (Bhagat et al. 2007a, b, c). Rao et al. (2003) investigated the effect of thermal degradation of $Si–(CH_3)_3$ groups on the surface of silica aerogels which are stable up to 325 °C.

Nevertheless, thermal stability ranges between 325 and 500 °C, beyond which the inert TMS groups on the surface will oxidize and revert back to Si–OH bonds (Rao et al. 2005; Bhagat et al. 2007c) and thus become hydrophilic. Many researchers have tried using other precursors with silylation agents to improve overall qualities of the APD processed silica aerogels, but water-glass-derived aerogels remain the best and most feasible for commercial production (Soleimani Dorcheh and Abbasi 2008).

#### 2.5.3.3 Freeze Drying (FD)

Solvents of low expansion coefficient and high sublimation pressure are usually used in FD. Similar to SCD, FD works on the principle of non-capillary pressure between the liquid and gas phase. The liquid is frozen and then sublimed under

vacuum (Arndt et al. 2007). Although this technique offers a safer route to obtaining aerogels, FD is not extensively used (Tamon et al. 2001). Hyun et al. successfully developed nanoporous silica films with low dielectric constant using the FD method (Hyun et al. 2000). A major setback of FD is crystallization of the solvent in the pores tends to destroy the network structure in aerogels thus inhibiting cracks. FD also requires prolonged aging than other drying process for stabilization of the network (Daoussi et al. 2009). Despite the shortcomings, FD is used in the current works as one of the methodologies in the binding treatment of the silica aerogel composites fabrication as it is safer and hassle free. This will be discussed in detail in Chap. 3.

## 2.6 Concluding Remarks

Aerogels are fast becoming a niche material, which will be seen as a significant global commodity in the near future. The expected rise in the market value of aerogels could see greater involvement, investment, and collaboration from various industries to achieve commercial success for diversified applications. Silica aerogels are the most researched aerogels that offer the diversity for commercial application. This has been aided by the reduction in production and manufacturing costs. Commercially, available silica aerogels are synthesized under ambient conditions negating the need for expensive equipment. However, main drawbacks of silica aerogels are brittleness and low mechanical properties. Strengthening methodologies of silica aerogels by addition of fibers, resins, and other materials as a composite will be the highlight in the next chapter.

## References

Arndt, E.M., M.D. Gawryla, and D.A. Schiraldi. 2007. Elastic, low density epoxy/clay aerogel composites. *Journal of Materials Chemistry* 17(33): 3525–3529.

Bag, S., P.N. Trikalitis, P.J. Chupas, G.S. Armatas, and M.G. Kanatzidis. 2007. Porous semiconducting gels and aerogels from chalcogenide clusters. *Science* 317(5837): 490–493.

Bhagat, S.D., Y.-H. Kim, Y.-S. Ahn, and J.-G. Yeo. 2007a. Rapid synthesis of water-glass based aerogels by in situ surface modification of the hydrogels. *Applied Surface Science* 253(6): 3231–3236.

Bhagat, S.D., Y.-H. Kim, M.-J. Moon, Y.-S. Ahn, and J.-G. Yeo. 2007b. A cost-effective and fast synthesis of nanoporous SiO2 aerogel powders using water-glass via ambient pressure drying route. *Solid State Sciences* 9(7): 628–635.

Bhagat, S.D., C.-S. Oh, Y.-H. Kim, Y.-S. Ahn, and J.-G. Yeo. 2007c. Methyltrimethoxysilane based monolithic silica aerogels via ambient pressure drying. *Microporous and Mesoporous Materials* 100(1–3): 350–355.

Bhagat, S.D., and A.V. Rao. 2006. Surface chemical modification of TEOS based silica aerogels synthesized by two step (acid-base) sol-gel process. *Applied Surface Science* 252(12): 4289–4297.

Daoussi, R., S. Vessot, J. Andrieu, and O. Monnier. 2009. Sublimation kinetics and sublimation end-point times during freeze-drying of pharmaceutical active principle with organic co-solvent formulations. *Chemical Engineering Research and Design* 87(7): 899–907.

Erik, B., M. Joseph, and P. David. 2006. Thermal resistance and compressive strain of underwater aerogel–syntactic foam hybrid insulation at atmospheric and elevated hydrostatic pressure. *Journal of Physics. D. Applied Physics* 39(9): 1908.

Gerard, P. 2006. *Aerogel synthesis. Catalyst preparation*, 31–43. Boca Raton: CRC Press.

Gesser, H.D., and P.C. Goswami. 1989. Aerogels and related porous materials. *Chemical Reviews* 89(4): 765–788.

Gibiat, V., O. Lefeuvre, T. Woignier, J. Pelous, and J. Phalippou. 1995. Acoustic properties and potential applications of silica aerogels. *Journal of Non-Crystalline Solids* 186: 244–255.

Gurav, J.L., I.-K. Jung, H.-H. Park, E.S. Kang, and D.Y. Nadargi. 2010. Silica aerogel: synthesis and applications. *Journal of Nanomaterials* 2010: 11.

Hong, C.-Q., J.-C. Han, X.-H. Zhang, and J.-C. Du. 2013. Novel nanoporous silica aerogel impregnated highly porous ceramics with low thermal conductivity and enhanced mechanical properties. *Scripta Materialia* 68(8): 599–602.

Hunt, A. J., C. A. Jantzen and W. Cao. 1991. Aerogel. A high performance insulating material at 0.1 bar. In *Insulation materials: Testing and applications*, October 10, 1991–October 12, 1991, Gatlinburg, TN, USA: ASTM.

Hyun, S.H., T.Y. Kim, G.S. Kim, and H.H. Park. 2000. Synthesis of low-k porous silica films via freeze drying. *Journal of Materials Science Letters* 19(20): 1863–1866.

Juzkow, M. 2002. Aerogel capacitors support pulse, hold-up, and main power applications. *Power Electronics Technology* 28(2): 58–60.

Kobayashi, Y., T. Saito, and A. Isogai. 2014. Aerogels with 3D ordered nanofiber skeletons of liquid-crystalline nanocellulose derivatives as tough and transparent insulators. *Angewandte Chemie International Edition* 53(39): 10394–10397.

Koebel, M., A. Rigacci, and P. Achard. 2012. Aerogel-based thermal superinsulation: an overview. *Journal of Sol-Gel Science and Technology* 63(3): 315–339.

Lee, C.J., G.S. Kim, and S.H. Hyun. 2002. Synthesis of silica aerogels from waterglass via new modified ambient drying. *Journal of Materials Science* 37(11): 2237–2241.

Lee, K.-H., S.-Y. Kim, and K.-P. Yoo. 1995. Low-density, hydrophobic aerogels. *Journal of Non-Crystalline Solids* 186: 18–22.

Mahadik, D.B., A.V. Rao, R. Kumar, S.V. Ingale, P.B. Wagh, and S.C. Gupta. 2012. Reduction of processing time by mechanical shaking of the ambient pressure dried TEOS based silica aerogel granules. *Journal of Porous Materials* 19(1): 87–94.

Morris, C.A., M.L. Anderson, R.M. Stroud, C.I. Merzbacher, and D.R. Rolison. 1999. Silica sol as a nanoglue: flexible synthesis of composite aerogels. *Science* 284(5414): 622–624.

Nuckols, M.L., J.C. Chao and M.J. Swiergosz. 2005. Manned evaluation of a prototype composite cold water diving garment using liquids and superinsulation aerogel materials. *Panama*: 28p.

Pajonk, G.M. 1998. Transparent silica aerogels. *Journal of Non-Crystalline Solids* 225: 307–314.

Rao, A.P., G.M. Pajonk, and A.V. Rao. 2005. Effect of preparation conditions on the physical and hydrophobic properties of two step processed ambient pressure dried silica aerogels. *Journal of Materials Science* 40(13): 3481–3489.

Rao, A.V., M.M. Kulkarni, G.M. Pajonk, D.P. Amalnerkar, and T. Seth. 2003. Synthesis and characterization of hydrophobic silica aerogels using trimethylethoxysilane as a co-precursor. *Journal of Sol-Gel Science and Technology* 27(2): 103–109.

Ratke, L., and S. Brück. 2006. Mechanical properties of aerogel composites for casting purposes. *Journal of Materials Science* 41(4): 1019–1024.

Schmidt, M., and F. Schwertfeger. 1998. Applications for silica aerogel products. *Journal of Non-Crystalline Solids* 225: 364–368.

Soleimani Dorcheh, A., and M.H. Abbasi. 2008. Silica aerogel; synthesis, properties and characterization. *Journal of Materials Processing Technology* 199(1–3): 10–26.

Tamon, H., H. Ishizaka, T. Yamamoto, and T. Suzuki. 2001. Freeze drying for preparation of aerogel-like carbon. *Drying Technology* 19(2): 313–324.

Wang, D., F. Zhang, and J. Tang. 2015. Sodium alginate decorated carbon nanotubes-graphene composite aerogel for heavy metal ions detection. *Electrochemistry* 83(2): 84–90.

Wei, G., Y. Liu, X. Zhang, F. Yu, and X. Du. 2011. Thermal conductivities study on silica aerogel and its composite insulation materials. *International Journal of Heat and Mass Transfer* 54(11–12): 2355–2366.

Zu, G.Q., J. Shen, X.Q. Wei, X.Y. Ni, Z.H. Zhang, J.C. Wang, and G.W. Liu. 2011. Preparation and characterization of monolithic alumina aerogels. *Journal of Non-Crystalline Solids* 357(15): 2903–2906.

# Chapter 3
# Fabrication Methods

## 3.1 Introduction

The high porosity and the nanoscaled pores with many dead ends in silica aerogels structure have contributed to their ultra-low density, low thermal conductivity, high optical transmittance, acoustic attenuation, and hydrophobic properties. However, silica aerogels are brittle with very low strength and modulus, which compromise their commercial use. These limitations have warranted the need to broaden and optimize the usefulness for variety of applications. To overcome this drawback, silica aerogels have since been added with another material such as polymers and metals prior to gelation stage of manufacturing before the drying the process.

## 3.2 Silica Aerogel 'Hybrid' Composites—Developments and Limitations

Recent developments into aerogel composites have yielded significant results to enhance the properties of the silica aerogels. Metals, metal oxides, and polymers have been doped during or after formation of wet gel in order to get a composite hybrid (Santos et al. 2006; Xu et al. 2007; Ge et al. 2009; Ye et al. 2010). The use of noble metals such as gold and silver nano particles embedded in silica aerogel by ambient pressure radiolysis using gamma ray irradiation for catalytic applications (Bertino et al. 2004) is another noteworthy development. Innovative method involving in situ growth approach of Au nanoparticles by reducing agent during pre-hydrolysis followed by LTSCD (Ren and Zhang 2010) is one worth mentioning. Cross-linking with epoxies by modifying the surface groups on silica aerogels was reported to improve the modulus by two orders with corresponding 100 % increase in density compared to native silica aerogels (Meador et al. 2005). Meador et al. (2009) further showed that epoxy cross-linked silica aerogels in



M. Sachithanadam and S.C. Joshi, *Silica Aerogel Composites*,
Engineering Materials, DOI 10.1007/978-981-10-0440-7_3

ethanol exhibited strain recovery of up to 50 %. Katti et al. (2006) experimented with polyurethane conformal coating on the silica framework and evaluated the compressive modulus to be 129 MPa, low thermal conductivity of 0.041 $Wm^{-1}$ $K^{-1}$ and exhibiting extended yield behavior till 40 % strain but with an increase in density by 0.40 $g/cm^3$. Cross-linking of metals such as silica–titania aerogels have also been known to improve the strength and are essentially known to possess photocatalytic qualities in the degradation of organic pollutants (Xu et al. 2007). However, the cross-linking route of improving mechanical properties somehow has brought undesirable increase in density and drop in the performance of the thermal insulation. For example, flexible hybrid aerogel composite prepared via layered 5–20 μm glass fibers reinforcement of 9 %wt. produced compressive strength and bending modulus of 21.03 and 12.52 MPa, respectively, with a significant increase in density of 0.227 $g/cm^3$ and thermal conductivity of 0.032 $Wm^{-1}$ $K^{-1}$ (Liao et al. 2012). The diameters of the fibers used are at least three orders greater than the nanopores of the aerogel resulting in elevated strain on the fibers during supercritical drying, resulting in cracks and weaken structural stability as highlighted by Meador et al. (2008) and Wu et al. (2013). Wu et al. recognized that matching of nanopores to electrospun polyvinylidene fluoride (PVDF) nanofibers (20–200 nm) reduces the induced strain between the interfaces and thereby increased the flexibility with strength and stability (Wu et al. 2013).

Table 3.1 shows that the modifications to the silica aerogels are mostly achieved during the sol–gel process where the second constituent material is doped together

**Table 3.1** Selected silica aerogel hybrid composites with enhanced properties

| Composite type | Technique | $\rho$ ($kg/m^3$) | $\lambda$ (W/mK) | S (MPa) | E (MPa) | Ref |
|---|---|---|---|---|---|---|
| Epoxy | Engulfment/post synthesis | 980–1070 | | 83–101 | 1807–1875 | Gupta and Ricci (2008) |
| Di-isocyanate with carbon nanofibre | Sol-Gel SCD with carbon dioxide | 88–469 | | 0.04–5.42 | 0.71–182 | Meador et al. (2008) |
| Epoxy | Hot pressed | 250–720 | 0.044–0.11 | | | Ge et al. (2009) |
| Epoxy | Sol–gel SCD with carbon dioxide | 30–59 | | 0.132 –1.905 | 11.56–126 | Meador et al. (2005) |
| Copper oxide | Sol–gel SCD with carbon dioxide | 71.9–283 | | | | Mohanan and Brock (2003) |
| Ceramic fibers —$SiO_2$ and $Al_2O_3$ | Sol–gel SCD with ethanol | 290 | | | 3.34 @ 800 °C 7.4 @ 25 °C | Yang et al. (2011) |
| Carbon | Sol-Gel SCD with carbon dioxide | 150–240 | | | 23–190 | Moner-Girona et al. (1999) |
| PVDF nano fibers with silica | Electro spun with Sol–gel | 202–277 | 0.027–0.048 | 4.56–5.23 | 0.79–1.10 | Wu et al. (2013) |
| Glass fiber with silica | Sol-Gel with reinforced | 163–227 | 0.024–0.033 | 3.70–21.03 | 5.84–12.21 | Liao et al. (2012) |

with the precursors for gel formation except for two techniques that use epoxy. In fact, a majority of the published literature used sol–gel technique as the path to synthesize mechanically stronger hybrid silica aerogel composites. The only data comparable to this thesis are from Gupta and Ricci (2008) and Ge et al. (2009), who have prepared composites using engulfment and hot pressed methods, respectively, with epoxy. Gupta and Ricci (2008) reported not only high strength and compressive modulus for the composites but also observed that density of the composite is approximately 12 times that of neat silica aerogel granulate. This essentially means that porosity of the silica aerogel is significantly reduced, revealing strong evidence that the epoxy has infiltrated into the pores and displaced the air inside it and ultimately, compromising many of the aerogels' properties. This does not make the composite attractive as there are other polymer-based composites that have higher specific compressive strength and modulus. Ge et al. (2009) investigated thermal conductivity of the epoxy-binder silica aerogel composite. His method involved hot pressing technique where epoxy was ground into powders and aerogel granulates ground into smaller particles. Epoxy liquid with ground aerogel granulates was mixed as dry and wet systems respectively—and subjected to heat treatment and applied pressure to form a composite.

The specimens were lighter compared to those reported by Gupta and Ricci (2008) and exhibited reasonably low thermal conductivity with porosity of approximately 50 %. However, the texture and the mechanical properties of the composite were not reported. The works by these two groups can be considered comparable to the proposed thesis mainly for two reasons: First, they both used the same aerogel granulates from Cabot Corp® (USA) and second, they both used different techniques other than the usual sol–gel technique used in most literature. The aerogel hybrid composites produced via sol–gel technique aim to modify the silica backbone structure during gelation of the precursors. By altering the backbone structure a stronger, stiffer, and a more flexible aerogel can be produced but at the expense of increased density and thermal conductivity which are the most essential properties. While showing tremendous improvements over the past decade, the composites derived from sol–gel technique do have their limitations. First, large amounts of solvent are required during exchanging of fluid prior to the drying stage, which increases the cost of production and renders them commercially expensive. Second, the hazardous substances used during manufacturing of the composites compromise workplace safety and the health of personnel.

## 3.3 Silica Aerogel Binder Composites

### *3.3.1 Associated Problems*

Attempts to bind aerogels similar to traditional composites have yielded little success. Dry binding systems such as epoxy and EVA resins are some of the commonly used binders for composites leveraging on the tackiness of the binding

materials to promote physical adhesion. However, resins being much denser tend to settle at the bottom of the hot plate during the curing stage, thus resulting in nonuniform mixture and distinct separation of the constituent materials. This is a major limitation in using resin binder systems, although Ge et al. (2009) managed to fabricate a composite using epoxy resins primarily because aerogels were ground, technically crushing them into smaller fragments.

Second, the probable infiltration of the second material into the pores of aerogel indefinitely will eliminate the attractive properties of the aerogels as Gupta and Ricci (2008) used acetone for the composite fabrication which resulted in collapsing of the aerogel 'pearl necklace' like structure when mixed with epoxy, reporting a compressive modulus of 1800 MPa due to infiltration of the epoxy mixture through the pores of the aerogels and thus increasing the density, making it heavier than copper. Third, the hydrophobic feature of the silica aerogel provides an additional barrier to the second material to form covalent bonds due to the "terminally inert" TMS groups on the surface. Lastly, although these groups can be decomposed by heat treatment as highlighted by Rao et al. (2003) and revert to the hydroxide (OH) groups, such actions transform the aerogels into powdery form upon contact with water or solvent with water content. The hydrophobic silica aerogel granules structure also deteriorates upon contact with organic solvents such as acetone and toluene, thus eliminating possibilities of binding materials that are soluble in organic solvents. Besides, these solvents are injurious and hazardous to health and their volatility could compromise the safety of the personnel working with these chemicals.

## 3.4 Surface Chemistry of Silica Aerogel Granules

The silica aerogel granules purchased from Cabot Corp® (USA) come in particle sizes of 0.1–4.0 mm, exteriorly coated for hydrophobic properties. They have a mean pore diameter of 20 nm. Their bulk density is approximately 60–80 kg/m$^3$. The industrial name is silica, (TMS)-oxy modified. The oxy-TMS groups on the surface of the aerogel granules provide the hydrophobic properties. Figure 3.1 shows the chemical formulation of the silica aerogel and the physical appearance of silica aerogel granules. Typically, silica aerogel have a melting temperature of above 500 °C but due to the oxy-TMS groups, the operating temperature for this particular silica aerogel is limited to 300–350 °C (Rao et al. 2003; Soleimani Dorcheh and Abbasi 2008) above which, the aerogel will lose its hydrophobic properties as verified with the Safety Data Sheet.

A simple experiment was carried out in-house to affirm this statement in the data sheet, as shown in Fig. 3.2, when the right beaker shows that silica aerogels become whitish and settle down at the bottom after being subjected to heat in a furnace at

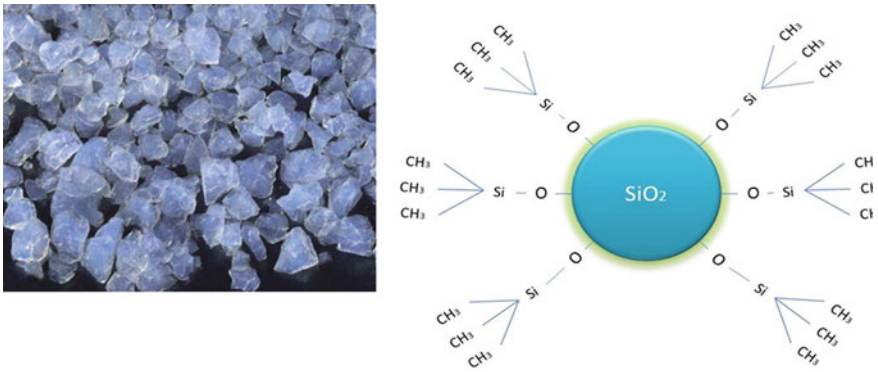


**Fig. 3.1** Silica aerogel granules chemical formulation

**Fig. 3.2** Loss of hydrophobic properties in silica aerogel granules. *Left Beaker* Unheated hydrophobic aerogels are seen floating on the surface of the water. *Right Beaker* Heated aerogels turned whitish indicating shrinkage in volume due to infiltration of water into the pores. As a result, the aerogels become denser and settle down at the bottom of the beaker

350 °C for 2 h. This confirms that the oxy-TMS groups have been decomposed into formaldehyde and reverted to the OH groups since water has penetrated through the pores of the aerogels. The experiment revealed two important aspects for composite fabrication. First, the binder material to be used should bind either with the methyl groups that exist on the surface of the silica aerogels physically or chemically in order to retain the hydrophobic properties. Alternatively, some of the methyl groups must be de-methylated to OH groups in order for water-soluble materials to bind.

## 3.5 Possible Routes of Binder Composite Fabrication

### 3.5.1 Route 1—Resin Binders

Figure 3.3 shows the flowchart of the possible routes of binder composite fabrication. The technique and the problems associated with resin binders have been discussed in Sect. 3.2. Figure 3.4 shows the crushing of the silica aerogel when used with epoxy-acetone solution.

### 3.5.2 Route 2—De-Methylation of Hydrophobic Groups

De-methylation of the TMS groups can be achieved via converting one of the methyl groups to a reactive group or replacing it hydrogen (Jones et al. 2003; Fang et al. 2007) to create some reactive sites through chemically cleaving the attached bonding. Fang et al. (2007) carried out de-methylation of aryl methyl ethers via microwave irradiation method. Such methods are frequently employed in DNA drug deliveries (Jens et al. 2004) and genetic manipulation or biological modifications (Cheng et al. 2004). Shoeb and Kushner (2011) performed de-methylation of $–CH_3$ groups on porous silica substrate in $Ar/O_2$ and $H_2$/He plasma environment to a penetration depth of 10 nm. The plasma de-methylation of methyl groups offers

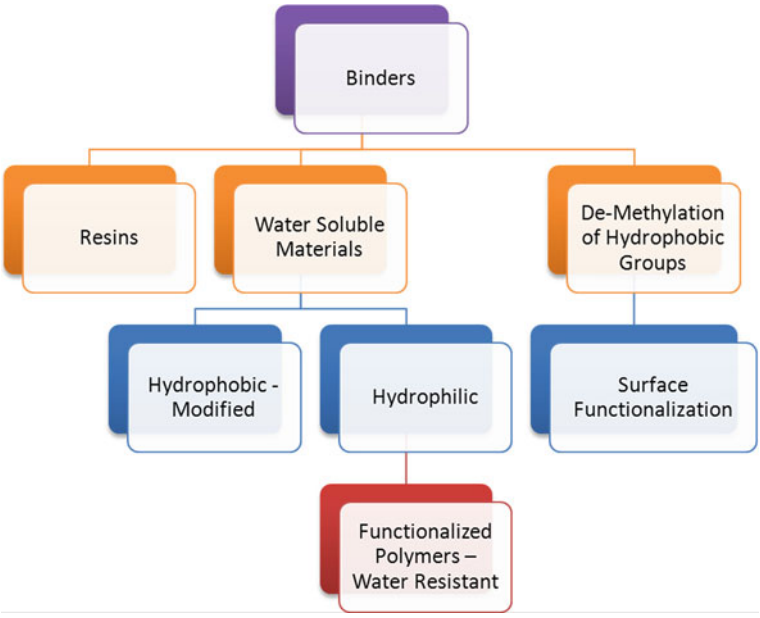


**Fig. 3.3** Postulated binder composite fabrication routes

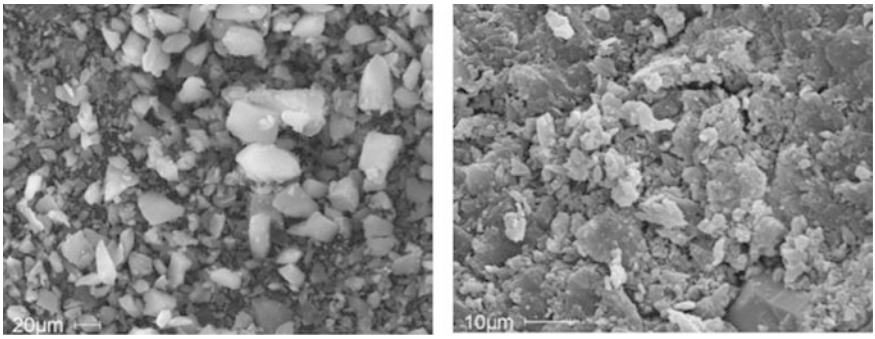


**Fig. 3.4** Crushing of silica aerogel granules when mixed with epoxy-acetone solution (Gupta and Ricci 2008)

the opportunity to bind materials via surface functionalization via CVD as employed by Boday et al. (2008), utilizing methyl cyanoacrylate monomers vaporized in nitrogen to provide the coating. Similar CVD treatment on silica aerogels by Obrey et al. (2011) resulted in improved compressive modulus with high porosity and surface areas with low densities. CVD technique offers good coating on thin films where the scale is in nano to micro meters.

Alternatively, silica aerogel silica aerogel can be heat treated to more than 300 °C as stated in the previous section to convert all the oxy-TMS groups into −OH groups resulting in hydrophilic aerogels. Surface functionalization can then be performed via vapor deposition of suitable polymers in methanol solution heated at above 240 °C for approximately 10 h (Lee et al. 1995).

### *3.5.3 Route 3—Water Soluble Materials*

Water can be evaporated or sublimed from an aqueous solution via heating through controlled pressure and temperature making it a desirable solvent to be used. Furthermore, water does not affect the networked structure of the aerogels. Hence, the hydrophobic properties of the aerogels are not compromised. Water as a solvent is nontoxic and nonhazardous. Water-soluble materials are ideal constituents as a binder. The water-soluble materials must be able to covalently bind with the oxy-TMS groups or at least be physically adsorbed via their charges.

Water-soluble materials are hydrophilic and bonding is achieved through hydrogen bonds and weak van der Waals' interaction between the material and water (Veronica and Adrian 2010). After curing, such bonds can be broken physically through heating. They can also de-bond upon contact with water again. Thus, for these materials to have adequate binding with the aerogels and yet be water resistant, they need to be functionalized or hydrophobically modified.

Polymers are an ideal class of materials due to their wide range of applications and their properties (Schweitzer 2006) can be tailor-made for specific applications via functionalized polymers that have high affinity for water and yet be water resistant once cured (Roy 2008). Classes of functionalized hydrophilic polymers are used in immunoassay techniques due to their ability to undergo fast structural changes for effective separation of reactants (Boris et al. 2001) and pressure sensitive adhesion for membrane engineering (Gary et al. 2008). Polystyrene-OH and Polystyrene-COOH functionalized polymers, although soluble in water, are extremely expensive. Furthermore, developing such materials in the laboratory is a highly skilled expertise. Alternatively, cross-linkers of hydrophilic polymers can be employed to increase overall resistance and reduce mobility of polymer chains and thus improve hydrophobicity. However, cross-linking also introduces increased molecular weight, resulting in an increase in density.

Hydrophobic-modified water-soluble polymers (HMWSP) have gained attraction over the past decade in its application in oil recovery (Candau et al. 1994), as emulsions in paint and membranes distillation (Cheong et al. 2013), and for its ability to adapt and conform to the desired properties. HMWS polymers typically have hydrophobic side chains or are end-capped on a hydrophilic backbone as shown in Fig. 3.5. Karlson et al. (2003) investigated the degradation of network surrounding the hydrophobically end-modified polyethylene glycol (HM-PEG) in an aqueous solution and reported very little absorption of the water but increased entanglement of the polymer chains. Podhajecka et al. (2007) examined the viscoelastic behavior of water-soluble polymers grafted on strong hydrophobic side chain and observed to exhibit sol–gel transition that obeys the percolation theory. This flexibility of HMWSP has therefore introduced yet another possible route to aerogel binder composite.

The three possible routes for silica aerogel binder composites fabrication discussed thus far offer a combination of physical adhesion and covalent bonding

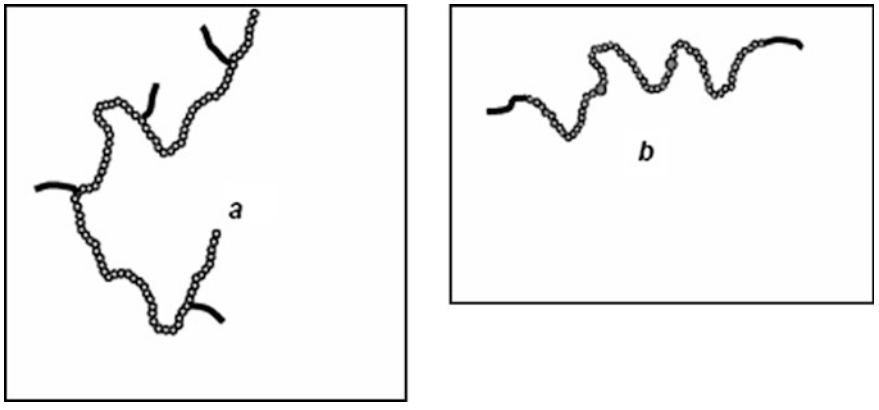


**Fig. 3.5** Schematic illustration of HMWSP **a** side-chain, **b** end-capped. White necklace represents hydrophilic monomers and *bold solid lines* represent hydrophobic groups (Karlson et al. 2003)

through chemical reactions. Herein, Route 3 is the chosen binding route as it offers a wider range of manipulation as well as the flexibility to source for a suitable binder functionalized material that has affinity for water and HMWS polymers.

## 3.6 Possible Binder Materials

This section explores possible binder materials that have the ability to bind with silica aerogels. Functionalized water soluble polymers or polymers that have the ability to be functionalized and HMWSP are the materials considered in this section.

### *3.6.1 Gelatin*

"Gelatin" is derived from "gelatus," the Latin word for "stiff" or "frozen". As its name implies, gelatin has the ability to solidify into jelly. The gelling property is one of gelatin's most important characteristics. Gelatin is a heterogeneous mixture of water-soluble proteins of high average molecular masses, present in collagen extracted by boiling skins, tendons, ligaments, bones, etc., in water. Collagen that is denatured with heat and becomes soluble in water is referred to as Gelatin (Yannas and Tobolsky 1968; Kozlov and Burdygina 1983; Thomas 1998; Aristippos 2002; Ioannis 2002; Smitha et al. 2007). Gelatin, as a biocompatible polymer, has been used as a delivery vehicle for the release of bioactive molecules and in the generation of scaffolds for tissue engineering applications (Liu and Ma 2009; Frydrych et al. 2011). Industrial applications include the use of gelatin as a stabilizer, thickener, and texturizer in foods and in the manufacture of rubber substitutes, adhesives, cements, lithographic and printing inks, plastic compounds, artificial silk, photographic plates, and films (Ioannis 2002). In the pharmaceutical industry, gelatin is used as a suspending agent, encapsulating agent, and tablet binder; and in veterinary applications, it is used as a plasma expander and hemostatic sponge (Aristippos 2002).

Within the living body, the collagen molecule has a regularly-structured triple helix structure and is insoluble in water (Ioannis 2002). On the other hand, when collagen is heated for extended periods of time, the triple helix molecular structure unfolds at a certain temperature, and the collagen dissolves into random peptide chains in solution forming gelatin. Gelatin chains can be intertwined back into the collagen helix through an appropriate technique, such as cooling or annealing in solution (Kozlov and Burdygina 1983; Ioannis 2002). Type A gelatin is derived from acid-cured tissue while Type B gelatin is derived from lime-cured tissue (Ioannis 2002). The transformation of gelatin as loose polymer chained when heated into an almost helically entangled chain when cooled is an important characteristic and shows its ability to pull the adjacent chains to form a network.

Gelatin has both polar and nonpolar side chains. It is being explored as a biodegradable polymer and one of the key advantages over other polymers is that gelatin is nontoxic and not hazardous. It is also versatile enough to synthesis as polymer blends and is soluble in water. This is very desirable as a binder for aerogels as it is lipophilic. The high number of amino acids in one compound is also desirable because it offers more than one reactive sites. Fidler and Thomas (1996, 2000) patented an aerogel insulated foam using gelatin as the main binding material and additives from inorganic and organic materials to investigate the thermal conductivity of the aerogel composite. Their work involved blending the aerogels and gelatin into a foam and curing it under ambient conditions. A typical chemical structure should resemble that shown in Fig. 3.6.

The works of Fidler and Thomas revealed the versatility of gelatin as a polymer that can fulfill the binding concept of Route 3. Gelatin due to its numerous amine and carboxyl sites, offers cross-linking, functionalization, and even grafting of hydrophobic materials onto its peptide chain (Fidler 1996, 2000). The primary structure (amino acid sequence) of gelatin consists of 18 different amino acids and is almost identical to the parent collagen except for some small differences due to pretreatment and extraction processes. Figure 3.7 shows the composition of gelatin (Ioannis 2002). The precise macromolecular constitution of gelatin resulting from a

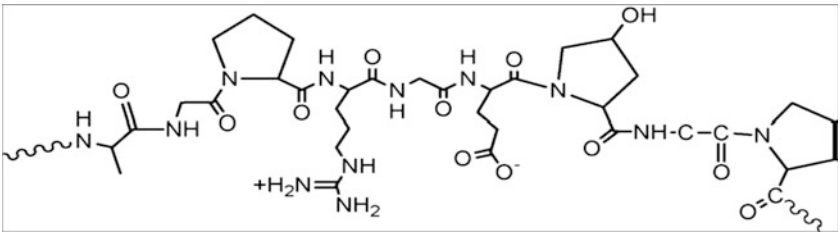


**Fig. 3.6** Basic unit of gelatin molecule (Smitha et al. 2007)

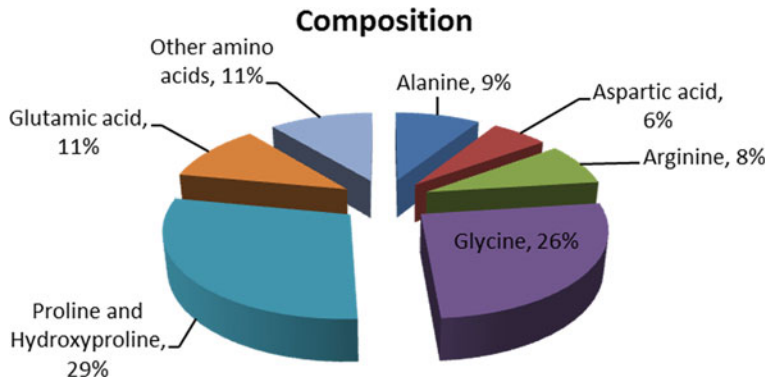


**Fig. 3.7** Composition of gelatin

melting process depends on the collagen source and the extraction method (Yannas and Tobolsky 1968; Ioannis 2002) and thus the exact chemical structure of the gelatin can vary due to this reason.

#### 3.6.1.1 Properties of Gelatin

Gelatin in the solid state behaves as a brittle material in the absence of water, similar to a rigid polymer chains (Kozlov and Burdygina 1983). When absorbed by water, they transform from glassy to rubbery material. Gelatin exhibits viscoelastic behavior when subjected to heat at the upper limit of 210 °C (Kozlov and Burdygina 1983). The $T_m$ and $T_g$ of gelatin is approximately 220 and 200 °C respectively (Ioannis 2002). Generally, $T_m$ and $T_g$ decrease with increase in moisture content as shown in Fig. 3.8. Gelatin is mainly characterized by bloom strength number and viscosity. An apparatus called the Bloom gelometer measures the strength of a gel formed from a solution of known concentration and it is proportional to its average molecular mass. Bloom number in the range from 225 to 325 typically indicates high strength gelatin with an average molecular mass in the range from 50,000 to 100,000.

Yakimets et al. (2005) correlated that gelatin shows improved mechanical properties with 7 to 14 % of water content. They argued that the water is regarded as "structural water" where it is directly bound to the protein (both inside and

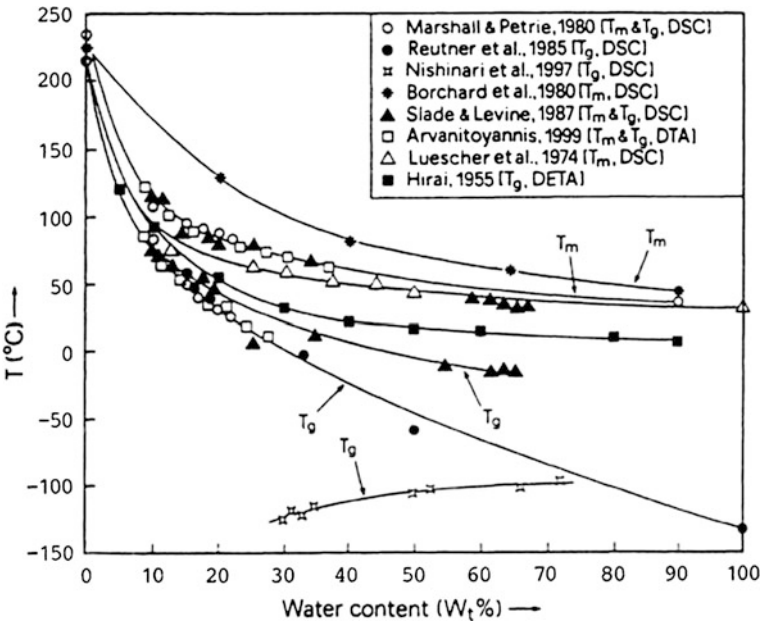


**Fig. 3.8** State diagram of gelatin–water system (Ioannis 2002)

outside helical fragments). They also reported that at the $T_g$ of gelatin was observed to be at the peak in within the range stated above (Yakimets et al. 2005).

## 3.6.2 Additives

### 3.6.2.1 Sodium Dodecyl Sulfate (SDS)

SDS is an anionic surfactant used in many cleaning and hygiene products. The salt is of an organo-sulfate consisting of a 12-carbon tail attached to a sulfate group, giving the material the amphiphilic properties required of a detergent. Being derived from inexpensive coconut and palm oils, it is a common component of many domestic cleaning products. Figure 3.9 shows the chemical structure of SDS. SDS is further used in lysing cells during DNA extraction and also as shark repellent (Ruiz et al. 2008). As a detergent, SDS has the ability to foam and form micelles and is known to denature proteins (Mo and Sun 2000). Denaturation can modify the secondary, tertiary ,or quaternary structures of protein molecules without breaking the peptide bonds.

### 3.6.2.2 Carbon Nanotubes (CNTs)

CNTs have remarkable mechanical properties, high thermal and chemical stability and excellent heat conduction with hardness of diamond and conductivity of graphite (Jing 2004). Their applications are widespread and keen interest has been revolutionized in the specialization of sensors (Jing 2004). CNTs have high aspect ratio with a diameter of a few nanometers and length of micrometers and can be manufactured into extremely thin wires (Jie 2004; Jing 2004). Multi-walled CNTs (MWNTs) were first discovered by Iijima in 1991 and Single-walled CNTs (SWNTs) two years later (Jie 2004; Jing 2004; Rivière 2012). The structure of MWNT can be seen as a group of coaxial SWNTs forming a hollow cylinder of graphite sheets (Jie 2004; Rivière 2012). More essentially, MWNTs can be structured into different conformations as shown in Fig. 3.10 for specific applications or design (Jie 2004; Rivière 2012). The Young's Modulus and tensile strength of MWNT is reported to be as high as 1200 and 150 GPa, respectively (Jie 2004).

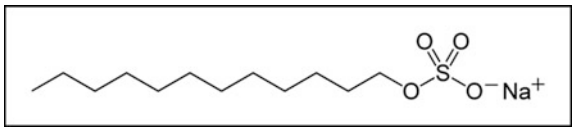


**Fig. 3.9** Chemical structure of SDS

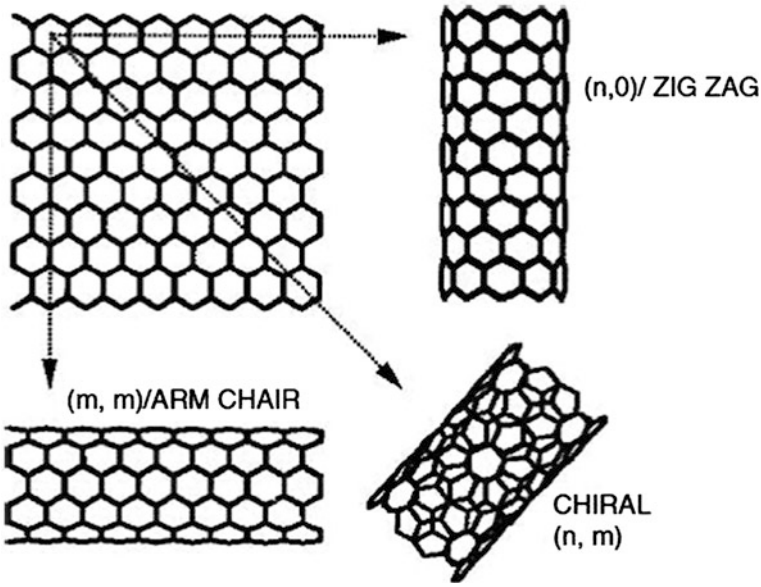


**Fig. 3.10** MWNT in various conformations (Jie 2004)

#### 3.6.2.3 Functionalized CNTs

SWNTs and MWNTs have strong π–π interactions between them resulting in the formation of aggregates, thus preventing homogeneous dispersion when blended into a matrix material to form a composite (Chattopadhyay and Webster 2009) resulting in underperformance of the composite and underpin the final properties. Modification to the structure of the CNT was therefore necessary and achieved via chemical surface functionalization, a technique that allows functional groups to be attached to the CNT to provide better covalent bonding, adhesion and improvement in the dispersion of the CNT in the matrix material (Gojny et al. 2003; Tagmatarchis and Prato 2005). Gojny functionalized MWNTs by refluxing the tubes with multifunctional amines embedded in epoxy resin (Gojny et al. 2003). Tagmatarchis et al. functionalized using 1,3-dipolar cycloaddition of azomethineylides (Tagmatarchis and Prato 2005). CNT are very good thermal conductors and their conductivity has been measured as high as 3500 W/m-K (Pop et al. 2005; Balakrishnan and Saha 2011). Kim et al. measured the thermal conductivity of a single MWNT using microfabricated suspended device and observed the thermal conductivity to be more than 3000 W/m-K (Kim et al. 2001). Sinha et al. (2005) investigated the room-temperature thermal conductivity for SWNT and MWNT in the radial direction and found it to be about 1.6 and 1.52 W/m-K, respectively, which is as thermally conductive as soil.

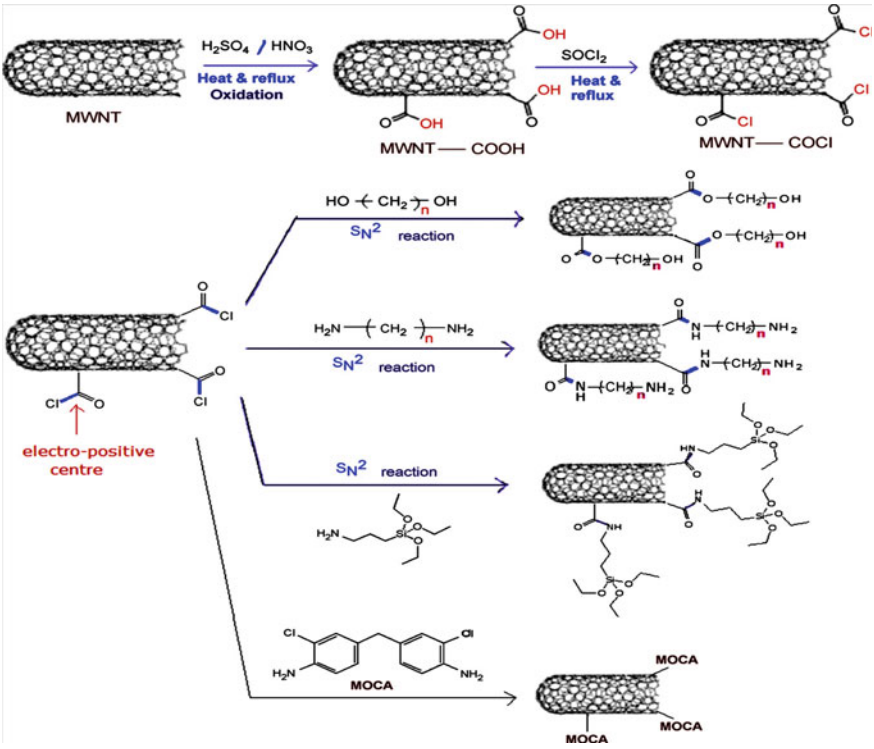


**Fig. 3.11** Derivatives of functionalized MWNT (Chattopadhyay and Webster 2009)

Currently, wide varieties of functionalized CNTs are available commercially for practical applications such as reinforcement in composites, nanoelectrodes, drug delivery, and supercapacitors to name a few. Figure 3.11 shows some of the techniques used in functionalized MWNTs production (Chattopadhyay and Webster 2009).

## 3.7 Materials' Property and Data

Silica aerogel granules were purchased from Cabot Corp®(USA). High strength gelatin from porcine skin (Bloom Strength 240–270) used as binder for the silica aerogel and sodium dodecyl sulfate (SDS) (#436143) were purchased from Sigma Aldrich. Functional MWNT–COOHs were purchased from Nanostructured and Amorphous Materials, Inc. Table 3.2 highlights some of the key properties of the individual materials used in this study.

**Table 3.2** General properties of materials under study

| Properties | Silica aerogel | Gelatin | SDS | MWNT-COOH |
|---|---|---|---|---|
| Appearance | Translucent granulates | Yellowish brown granulates | White power | Black powders |
| Density | 0.08–0.10 g/cm$^3$ | [a]0.8925–1.1940 g/cm$^3$ | 0.37 g/cm$^3$ | 2.1 g/cm$^3$ @ 20 °C |
| Solubility | Insoluble | Soluble | Soluble | Insoluble |
| Melting point | 1700 °C | Not available | 204–207 °C | 3652–3697 °C |
| Boiling point | 2230 °C | Not available | Not available | Not available |
| Strength | 16 kPa | Bloom strength (240–270) [a]33.48–62.43 MPa | Not available | Not available |
| Young's modulus | 0.1–10 MPa | 1497 MPa (Frydrych et al. 2011) [a]2138–2560 MPa | Not available | Not available |
| Remarks | >90 % porous. Fully hydrophobic. Heating above 300 °C decomposes the hydrophobic coating by release of formaldehyde | | | Content of—COOH: 1.22–1.34 % Outside diameter: 8–15 nm Inside diameter: 3–5 nm Length: ~50 μm |

[a]Data from in-house experiments on gelatin films for density, modulus, strength and thermal conductivity

## 3.8 Fabrication Methodologies of GSA Composites

### *3.8.1 FM Method*

The flowchart in Fig. 3.12 shows the processes in fabricating the composites via 'Froth and Mix' (FM) method. The basic constituent materials are water, gelatin, and silica aerogels. SDS and/or FMWNT were added as the additives to the basic composite. The variants in the composites' makeup are evaluated separately and comparatively based on various properties. Compared with the works of Fidler and Thomas (1996, 2000), there are two key fabrication processes that are entirely different. For the first, the aqueous solution of gelatin was obtained via sonication using Fisher Scientific FB15051 in Stage 1. Sonication allows particles to dissolve through vibration signals generated by the equipment shown in Fig. 3.13. Since the amount of water used in dissolving the gelatin is small (12 ml in a tightly lid bottle),

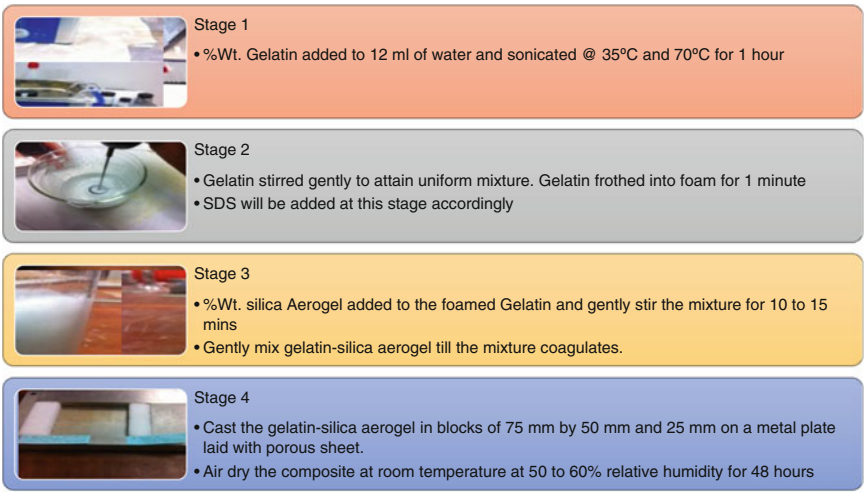


**Fig. 3.12** Fabrication of composite via 'Froth and Mix' (*FM*) method with or without SDS

| Fisher Scientific FB 15051 Specifications | |
|---|---|
| **Tank Volume (liters)** | 2.75 |
| **Weight (kg)** | 3.3 |
| **Tank dimensions (mm)** | 240 x 137 x 100 |
| **Ultrasonic Frequency (kHz)** | 37 |
| **Power (Watts)** | 80/280 |

**Fig. 3.13** Sonication bath to dissolve the WSP prior to frothing of aqueous solution

the volume remains constant and will not be lost due to evaporation or heat like in conventional dissolving techniques. Sonication also allows higher amounts of gelatin to be dissolved compared to stirring method such as using hot water. When using hot water, the loss of water through heat as vapor to the surrounding is hastened leaving some portion of gelatin undissolved. Thus, additional amount of hot water is needed to fully dissolve the remaining gelatin granules.

The second difference is that frothing of the aqueous gelatin solution is carried out prior to the addition of aerogel particles. Frothing induces a large amount of air into the solution, thus increasing the overall volume of the aqueous solution and therefore reducing the density. The reduced density of the aqueous solution eventually leads to minimal effect on the overall density of the composite compared to the neat aerogels.

Gelatin solutions from 2.0 to 50.0 %wt. in 12 ml water are prepared at 35 and 70 °C via sonication for 1 h to dissolve the gelatin granules. The solution is then stirred gently to achieve a homogeneous mix. Quantities of SDS from 0.0 to 0.66 % wt. are then dispersed into the solution and frothed into foam before adding 50.0–98.0 %wt. of silica aerogel granules. The frothed gelatin/SDS foam is then mixed carefully with silica aerogel with a stirrer with a relatively slow motion for 10 min to avoid breaking the silica aerogel until the mixture binds. The mixture is then cast as blocks of 75 mm × 50 mm × 25 mm on a metal dish laid with a porous sheet. The composites are left to cure at room temperature with a relative humidity of 60 %. Other additives such as functionalized MWNTs (FMWNTs) are added in stage 1 during sonication process.

### *3.8.2 FD Method*

Another fabrication methodology is via the freeze drying (FD) method. The aqueous solution of gelatin is obtained via sonication as described in the previous section. However, the solution in this case is not foamed by frothing as described in Fig. 3.12. Instead, the silica aerogel granules are mixed in the solution for about 10 min till a tacky mix is obtained. Thereafter, the mixture is casted onto a 100 mm diameter petri dish or in a metal mold of 75 mm × 50 mm by 25 mm laid with a porous sheet. The composite mold is covered with transparent porous foil and

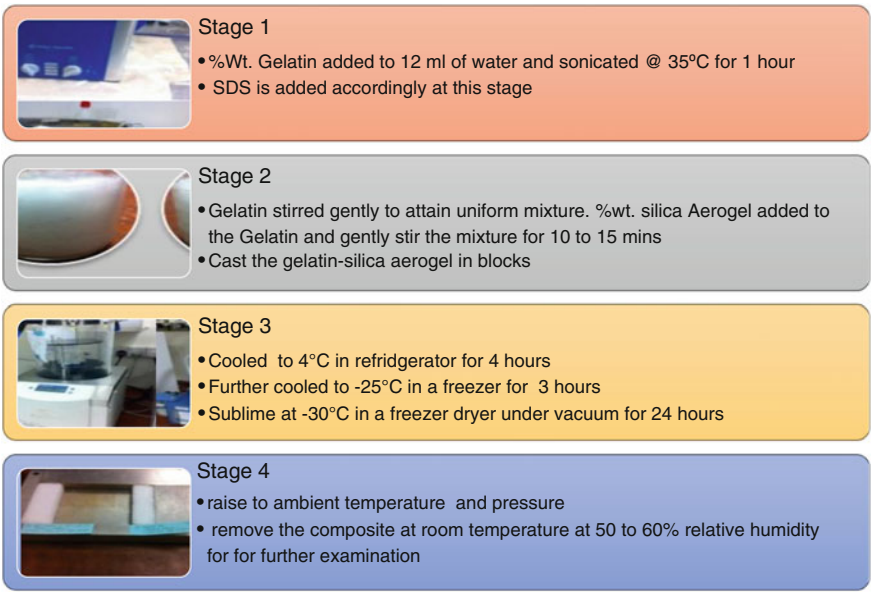


**Fig. 3.14** Fabrication of composite via FD method with or without SDS

secured with tape to allow for sublimation of water to take place when placed under vacuum. The composite is then cooled to 4 °C in a refrigerator for 4 h. This will allow the gelatin solution to lyophilize. The composite is further cooled to −25 °C in a freezer for another 3 h. The fully frozen sample is sublimated at −30 °C under vacuum for 24 h when transferred onto the freeze dryer. Full sublimation is achieved when the chamber temperature drops to −45 °C. Thereafter, the temperature is raised to an ambient temperature at 2 °C $min^{-1}$. The pressure is increased by slight opening of the vent valve on the chamber for 4 h. The fabrication process is shown in Fig. 3.14.

If the pressure is higher than 6.11 mbar, water undergoes all three phases (solid, liquid, gas) when the temperature is lowered or raised. At 6.11 mbar and 273.13 K, the melting pressure curve, vapor pressure curve and sublimation pressure curve meet at a point called the triple point. At this point, all three phases occur simultaneously. Below this point, i.e., when the pressure is lower than 6.11 mbar, the ice is converted directly from a solid into a gaseous phase upon reaching the sublimation pressure curve. The simultaneous action of vacuum and temperature has two effects on the composites. First, the vacuum facilitates a tight packing order of the silica aerogel granules, thus minimizing void and pores generated as a result of mixing of the gelatin. Second, the double action of temperature and vacuum sublimes the water content in the gelatine solution, thus leaving only the gelatin to be networked around the silica aerogel granules. Thus, binding is achieved physically as well. The significance of this will allow water soluble polymer to be physically bounded without the need to form covalent bonds. On the other hand, the disadvantage would be an overall reduction on the porosity of aerogels since the particles are also subjected to vacuum pressure.

## 3.9 Concluding Remarks

This chapter highlights the selection of fabrication methods for making silica aerogel composites. Merits and demerits of two different fabrication methodologies, one via FM method and the other on the principle of sublimation through FD method, have been examined. The recent developments and the limitations on the properties of hybrid silica aerogel composites, namely increased density with increasing thermal conductivities compromise two of the significant features of the aerogels. The properties of silica aerogel granules that are used as primary material and the possible binding routes were presented. The surface chemistry of the silica aerogels poses a challenge for effective binding of additive materials. Binding via Route 3 (functionalized polymers and HMWSP) seems to show a greater potential amongst those proposed. These materials and route provide flexibility of tailoring the final properties. Gelatin is chosen as the core primary binding material for its versatility and its ability to be cross-linked, functionalized, and grafted onto suitable polymer systems. SDS and FMWNTs are added to tailor the specific property of the GSA composite.

# References


Aristippos, G. 2002. *Soft gelatin capsules. Protein-based films and coatings*. Boca Raton: CRC Press.

Balakrishnan, A., and M.C. Saha. 2011. Tensile fracture and thermal conductivity characterization of toughened epoxy/CNT nanocomposites. *Materials Science and Engineering A* 528(3): 906–913.

Bertino, M.F., J.F. Hund, G. Zhang, C. Sotiriou-Leventis, A.T. Tokuhiro, and N. Leventis. 2004. Room temperature synthesis of noble metal clusters in the mesopores of mechanically strong silica-polymer aerogel composites. *Journal of Sol-Gel Science and Technology* 30(1): 43–48.

Boday, D.J., K.A. DeFriend, K.V. Wilson, D. Coder, and D.A. Loy. 2008. Formation of polycyanoacrylate—silica nanocomposites by chemical vapor deposition of cyanoacrylates on aerogels. *Chemistry of Materials* 20(9): 2845–2847.

Boris, D., Z. Anatoliy, and Y. Elena. 2001. *Application of water soluble polymers and their complexes for immunoanalytical purposes. Smart polymers*. Boca Raton: CRC Press.

Candau, F., S. Biggs, A. Hill, and J. Selb. 1994. Synthesis, structure and properties of hydrophobically associating polymers. *Progress in Organic Coatings* 24(1–4): 11–19.

Chattopadhyay, D.K., and D.C. Webster. 2009. Thermal stability and flame retardancy of polyurethanes. *Progress in Polymer Science* 34(10): 1068–1133.

Cheng, W., J. Peter Daniel, and C. Jonathan. 2004. *DNA Demethylating agents. DNA methylation*, 151–167. Boca Raton: CRC Press.

Cheong, S., B. Kim, H. Lee, and J. Rhim. 2013. Physical adsorption of water-soluble polymers on hydrophobic polymeric membrane surfaces via salting-out effect. *Macromolecular Research* 21(6): 629–635.

Fang, Z., G.-C. Zhou, S.-L. Zheng, G.-L. He, J.-L. Li, L. He, and D. Bei. 2007. Lithium chloride-catalyzed selective demethylation of aryl methyl ethers under microwave irradiation. *Journal of Molecular Catalysis A: Chemical* 274(1–2): 16–23.

Fidler, C. (W. S., PA), and C.S. Thomas (Willow Street, PA). 1996. Aerogel-in-foam thermal insulation and its preparation. United States: Armstrong World Industries, Inc. (Lancaster, PA).

Fidler, C. (W. S., PA), and C.S. Thomas (Willow Street, PA) (2000). Aerogel-in-foam thermal insulation and its preparation. United States, Armacell LLC (DE).

Frydrych, M., C. Wan, R. Stengler, K.U. O'Kelly, and B. Chen. 2011. Structure and mechanical properties of gelatin/sepiolite nanocomposite foams. *Journal of Materials Chemistry* 21(25): 9103–9111.

Gary, C., F. Mikhail, and S. Parminder. 2008. *Hydrophilic adhesives. Technology of pressure-sensitive adhesives and products*. Boca Raton: CRC Press, 7-1-7-80.

Ge, D.T., L.L. Yang, Y. Li, and J.P. Zhao. 2009. Hydrophobic and thermal insulation properties of silica aerogel/epoxy composite. *Journal of Non-Crystalline Solids* 355(52–54): 2610–2615.

Gojny, F.H., J. Nastalczyk, Z. Roslaniec, and K. Schulte. 2003. Surface modified multi-walled carbon nanotubes in CNT/epoxy-composites. *Chemical Physics Letters* 370(5–6): 820–824.

Gupta, N., and W. Ricci. 2008. Processing and compressive properties of aerogel/epoxy composites. *Journal of Materials Processing Technology* 198(1–3): 178–182.

Ioannis, A. 2002. *Formation and properties of and gelatin films and coatings. Protein-based films and coatings*. Boca Raton: CRC Press.

Jens, H., C. Rainer, and L. Michael. 2004. *DNA Demethylating agents. DNA Methylation*, 183–212. Boca Raton: CRC Press.

Jie, H. 2004. *Structures and properties of carbon nanotubes. Carbon nanotubes*, 1–24. Boca raton: CRC Press.

Jing, L. 2004. *Carbon nanotube applications. Carbon nanotubes*, 213–235. Boca Raton: CRC Press.

Jones, K., X. Roset, S. Rossiter, and P. Whitfield. 2003. Demethylation of 2,4-dimethoxyquinolines: The synthesis of atanine. *Organic and Biomolecular Chemistry* 1 (24): 4380–4383.

Karlson, L., C. Malmborg, K. Thuresson, and O. Söderman. 2003. Complex formed in the system hydrophobically modified polyethylene glycol/methylated α-cyclodextrin/water. An NMR diffusometry study. *Colloids and Surfaces A: Physicochemical and Engineering Aspects* 228 (1–3): 171–179.

Katti, A., N. Shimpi, S. Roy, H. Lu, E.F. Fabrizio, A. Dass, L.A. Capadona, and N. Leventis. 2006. Chemical, physical, and mechanical characterization of isocyanate cross-Linked amine-modified silica aerogels. *Chemistry of Materials* 18(2): 285–296.

Kim, P., L. Shi, A. Majumdar, and P.L. McEuen. 2001. Thermal transport measurements of individual multiwalled nanotubes. *Physical Review Letters* 87(21): 215502.

Kozlov, P.V., and G.I. Burdygina. 1983. The structure and properties of solid gelatin and the principles of their modification. *Polymer* 24(6): 651–666.

Lee, K.-H., S.-Y. Kim, and K.-P. Yoo. 1995. Low-density, hydrophobic aerogels. *Journal of Non-Crystalline Solids* 186: 18–22.

Liao, Y., H. Wu, Y. Ding, S. Yin, M. Wang, and A. Cao. 2012. Engineering thermal and mechanical properties of flexible fiber-reinforced aerogel composites. *Journal of Sol-Gel Science and Technology* 63(3): 445–456.

Liu, X., and P.X. Ma. 2009. Phase separation, pore structure, and properties of nanofibrous gelatin scaffolds. *Biomaterials* 30(25): 4094–4103.

Meador, M.A.B., E.F. Fabrizio, F. Ilhan, A. Dass, G. Zhang, P. Vassilaras, J.C. Johnston, and N. Leventis. 2005. Cross-linking amine-modified silica aerogels with epoxies: Mechanically strong lightweight porous materials. *Chemistry of Materials* 17(5): 1085–1098.

Meador, M.A.B., S.L. Vivod, L. McCorkle, D. Quade, R.M. Sullivan, L.J. Ghosn, N. Clark, and L. A. Capadona. 2008. Reinforcing polymer cross-linked aerogels with carbon nanofibers. *Journal of Materials Chemistry* 18(16): 1843–1852.

Meador, M.A.B., A.S. Weber, A. Hindi, M. Naumenko, L. McCorkle, D. Quade, S.L. Vivod, G.L. Gould, S. White, and K. Deshpande. 2009. Structure—property relationships in porous 3D nanostructures: Epoxy-cross-linked silica aerogels produced using ethanol as the solvent. *ACS Applied Materials & Interfaces* 1(4): 894–906.

Mo, X., and X. Sun. 2000. Thermal and mechanical properties of plastics molded from sodium dodecyl sulfate-modified soy protein isolates. *Journal of Polymers and the Environment* 8(4): 161–166.

Mohanan, J.L., and S.L. Brock. 2003. Influence of synthetic and processing on the surface area, speciation, and particle formation in copper oxide/silica aerogel composites. *Chemistry of Materials* 15(13): 2567–2576.

Moner-Girona, M., A. Roig, E. Molins, E. Martinez, and J. Esteve. 1999. Micromechanical properties of silica aerogels. *Applied Physics Letters* 75(5): 653–655.

Obrey, K.A.D., K.V. Wilson, and D.A. Loy. 2011. Enhancing mechanical properties of silica aerogels. *Journal of Non-Crystalline Solids* 357(19–20): 3435–3441.

Podhajecka, K., K. Prochazka, and D. Hourdet. 2007. Synthesis and viscoelastic behavior of water-soluble polymers modified with strong hydrophobic side chains. *Polymer* 48(6): 1586–1595.

Pop, E., D. Mann, Q. Wang, K. Goodson, and H. Dai. 2005. Thermal conductance of an individual single-wall carbon nanotube above room temperature. *Nano Letters* 6(1): 96–100.

Rao, A.V., M.M. Kulkarni, G.M. Pajonk, D.P. Amalnerkar, and T. Seth. 2003. Synthesis and characterization of hydrophobic silica aerogels using trimethylethoxysilane as a Co-precursor. *Journal of Sol-Gel Science and Technology* 27(2): 103–109.

Ren, H., and L. Zhang. 2010. In situ growth approach for preparation of Au nanoparticle-doped silica aerogel. *Colloids and Surfaces A: Physicochemical and Engineering Aspects* 372(1–3): 98–101.

Rivière, SMaJC. 2012. *Carbon nanotubes and other tube structures. Characterization of nanostructures*, 215–252. Boca Raton: CRC Press.

Roy, M. C. S. K. 2008. Industrial polymers. Industrial polymers, specialty polymers, and their applications. Boca Raton: CRC Press, 1-1-1-161.

Ruiz, C.C., L. Díaz-López, and J. Aguiar. 2008. Micellization of sodium dodecyl sulfate in glycerol aqueous mixtures. *Journal of Dispersion Science and Technology* 29(2): 266–273.

Santos, A., J.A. Toledo-Fernández, R. Mendoza-Serna, L. Gago-Duport, N. de la Rosa-Fox, M. Piñero, and L. Esquivias. 2006. Chemically active silica aerogel—wollastonite composites for $CO_2$ fixation by carbonation reactions. *Industrial and Engineering Chemistry Research* 46(1): 103–107.

Schweitzer, P.A. 2006. *Thermoset polymers. Corrosion of polymers and elastomers*, 147–220. Boca Raton: CRC Press.

Shoeb, J., and M.J. Kushner. 2011. Minimizing damage of porous SiCOH using $He/H_2$ plasmas. In *2011 Abstracts IEEE International Conference on Plasma Science (ICOPS)*.

Sinha, S., S. Barjami, G. Iannacchione, A. Schwab, and G. Muench. 2005. Off-axis thermal properties of carbon nanotube films. *Journal of Nanoparticle Research* 7(6): 651–657.

Smitha, S., P. Mukundan, P. Krishna Pillai, and K.G.K. Warrier. 2007. Silica-gelatin bio-hybrid and transparent nano-coatings through sol-gel technique. *Materials Chemistry and Physics* 103 (2–3): 318–322.

Soleimani Dorcheh, A., and M.H. Abbasi. 2008. Silica aerogel; synthesis properties and characterization. *Journal of Materials Processing Technology* 199(1–3): 10–26.

Tagmatarchis, N., and M. Prato. 2005. Carbon-based materials: From fullerene nanostructures to functionalized carbon nanotubes. *Pure and Applied Chemistry* 77(10): 1675–1684.

Thomas, K. 1998. *Gelatin. Handbook of biodegradable polymers*. Boca Raton: CRC Press.

Veronica, V., and T. Adrian. 2010. *Water. Water and life*, 235–247. Boca Raton: CRC Press.

Wu, H., Y. Chen, Q. Chen, Y. Ding, X. Zhou, and H. Gao. 2013. Synthesis of flexible aerogel composites reinforced with electrospun nanofibers and microparticles for thermal insulation. *Journal of Nanomaterials* 2013: 8.

Xu, Z., L. Gan, Y. Jia, Z. Hao, M. Liu, and L. Chen. 2007. Preparation and characterization of silica-titania aerogel-like balls by ambient pressure drying. *Journal of Sol-Gel Science and Technology* 41(3): 203–207.

Yakimets, I., N. Wellner, A.C. Smith, R.H. Wilson, I. Farhat, and J. Mitchell. 2005. Mechanical properties with respect to water content in glassy state. *Polymer* 46(26): 12577–12585.

Yang, X., Y. Sun, D. Shi, and J. Liu. 2011. Experimental investigation on mechanical properties of a fiber-reinforced silica aerogel composite. *Materials Science and Engineering A* 528(13–14): 4830–4836.

Yannas, I.V., and A.V. Tobolsky. 1968. High-temperature transformations of gelatin. *European Polymer Journal* 4(2): 257–264.

Ye, L., Z.-H. Ji, W.-J. Han, J.-D. Hu, and T. Zhao. 2010. Synthesis and characterization of silica/carbon composite aerogels. *Journal of the American Ceramic Society* 93(4): 1156–1163.

# Chapter 4
# Microstructural Analysis

## 4.1 Introduction

Gelatin is the main binder in the fabrication of composites and it is therefore essential to evaluate its properties. Gelatin films (GF) are fabricated as films and investigated for density, strength, modulus, thermal conductivity, and for chemical states variations in binding energy through XPS. The hypothesis on the binder concept allows us to postulate the various types of materials that may work and may not work. It is an important thought process to identify and test the hypothesis against a set of experiments. This chapter mainly focus on microstructural behavior, especially what causes the gelatin to bind with the hydrophobic silica aerogel granules.

## 4.2 Hypothesis on Binder Concept

Fidler and Thomas (Fidler and Simonton 1996, 2000) had described using aqueous solution of gelatin by binding them with silica aerogels to make a composite. Thus, the initial postulation is to use gelatin-like substances such as albumin from egg white and carrageenan. Both these substances have the ability to become a gel when dissolved in water. However, they failed to bind with aerogels when evaluated in the laboratory even though these substances showed similar texture to gelatin. Second, when the heated silica aerogels (@ 350 °C as described in the Chap. 3) were mixed with gelatin solution, it is observed that the gelatin solution did not bind these aerogel granules as seen in Fig. 4.1. Therefore, it is evident that there exist some interactions between the oxy-TMS groups on the silica aerogel granules with the gelatin solution. Three possible outcomes can be derived from the above statement. It is possible that the interaction could be due to: (i) covalent bonding of the TMSoxy groups onto the various carboxyl and amine groups of the gelatin;



M. Sachithanadam and S.C. Joshi, *Silica Aerogel Composites*,
Engineering Materials, DOI 10.1007/978-981-10-0440-7_4

**Fig. 4.1** Non-binding of heat-treated aerogels with gelatin. *Aqueous gelatin solution failed to bind with heat-treated silica aerogel granules but was instead absorbed by the aerogels is an indication of loss of hydrophobic properties*

(ii) weak van der Waals interaction or (iii) dipole–dipole interactions of charged particles of silica aerogel granules and gelatin. The preliminary investigations reported in this chapter aim to resolve the above hypothesis through microstructural examinations and simple experiments.

## 4.3 Chemical Analysis of Gelatin Films

The mechanical and physical properties of gelatin vary from each manufacturer due to its complex structure and the different sources it comes from. Thus, it is important to evaluate these properties of the gelatin used in the experiments for analysis of the composite properties.

The fabrication of gelatin films (GF) is shown in Fig. 4.2. GF in concentrations from 5 to 50 wt% are fabricated as seen in Fig. 4.3. The mass of the dry film is

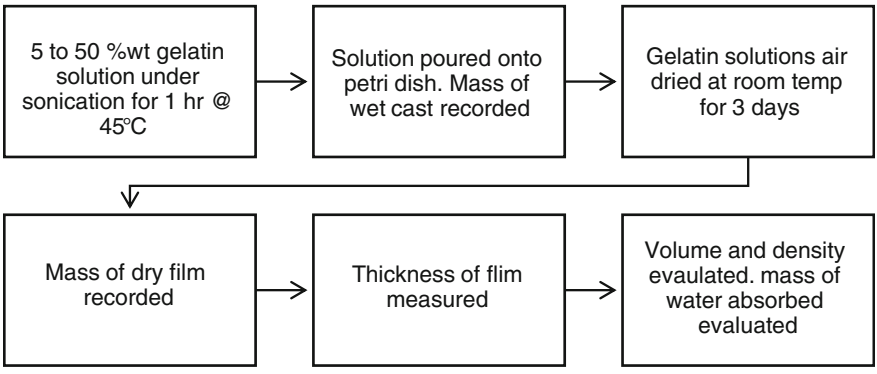


**Fig. 4.2** Fabrication of gelatin films (*GF*) under ambient conditions

**Fig. 4.3** Specimens of fabricated GF from 5.0 to 50 wt%

recorded. After recording the mass of dry film, the thickness of the films is measured using a micrometer. An average value of six measurements at random points of the film is taken to be the thickness. In addition, the mass of water absorbed in the film is determined by the difference in mass of the dry film with the original mass of gelatin. The fabrication of GFs is necessary to evaluate the microstructure of gelatin as a single constituent and how it may bind on the hydrophobic surface coating of the aerogels. The films are investigated for density, strength, modulus, thermal conductivity and for chemical states variations in binding energy through XPS. The initial masses of the gelatin granules before adding water were from 0.3 to 3.0 g (corresponding to the 5–50 wt% concentration). The dry masses of the films after drying were recorded from 0.0212 to 0.0562 g suggest that there was negligible amount of water absorbed thus the data shown are reasonable estimates of the gelatin granules. The median density of the films was evaluated to be 0.9224 g/cm$^3$ following a nonlinear Gaussian function curve fitting produced $R^2 = 0.993$ fit.

X-ray photoelectron spectroscopy (XPS) is used in determining the chemical compositions and chemical states of the silica aerogels, gelatine and the composites using KRATOS Axis Ultra shown in Fig. 4.4. The chemical composition analysis of the gelatin films in the range of 5–50 wt% were determined using Al Kα radiation of 15 kV, 30 mA operated at 450 W. The relative difference in composition will provide useful information of possible binding sites and patterns in the composites. XPS can also be used to measure thickness of thin films and depth profiling, but in the current study, these features are not used.

XPS is based on the photoelectric effect principle of the ejection of electrons from a surface when the photons impinged upon it. The source of photon energies used is Al Kα. The energy of the photoelectrons leaving the surface of a specimen gives a spectrum with a series of photoelectron peaks in terms of binding energy

| KRATOS Axis Ultra XPS/ESCA Specification | |
|---|---|
| **Source:** | Al Kα , Mg Kα |
| **Power (W)** | 450 |
| **Min spot size (μm)** | <15 |
| **Chemical State imaging mode (μm)** | <7 |

**Fig. 4.4** KRATOS axis ultra XPS/ESCA specification

BE. These peaks can be used to determine the composition of the specimen as well as the type of bonds that exist in the specimen. XPS, however, cannot detect the elements Hydrogen and Helium.

The chemical compositions that exist in the gelatin would give us an idea of the elements that may be responsible for the binding onto the aerogel surface. Elementally, gelatin is made of carbon, oxygen, nitrogen and hydrogen (Smitha et al. 2007). Figure 4.5 shows the ESCA spectrum of O-1s, C-1s and N-1s of the GF. There is a uniform shift in the binding energy of 2.7 eV as C-1s is observed to be at 287.2 eV as compared to the theoretical value of 284.5 eV (Moulder et al. 1995). This is due to charging effect of the specimens. All peaks are calibrated against C-1s, the peak for O-1s is 530.7 eV, and N-1s is 399.3 eV, respectively.

Table 4.1 shows the composition of the three major elements in the gelatin films in terms of binding energy (BE), energy at full width half-max (FWHM) and mass concentration in percentage. From the data in the table, the compositions of O-1s, C-1s and N-1s across various percentages of GF show consistent readings of 24.58 ± 0.77, 60.39 ± 1.09 and 14.99 ± 0.74 %, respectively. The values determined

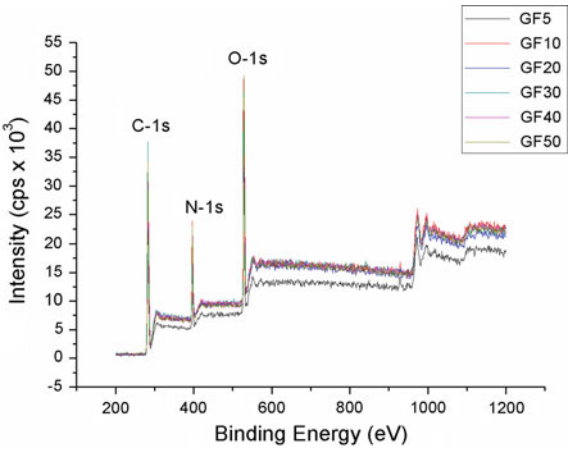


**Fig. 4.5** XPS/ESCA wide scan spectrum of various mass fraction of GF

**Table 4.1** Elemental composition of gelatin films

| Sample | Position BE (eV) | | | FWHM (eV) | | | Mass concentration % | | |
|---|---|---|---|---|---|---|---|---|---|
| | O 1s | N 1s | C 1s | O 1s | N 1s | C 1s | O 1s | N 1s | C 1s |
| GF5 | 530.4 | 399.1 | 284.5 | 2.078 | 1.418 | 2.296 | 23.99 | 15.29 | 60.72 |
| GF10 | 530.5 | 399.2 | 284.5 | 2.273 | 1.439 | 2.332 | 25.58 | 15.47 | 58.95 |
| GF20 | 530.7 | 399.4 | 284.5 | 2.523 | 1.405 | 2.393 | 24.56 | 14.33 | 61.1 |
| GF30 | 530.8 | 399.3 | 284.5 | 2.326 | 1.38 | 2.218 | 24.59 | 13.63 | 61.78 |
| GF40 | 530.7 | 399.2 | 284.5 | 2.355 | 1.407 | 2.44 | 24.46 | 15.48 | 60.06 |
| GF50 | 530.8 | 399.3 | 284.5 | 2.426 | 1.442 | 2.29 | 26.04 | 14.68 | 59.28 |
| Mean | **530.7** | **399.3** | **284.5** | **2.33** | **1.42** | **2.33** | **24.87** | **14.81** | **60.32** |
| Median | **530.7** | **399.3** | **284.5** | **2.34** | **1.41** | **2.31** | **24.58** | **14.99** | **60.39** |
| Std Dev | **0.16** | **0.10** | **0.00** | **0.15** | **0.02** | **0.08** | **0.77** | **0.74** | **1.09** |

do not include the concentration of hydrogen, although it can be assumed approximately 6 %. Elemental analysis of commercial gelatin is reported as carbon, 50.5 %; hydrogen, 6.8 %; nitrogen, 17 % and oxygen 25.2 % (Thomas 1998). The narrow spectrums of the individual elemental peaks were further analyzed to determine their possible chemical states that exist in the gelatin are shown in subsequent tables and figures.

The N-1s core-level spectrum exhibits a single component at 399.3 eV assigned to the free $–NH_2$ groups. The spectrum shows that the N-1s binding energy has a slight peak shift in the strength of small variation of 0.3 eV with increasing concentration, which could be attributed to a slight effect of intramolecular hydrogen bonding within the gelatin network. This is evident from a larger variation in the N/O ratio (0.63–0.73) in Table 4.2. Xu et al. (2012) investigated the effect of aggregation behavior of gelatin-grafted glycidol in aqueous solution reported similar trend on the free $–NH_2$ groups hydrogen bonding.

**Table 4.2** Percentage atomic concentration and elemental ratio of gelatin films

| Sample | Atomic concentration % | | | Calculated elemental ratio | | |
|---|---|---|---|---|---|---|
| | O 1s | N 1s | C 1s | N/C | O/C | N/O |
| GF5 | 19.61 | 14.28 | 66.11 | 0.22 | 0.30 | 0.73 |
| GFl10 | 21.01 | 14.51 | 64.48 | 0.23 | 0.33 | 0.69 |
| GF20 | 20.08 | 13.38 | 66.54 | 0.20 | 0.30 | 0.67 |
| GF30 | 20.08 | 12.72 | 67.2 | 0.19 | 0.30 | 0.63 |
| GF40 | 20.03 | 14.48 | 65.5 | 0.22 | 0.31 | 0.72 |
| GF50 | 21.39 | 13.77 | 64.84 | 0.21 | 0.33 | 0.64 |
| Mean | 20.37 | 13.86 | 65.78 | 0.21 | 0.31 | 0.68 |
| Median | 20.08 | 14.03 | 65.81 | 0.21 | 0.30 | 0.68 |
| Std Dev | 0.68 | 0.71 | 1.03 | 0.01 | 0.01 | 0.04 |

Unlike N-1s, three distinct peaks can be found on C-1s at 284.4 ± 0.1 eV (C-1s1), 285.5 ± 0.17 eV (C-1s3) and 287.5 ± 0.07 (C-1s2) eV which corresponds to C–C, C–N and $COO^-$ and/or C=O bonds in the GF (Moulder et al. 1995; Koul et al. 2011), respectively, as shown in Fig. 4.6a.

The peaks of C-1s1 and C-1s2 bonds remain similar in shape at various quantities of gelatin fractions. But the C-1s3 (C–N) peaks appear to have tapered at 10–30 % before reappearing again at 40 % gelatin. Such a phenomenon was observed by Xu et al. (2012) attributing the reappearance of distinct peak coincides with the needle like formation of gelatin at higher concentration due to non-covalent interactions that include hydrogen bonding, van der Waals forces,

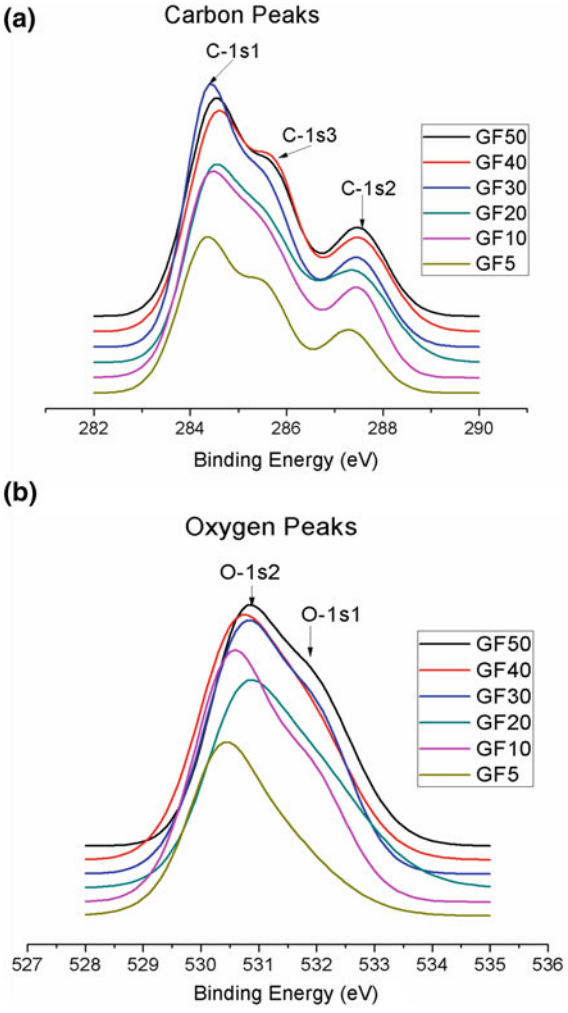


**Fig. 4.6** Distinct elemental peaks at various concentrations of GF films; (**a**) carbon C-1s and (**b**) oxygen O-1s

electrostatic interactions and hydrophobic effects. Similarly, O-1s has two distinct peaks at 530.6 ± 0.14 eV (O-1s2) and 531.8 ± 0.33 eV (O-1s1) which corresponds to O=C and $COO^-$ bonds, respectively (Xu et al. 2012) as shown in Fig. 4.6b. The XPS/ESCA analysis will be further deliberated in the next section for the GSA and GSA–SDS composites to detect the changes in the elemental ratio.

## 4.4 Microstructural Examination of Silica Aerogels and Their Composites

### *4.4.1 SEM/EDX Characterization*

The visual examinations are carried out via field emission scanning electron microscopy (FESEM) images from JSM7600 FESEM.EDX shown in Fig. 4.7. These high resolution images can be magnified up to one million times to investigate in nanoscale. The images facilitate visualisation of the microstructure of the materials at nanolevels. Figures 4.8a–b show the silica aerogel granules and visual examination of a single aerogel granule under SEM, respectively. Figure 4.8c shows the chemical structure and 4.8d, the microstructure of the magnified region where the 'pearl necklace' like structure and the nanopores are visibly seen as reported by Guo et al. (2013) and Zhong et al. (2011). The SEM pictures in Fig. 4.8e–f are the GSA–SDS composites where retention of the 'pearl necklace' like structure and visibility of nanopores are clearly seen suggesting that gelatin had bonded onto the hydrophobic surface with negligible penetration of the gelatin. Hence, there exists a possible reaction or physical adsorption between the carboxyl ($COO^-$) and free amides ($NH_2$) functional groups of the gelatin with the oxy-TMS groups of the silica aerogel. This has been verified when the same silica aerogel granules failed to bind with gelatin foamed solution when it was heated at 350°C

| JSM7600 FESEM/EDX Specifications | |
|---|---|
| **Resolution** | 1.0 nm @ 15kV |
| | 1.5nm (GB mode) |
| | 2.5nm (SEM Mode) |
| **Magnification** | |
| **LM mode** | X 25 – 19000 |
| **SEM mode** | X100 - 1000000 |
| **Prove Current (A)** | $10^{-15}$ to $2x10^{-7}$ |
| **Accelerating Voltage** | 0.5 -30 kV |

**Fig. 4.7** JSM7600 FESEM/EDX specification

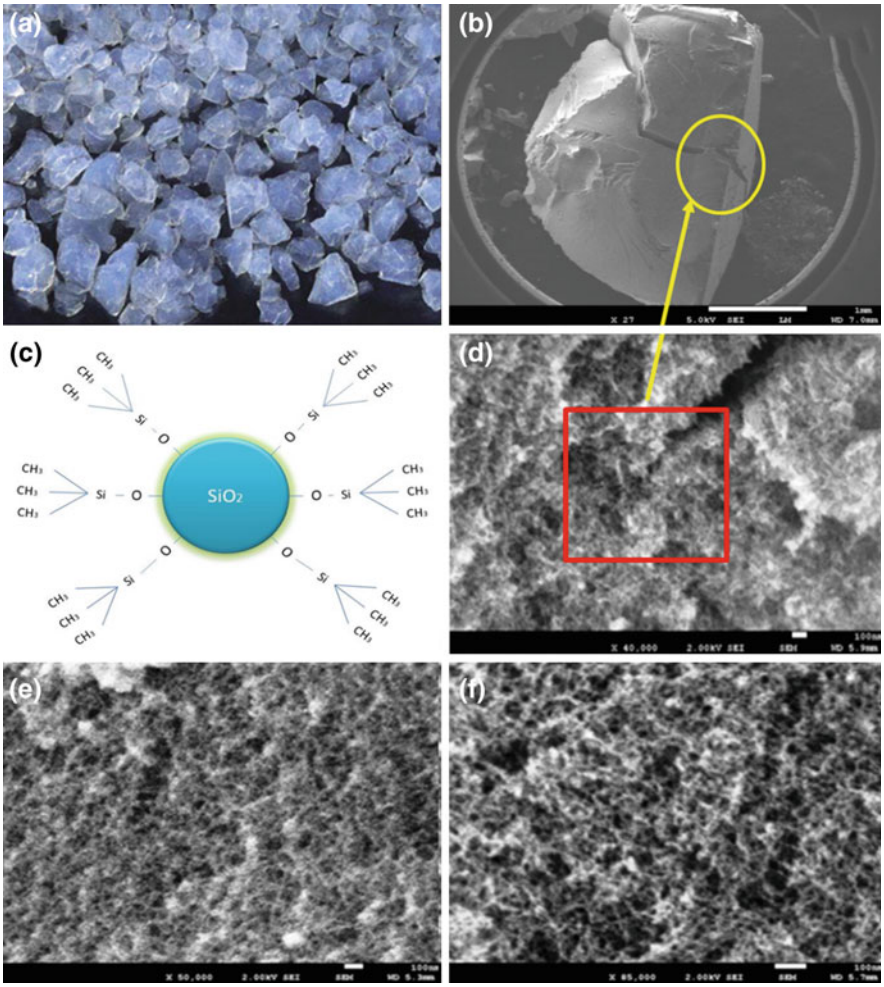


**Fig. 4.8** SEM pictures of (**a**) silica aerogel granules; (**b**) single silica aerogel granule under SEM; (**c**) chemical structure of aerogel; (**d**) pearl-like necklace structure of the aerogel with clear visualization of nano-pores (boxed in *red*); (**e**–**f**) GSA–SDS composite showing the retention of the silica aerogel pearl-like necklace structure suggesting non penetration of gelatin into pores and binding of gelatin onto the hydrophobic surface

before the mixing phase indicating that the oxy-TMS (Si–O–Si$(CH_3)_3$) groups had reverted to hydroxyl (Si–OH) groups by oxidation as reported previously by Rao et al. (2003). The foamed solution of gelatin and SDS induces large amount of air from the surrounding forming bubbles. This action enables air to be trapped between the silica aerogel granules during mixing.

While some of the trapped air escape via differential gas pressure inside the bubbles, some may not, thus remain trapped during the curing stage. The

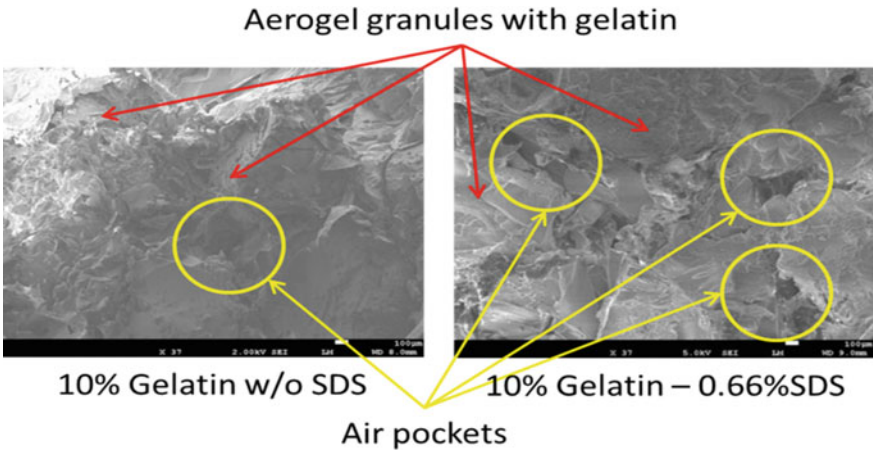


**Fig. 4.9** Existence of 'air pockets' in the GSA and GSA–SDS composite blocks

introduction of SDS into the gelatin solution increases the amount of bubbling, and therefore trapped air volume during the frothing stage. This can be observed from Fig. 4.8b where the volume of the composite block is increased significantly for the same amount of gelatin and hence reducing the density. The binding is further aided by adding the SDS having both the polar and nonpolar groups to bridge the hydrophobic groups of silica aerogel with polar groups of gelatin giving the added springiness in the interface between the aerogels and the foamed solution.

SEM picture in Fig. 4.9 shows a comparison between two specimens with and without SDS. It is clear that with GSA–SDS, there are more air pockets between the aerogel particles between the two specimens per unit area. The EDX data in Table 4.3 shows reduction of C but increase of Si and O elements on the surfaces of composites at the regions of air pockets between both specimens as a result of re-distribution of the gelatin content throughout the composite mix due to increased volume with the addition of SDS. This observation concludes that for composites having same gelatin content, the binding between the aerogel particles has significant amount of trapped air in the form of 'air pockets' when added with SDS that simultaneously increases its flexibility in the dried gelatin foam network. Thus the ability of these 'air pockets' to withstand the compressive load during testing result in a lower strength, higher strain recovery, and therefore transforming into a ductile polymer behavior (Ashby and Gibson 1997).

**Table 4.3** EDX data

| Specimen | Weight % | | |
|---|---|---|---|
| | Carbon | Silicon | Oxygen |
| 10 % Gelatin–0 % SDS | 51.30 | 12.29 | 35.84 |
| 10 % Gelatin–0.66 % SDS | 12.30 | 35.14 | 52.07 |

### 4.4.2 XPS/ESCA Surface Characterization

While the EDX data provide a general elemental composition of the composites, it does not provide enough details on the type of bonds that may possibly exist between the gelatin and the aerogels. This is essential to the future work that may involve the use of other types of binders. It was already mentioned in Sect. 4.4.1 that some form of interaction existed between gelatin and the aerogels as it was found that gelatin did not bind with the –OH group on aerogels (heat-treated). XPS characterization is carried out on selected specimens of GSA and GSA-SDS composites and compared with silica aerogel to determine the chemical states of the elements. In Fig. 4.10, there are two carbons peaks, 284.0 and 284.6 eV, with an atomic concentration of 0.75 and 20.4 %, respectively, on the aerogels. The peak at 284.6 eV is assigned to the methyl groups ($C–H_3$) from the oxy-TMS groups on the surface of aerogels (Moulder et al. 1995). The oxygen peak at 532.8 eV is assigned to the oxygen bonds in the $SiO_2$ clusters and the peak at 532.2 eV is assigned to the oxy-TMS groups (Wang et al. 1998). Similarly, the peak at 103.4 eV is assigned to the silicon content in $SiO_2$ aerogel cluster and 103.9 eV is assigned to Si–C bonds in oxy-TMS groups (Jerzy and Carl 1984; Jo et al. 1997; Yang et al. 1999).

In Table 4.4, the loss of N 1s peaks in the composites suggest that the free $–NH_2$ groups have undergone hydrogen bonding with the aerogels aided by the reducing elemental ratio Si:C shown in Table 4.5. This indicates that the some of the oxy-TMS groups would have participated in the reaction with $–NH_2$ groups. At the same time,

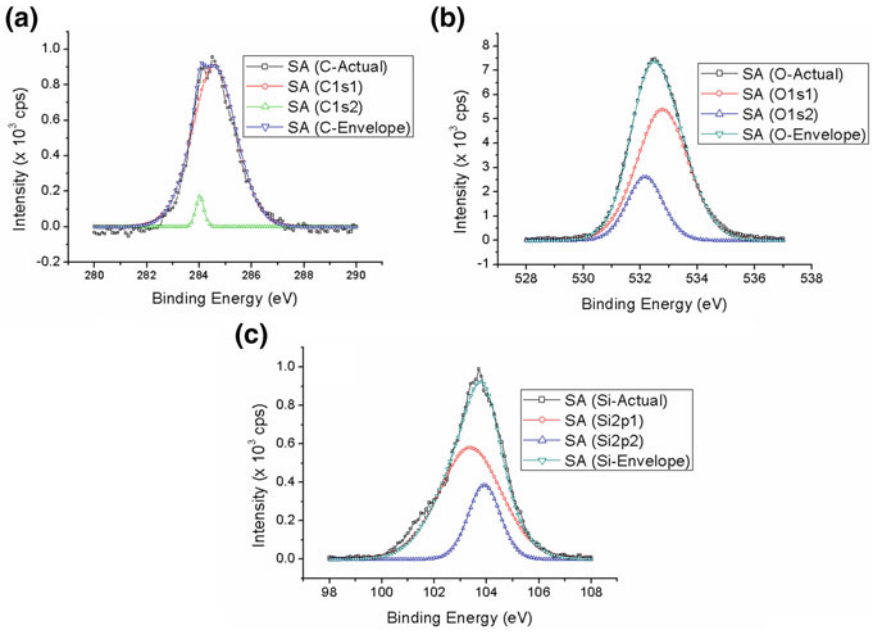


**Fig. 4.10** Silica aerogel elemental peaks; (**a**) carbon; (**b**) oxygen and (**c**) silicon

**Table 4.4** Binding energy position and percentage atomic concentration of composites

| Sample | Position BE (eV) | | | | Atomic concentration % | | | |
|---|---|---|---|---|---|---|---|---|
| | O 1s | N 1s | C 1s | Si 2p | O 1s | N 1s | C 1s | Si 2p |
| GSA | 532.4 ± 0.2 | 400.5 ± 0.6 | 284.5 | 103.7 ± 0.1 | 46.6 ± 0.7 | 0.5 ± 0.3 | 26.6 ± 0.9 | 26.3 ± 0.6 |
| GSA-SDS | 532.4 ± 0.1 | 399.8 ± 0.4 | 284.5 | 103.6 ± 0.2 | 51.3 ± 0.5 | 0.5 ± 0.2 | 24.5 ± 0.4 | 25.4 ± 0.6 |
| SA | 532.5 | – | 284.5 | 103.7 | 53.7 | – | 21.1 | 25.2 |
| GF | 530.7 ± 0.2 | 399.3 ± 0.1 | 284.5 | – | 20.1 ± 0.1 | 14.0 ± 0.1 | 65.8 ± 0.2 | – |

**Table 4.5** Elemental ratio of composites

| Sample | Calculated elemental ratio | | | | | |
|---|---|---|---|---|---|---|
| | N/C | O/C | N/O | Si/C | Si/O | Si/N |
| GSA | 0.019 | 1.751 | 0.011 | 0.988 | 0.564 | 51.049 |
| GSA-SDS | 0.019 | 2.092 | 0.009 | 1.038 | 0.496 | 55.283 |
| SA | – | 2.548 | – | 1.196 | 0.470 | – |
| GF | 0.214 | 0.304 | 0.678 | | | |

the lower Si:O ratio of composites with SDS indicates that not all of the oxy-TMS groups on the aerogel bond due to increase in O 1s with the addition of SDS.

Figure 4.11a shows the breakdown of the Si-2p peaks in aerogels and the various compositions of composites. Si–O peaks at 103.4 eV were relatively constant at 20 ± 2 % for the aerogels and the composites. The aerogels has another small peak at 103.9 eV which was identified as the Si–$OR_3$ (R=$CH_3$). However, this peak shifted to 101.5 eV for the composites which has been identified as Si–$OR_x$ suggests possible reduction of methyl groups or a loss of hydrogen that reacted with the free –$NH_2$ groups of the gelatin resulting in the lower binding energy. The reduction in the atomic concentration from 6.44 to 3.75 % on the oxy-TMS groups also points to the above postulation.

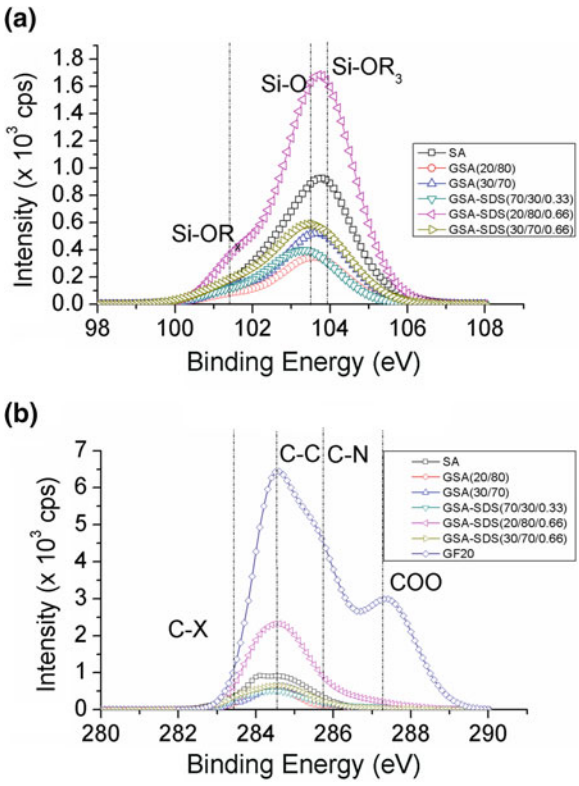


**Fig. 4.11** Comparison of (**a**) carbon and (**b**) silicon chemical states in silica aerogel, GSA, GSA-SDS and gelatin

The C-1s peaks in Fig. 4.11b showed that the $COO^-$ and C–N peaks had disappeared and a new C–X at 283.6 eV appeared in the composites. The new peak has 1.1–1.9 % atomic concentrations which could be hydrocarbon or carbon–carbon bond. Similarly, the O-1s(2) composition in the composites shows a reduced percentage level as compared to aerogels. The XPS data affirmed the initial postulation that there is some reaction between the aerogels and the gelatin as seen from the shift on the $Si–OR_3$ binding energy of the composite and as well as the disappearance of the C–N and $COO^-$ peaks that were distinct in the gelatin films but not in the composite. Essentially, for a material to bind with aerogels, it must possess free $NH_2$ groups in more than 14 % concentration and with COOH groups.

## 4.5 Concluding Remarks

XPS/ESCA carried out on the gelatin film provided some vital information on the chemical structure and composition. The variations in the peaks of the binding energy gave an overview of the various bonds existed in the gelatin. The N-1s displayed a single peak that corresponds to the free $NH_2$ groups in the gelatin. Likewise, similar matching of the peaks to the possible bonded groups was evaluated using the standard reference in Handbook of X-ray photoelectron spectroscopy (Moulder et al. 1995). It can be concluded that besides the C–C bonds chains, gelatin has other C–N and $COO^-$ and/or C=O bonds in its structure. XPS investigation of the chemical states of the composites in comparison with gelatin films and neat silica aerogel granules prove that free $NH_2$ groups are responsible for the binding between the surface of the silica aerogel granules and gelatin although lower concentrations levels of $NH_2$ prevented full bonding with oxy-TMS groups. It is also observed that the carboxyl groups in gelatin aided in the hydrogen bonding with water and with the silica aerogel granules while SDS ensures uniformity in binding by bridging the polar and non-polar groups.

## References

Ashby, M.F., and L.J. Gibson. 1997. *Cellular Solids—Structure and Properties*. Cambridge: Cambridge University Press.

Fidler, C., and T.C. Simonton. 1996. *Aerogel-in-foam Thermal Insulation and its Preparation*. Lancaster, PA: United States, Armstrong World Industries, Inc.

Fidler, C., and T.C. Simonton. 2000. *Aerogel-in-foam Thermal Insulation and its Preparation*. United States, Armacell LLC (DE).

Guo, J., B.N. Nguyen, L. Li, M.A.B. Meador, D.A. Scheiman, and M. Cakmak. 2013. Clay reinforced polyimide/silica hybrid aerogel. *Journal of Materials Chemistry A* 1(24): 7211–7221.

Jerzy, H.M., and M.L. Carl. 1984. High-resolution electron microscopy study of silica aerogel transparent insulation. 28th SPIE annual international technical symposium, August 19–24, 1984, San Diego, CA.

Jo, M.-H., J.-K. Hong, H.-H. Park, J.-J. Kim, S.-H. Hyun, and S.-Y. Choi. 1997. Application of SiO2 aerogel film with low dielectric constant to intermetal dielectrics. *Thin Solid Films* 308–309: 490–494.

Koul, V., R. Mohamed, D. Kuckling, H.-J.P. Adler, and V. Choudhary. 2011. Interpenetrating polymer network (IPN) nanogels based on gelatin and poly(acrylic acid) by inverse miniemulsion technique: synthesis and characterization. *Colloids and Surfaces B: Biointerfaces* 83(2): 204–213.

Moulder, J.F., J. Chastain, and R.C. King. 1995. Handbook of X-ray photoelectron spectroscopy: a reference book of standard spectra for identification and interpretation of XPS data/by John F. Moulder … [et al.]. In *Physical Electronics* edited by Jill Chastain, Roger C. King, Jr., Eden Prairie, Minn, 1995.

Rao, A.V., M.M. Kulkarni, G.M. Pajonk, D.P. Amalnerkar, and T. Seth. 2003. Synthesis and characterization of hydrophobic silica aerogels using trimethylethoxysilane as a co-precursor. *Journal of Sol-Gel Science and Technology* 27(2): 103–109.

Smitha, S., P. Mukundan, P. Krishna Pillai, and K.G.K. Warrier. 2007. Silica-gelatin bio-hybrid and transparent nano-coatings through sol-gel technique. *Materials Chemistry and Physics* 103 (2–3): 318–322.

Thomas, K. 1998. *Gelatin. Handbook of Biodegradable Polymers*. Boca Raton: CRC Press.

Wang, S.-J., I.-S. Jin, and H.-H. Park. 1998. X-ray photoelectron spectroscopic analysis on plasma-etched SiO2 aerogel with CHF3 gas. *Surface and Coatings Technology* 100–101: 59–64.

Xu, J., T.-D. Li, X.-L. Tang, C.-D. Qiao, and Q.-W. Jiang. 2012. Effect of aggregation behavior of gelatin in aqueous solution on the grafting density of gelatin modified with glycidol. *Colloids and Surfaces B: Biointerfaces* 95: 201–207.

Yang, H.-S., S.-Y. Choi, S.-H. Hyun, and C.-G. Park. 1999. Ambient-dried SiO2 aerogel thin films and their dielectric application. *Thin Solid Films* 348(1–2): 69–73.

Zhong, Y.-H., B. Zhou, J.-Y. Gui, Y.-N. Li, A. Du, J. Shen, G.-M. Wu, and Z.-H. Zhang. 2011. Low-density carbon aerogels fabrication and its thermal and mechanical properties. *Yuanzineng Kexue Jishu/Atomic Energy Science and Technology* 45(10): 1170–1176.

# Chapter 5
# A New Phenomenon—Brittle to Ductile Transition

## 5.1 Introduction

Most published literature analyzed the elastic modulus of silica aerogels by drawing inspiration from the cellular solids models. For example, Ashby and Gibson (1997) describe the open cellular foam model compressive modulus to follow power law dependence on the relative density as shown in Eq. (5.1) where $C$ and $\mu$ are geometric constants that depend on the topological features and microstructure undergoing cell wall bending as the dominant deformation.

$$\left(\frac{E}{E_s}\right) = C\left(\frac{\rho}{\rho_s}\right)^{\mu} \tag{5.1}$$

Ashby and Gibson (1997) illustrated the model as a cubic array of interconnected beams as shown in Fig. 5.1 with an exponent of 2. Similarly for closed-cell foam, Ashby and Gibson approximated the relative modulus with an additional term accounted for internal gas pressure and membrane stresses on the faces as shown in Table 5.1.

Mills and Zhu (1999) developed the closed-cell and opened-cell foams using the BBC lattice tetrakaidecahedral cell model were as shown in Table 5.1 where $ø_s$ is the volume fraction of solids in the cell edges (Zhu et al. 1997a, b; Mills and Zhu 1999). Roberts and Garboczi (2001, 2002) investigated the modulus for both opened-cell and closed-cell foam structure of random models based on Voronoi tessellations and level-cut Gaussian random fields for a closed-cell tetrakaidecahedral model shown in Fig. 5.2. Lu et al. (1999) proposed macro-mechanic model to evaluate the modulus for low porosity.



M. Sachithanadam and S.C. Joshi, *Silica Aerogel Composites*,
Engineering Materials, DOI 10.1007/978-981-10-0440-7_5

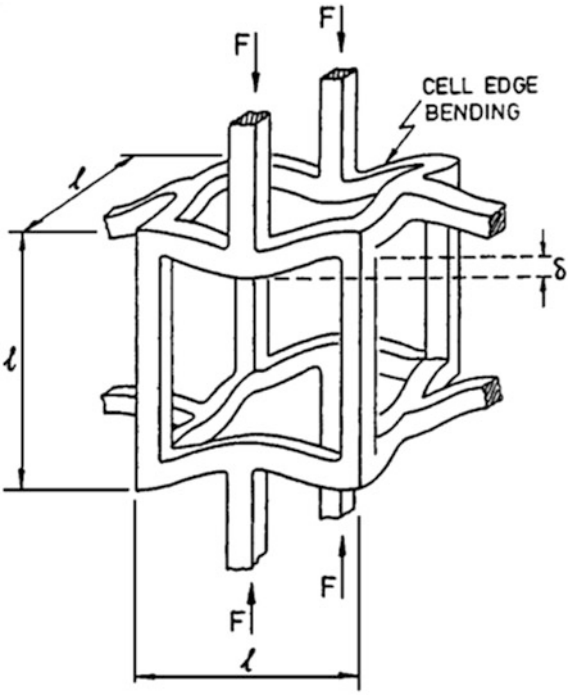


**Fig. 5.1** Cell edge bending of an idealized open-celled foam (Ashby and Gibson 1997)

### *5.1.1 Parametric Model*

The study of highly nanoporous material like aerogel is very complex as the final properties are significantly affected by the process parameters. Significant developments and theories have been formulated to characterize the mechanical properties of aerogel. The elastic Young's modulus ($E_a$) of aerogels is probably the most researched mechanical property over the past few decades (Woignier et al. 1989, 1998; Groβ and Fricke 1995; Scherer et al. 1995a, b; Emmerling and Fricke 1997; Alaoui et al. 2008) employing various techniques.

Woignier et al. (1989) used the three-point flexural technique to determine the $E_a$ of an aerogel prepared via sol gel technique concluding that the process parameters such as concentration of silicon compounds, catalytic conditions, and the preparation conditions affect the Young's modulus. They concluded that the $E_a$ obeys the power law dependence relative to its density with the exponent of 3.7.

Scherer et al. (1995a, b) investigated the bulk modulus using mercury porosimetry method. They observed that the silica aerogels are linearly elastic under small strains. Thereafter, they exhibit yield followed by densification and plastic hardening. Scherer and his co-workers found that the bulk modulus of the silica aerogel has a power law dependence on density with an exponent of 3.2 in the plastic regime and the linear elastic modulus with an exponent of 3.6 (Scherer 1995a, b), noting the behavior strongly resembles that of a polymeric foam (Ashby

**Table 5.1** Cellular foam models

| Type | Model | Reference |
|---|---|---|
| Opened cell (interconnected beams) | $\left(\frac{E}{E_s}\right) = C\left(\frac{\rho}{\rho_s}\right)^2$ | Ashby and Gibson (1997) |
| Closed cell (interconnected beams) | $\left(\frac{E}{E_s}\right) \approx \text{ø}^2\left(\frac{\rho}{\rho_s}\right)^2 + (1-\text{ø})\frac{\rho}{\rho_s} + \frac{p_0(1-2v)}{E_s\left(1-\rho/\rho_s\right)}$ where $v \approx \frac{1}{3}$, ø is the variable solid fraction and $p_0$ is the gas pressure in the cell | Ashby and Gibson (1997) |
| Closed cell (BCC lattice tetrakaidecahedral) | $\left(\frac{E}{E_s}\right) = 0.0598\left(\frac{\rho}{\rho_s}\right)^{1.066}$ for $0.015 < \frac{\rho}{\rho_s} < 0.1$<br>$\left(\frac{E}{E_s}\right) = 0.0807\left(\frac{\rho}{\rho_s}\right)^{1.155}$ for $\text{ø}_s = 0.93$<br>$\left(\frac{E}{E_s}\right) = 0.977\left(\frac{\rho}{\rho_s}\right)^{1.627}$ for $\text{ø}_s = 0.6$ | Zhu et al. (1997a), Mills and Zhu (1999) |
| Opened cell (BCC lattice tetrakaidecahedral) | $\left(\frac{E}{E_s}\right) = 0.7258\left(\frac{\rho}{\rho_s}\right)^2$ for $0.015 < \frac{\rho}{\rho_s} < 0.1$ | Zhu et al. (1997b) |
| Closed cell (BCC-Voronoi tessellation) | $\left(\frac{E}{E_s}\right) = 0.64\left(\frac{\rho}{\rho_s}\right)^{1.4}$ (20 % cell wall deleted at random)<br>$\left(\frac{E}{E_s}\right) = 0.76\left(\frac{\rho}{\rho_s}\right)^{1.7}$ (40 % cell wall deleted at random)<br>$\left(\frac{E}{E_s}\right) = \left(\frac{\rho}{\rho_s}\right)^2$ (70 − 85 % cell wall deleted at random) | Roberts and Garboczi (2001) |
| Opened cell (BCC-Voronoi tessellation) | $\left(\frac{E}{E_s}\right) = 4.2\left(\frac{\rho}{\rho_s}\right)^{3.5}$ for $0.05 < \frac{\rho}{\rho_s} < 0.2$ | Roberts and Garboczi (2002) |
| Macro-mechanics | $\left(\frac{E}{E_s}\right) \approx (1-2\text{ø})(1+4\text{ø}^2)$, where ø < 30 % | Lu et al. (1999) |

and Gibson 1997). However, the inability for mercury to penetrate into the aerogel showed the analysis done using the pore size distribution is unreliable and inconclusive (Scherer 1995a, b). Groβ and Fricke (1995) evaluated the Young's modulus via ultrasound technique and explained that most aerogels are fractal over less than one order of magnitude in length and therefore, concluded that there is no necessity for fractal concepts to be included and used the Kelvin Voigt bars model to explain the observed scaling exponents in aerogels by adjusting the geometric parameters. They concluded that the $E_a$ obeys the power law dependence relative to its density with the exponent of 2.0–4.5.

Emmerling and Fricke (1997) proposed that there is a strong relationship between the morphological and topological features of fractal gel networks and properties such as elasticity and solid thermal conductivity of the aerogels. They

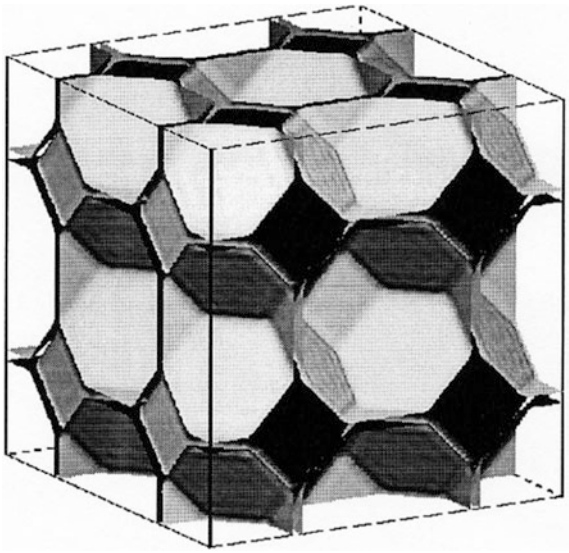

**Fig. 5.2**
The tetrakaidecahedral model corresponds to the Voronoi tessellation of a body-centered cubic lattice (Roberts and Garboczi 2001)

investigated that the scaling exponent is functional of the mass fractal dimension ($D$), as shown in Eq. (5.2) and the exponent ranges from 2.6 to 3.8 attributed due to increase in the dangling mass effect.

$$\frac{E}{E_s} \propto \left(\frac{\rho}{\rho_s}\right)^{\mu}, \quad \text{where} \quad \mu = \frac{5-D}{3-D} \tag{5.2}$$

However, Woignier et al. (1998) argued that exponent is not a function of cluster features and dangling mass effect but instead a function of connectivity in agreement with Ma et al. (2000) who also showed from diffusion-limited cluster–cluster aggregation (DLCA) finite element simulation that for a perfectly connected silica network, the exponent does not go beyond 3.6. Their model based on blobs and links suggests that the high exponent is largely due to the reduction in connectivity of the material with decreasing density. Ma et al. (2001) further added that the opened-cell foam model predicted by Ashby and Gibson (Ashby and Gibson 1997) which follows the exponent of 2 is valid only when the connectivity remains unchanged with variation of the density and bending as the dominant mode of failure. It was also shown that through combination of DLCA and dangling mass algorithm (Ma et al. 2001), the exponent was between 3 and 4.

The approaches discussed so far suggest that silica aerogels have complexly networked structures that the final properties depend not only on the topological features but also on the process parameters. For certain, most of the authors used density as the single most important physical property in their analysis. Hence, the models and proposed theories could only provide an estimate of the real values. Nevertheless, both the cellular foam and parametric models revealed a certain

commonality; that is, they led to a simplified formulation that relates the relative modulus to the relative density in the form of power law dependence.

### 5.1.2 Direct Experimental Measurements

Parmenter and Milstein (1998) investigated mechanical properties of silica aerogels with fiber reinforcement. It was reported that neat aerogel have a compressive strength of 1.01 MPa and a hardness of 5.37 MPa. The compressive strength and hardness generally exhibited lower values with increasing amount of fibre reinforcement. The works carried out by Parmenter and Milstein (1998) had certain limitations especially in the case of handling of aerogels. Microcracks were noted during testing and given the brittle nature of these aerogels the results did not truly reflect the properties. Moner-Girona et al reported on the mechanical properties with nondestructive micro-indentation technique (Moner-Girona et al. 1999) which prevents cracking of the aerogels since the indentation loads were approximately 1 mN. They reported that silica aerogels showed two different behaviors; low-density silica aerogels are elastic while the denser ones behave as elastic-plastic materials. The Young's modulus was observed to be in the range between 7.0 and 346 MPa with increasing densities from 80 to 260 kg/m$^3$. However, this technique may possibly overestimate the properties of the silica aerogels since the load is very small. Another technique employed by Obrey et al using the chemical vapor deposition with silicon derivative layers on a monolithic silica aerogel, have observed a sixfold increase in compressive modulus to about 8.77 MPa (Obrey et al. 2011).

## 5.2 Experimental Setup

Compression tests are carried out as per ASTM C165 and ASTM D1621 using the Instron 5569 Universal Testing Machine as shown in Fig. 5.3. Each GSA and GSA–SDS sample was cut into a square specimen of $x$–$y$ dimensions of 17.5 ± 2.5 width 27.5 ± 1.5 mm height (in $z$-direction) using razor blades. The blocks were compression tested in the $z$-direction at three strain rates, viz, 0.8/min, 1.2/min at the nominal strain up to 44.4 %, and at 1.0/min. Each specimen was loaded in compression using 500 N ± 4 % load cell with the initial load of 25 % of the nominal strain for 1 min and, thereafter was unloaded. The compressive modulus for each specimen is calculated with the in-built Instron Bluehill software.

The amount of strain recovery was measured after 1 min upon unloading. The expression for strain recovery is shown in Eq. (5.3). Total of 172 specimens from the first fabrication process (via FM method) were tested for strain recovery at various strains, of which, 17 specimens had zero strain recovery.

| Instron 5569 Load Frame Specification | |
|---|---|
| **Load capacity (kN)** | 50 |
| **Max speed (mm/min)** | 500 |
| **Min speed (mm/min)** | 0.005 |
| **Max force at full speed (kN)** | 25 |
| **Max speed at full load (mm/min)** | 250 |
| **Load measurement accuracy** | ±0.4% |
| **Strain Measurement accuracy** | ±0.5% |

**Fig. 5.3** Specifications of Instron 5569 universal testing machine used in the compression experiments of the composites

$$\mathrm{SR} = \left(1 - \frac{\Delta L}{\mathrm{CS}}\right) \times 100\,\% \tag{5.3}$$

where SR = strain recovery, CS = compressive strain (mm), and, $\Delta L$ = change in length of specimen due to compression (mm)

Failed specimen analysis was carried out to purge out the redundant data, which is defined as a specimen already failing at first level but having duplicate data at higher levels. The 'Failed Specimen Analysis' is shown in Appendix 5A. In addition, 55 FD specimens were tested for strain recovery, strength and modulus at 45 % compressive strain as part of the validation data. The data include 40 specimens that were studied for the influence of the silica aerogel granule size on the mechanical properties.

Similarly, the fabricated GFs are also tested for the strength and the modulus. Each GF sample is cut into a standard specimen of gauge length 27.5 ± 2.5 mm. Three specimens from each sample are tested for strength and modulus in accordance with ASTM D882-12 procedures on INSTRON 5547 Micro Tester. The specimens are tensile strained in the $z$-direction at a strain rate of 1.0/min using 2 kN ± 4 % calibrated load cell. Figure 5.4a, b show the median values of modulus and strength of the gelatin films of various mass fractions. The modulus is evaluated to follow a parabolic curve of $R^2 = 0.999$ and the strength follows a cubic function of $R^2 = 0.877$ with a range of 1.6–2.5 GPa and 33–62 MPa with increasing gelatin content, respectively.

The properties of GF evaluated are essential in determining the properties of GSA and GSA–SDS composites. The process variables affecting or influencing the behavior of the GSA and GSA–SDS composites fabricated via FM are studied in detail via ANOVA design of experiment technique. ANOVA statistical tool is utilized to gage the process variables that have significant effect on the composites properties.

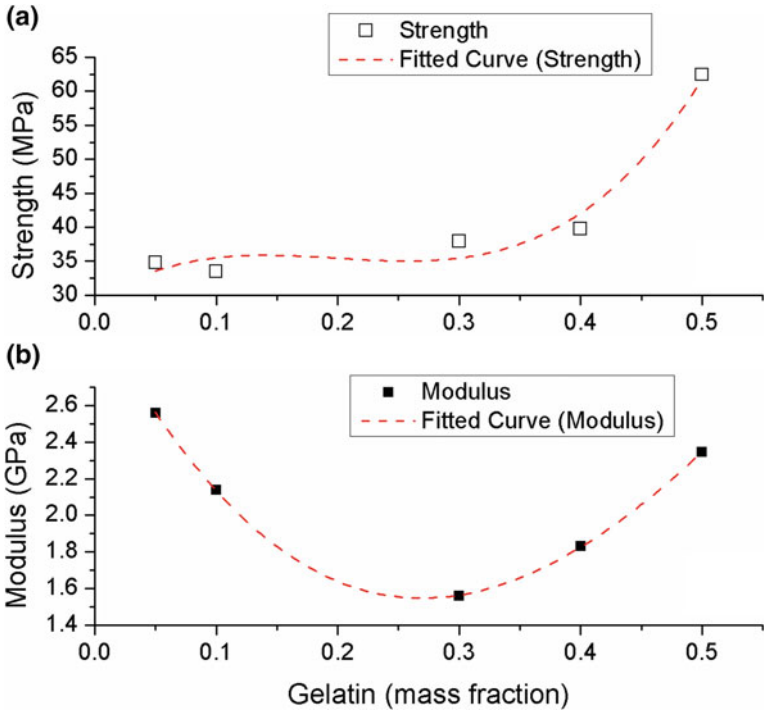


**Fig. 5.4** **a** Strength; **b** modulus of GF as a function of gelatin mass fraction

## 5.3 GSA and GSA–SDS Composites (FM Method)

### *5.3.1 Compressive Stress–Strain Behavior (FM Composites)*

It was established during the fabrication of the GSA and the GSA–SDS composites, that frothing of gelatin solution improves the overall texture to produce consistent and uniform foam resulting in greater variation of composite blocks fabricated at a faster rate. The experimental stress–strain curves in Fig. 5.5a, b shows the transformation of brittle to ductile behavior with the addition of SDS (max 0.66 wt%) exhibiting three distinct regions analogous to creep-curve annotated as low strain zone (LSZ), high strain zone (HSZ), and densification. LSZ is defined as the region under less than 20 % compressive strain whereas HSZ refers to the region where the composites were subjected to 20–50 % compressive strain. Generally, beyond 50 % compressive strain, densification of the composites follows. The analyses in this chapter are restricted to the LSZ and HSZ regions.

The general trend of strain recovery measured after compression test on each specimen is shown in Fig. 5.6. The data points plotted are the median strain recovery as the functions of gelatin and SDS content as well as compressive strain. The addition of SDS improves the strain recovery to approximately 10 % over the

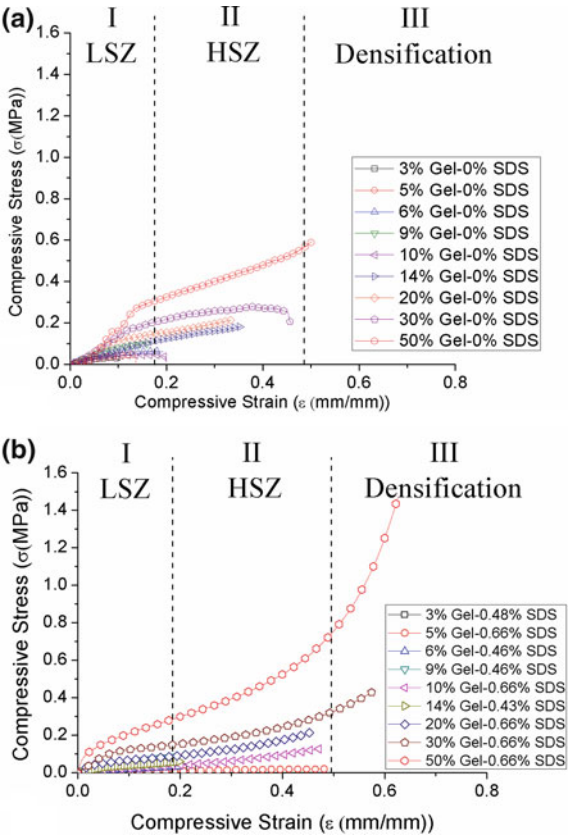


**Fig. 5.5** Stress–strain response curves of composites **a** GSA; **b** GSA–SDS

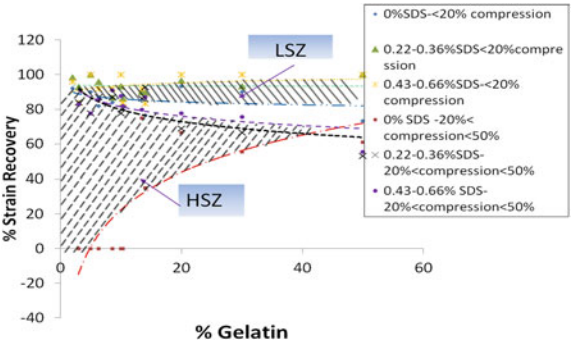


**Fig. 5.6** Composites strain recovery in terms of %Gelatin and %SDS

range of gelatin mass fraction in LSZ thus sustaining high % strain recovery of between 80 and 95 % as seen by the hatched region between the blue and yellow trend lines. This range is wider in HSZ as SDS has more significance in the strain recovery when subjected to high compressive strain whereas the strain recovery is only observable at above 10 % gelatin in GSA composites (annotated by red

trend-line). In contrast, the inclusion of SDS shows that the GSA–SDS composites are able to sustain good recovery of 70–90 % when subjected to high compressive strain for all mass fractions of gelatin setting up a converging envelope of strain recovery in the HSZ towards higher mass fractions of gelatin.

### 5.3.2 *Unusual Phenomenon—Brittle to Ductile Behavior*

A simplified schematic on the mechanism of the behavior is shown in Fig. 5.7. The linkages represented by SDS, together with the gas pressure within the dried gelatin

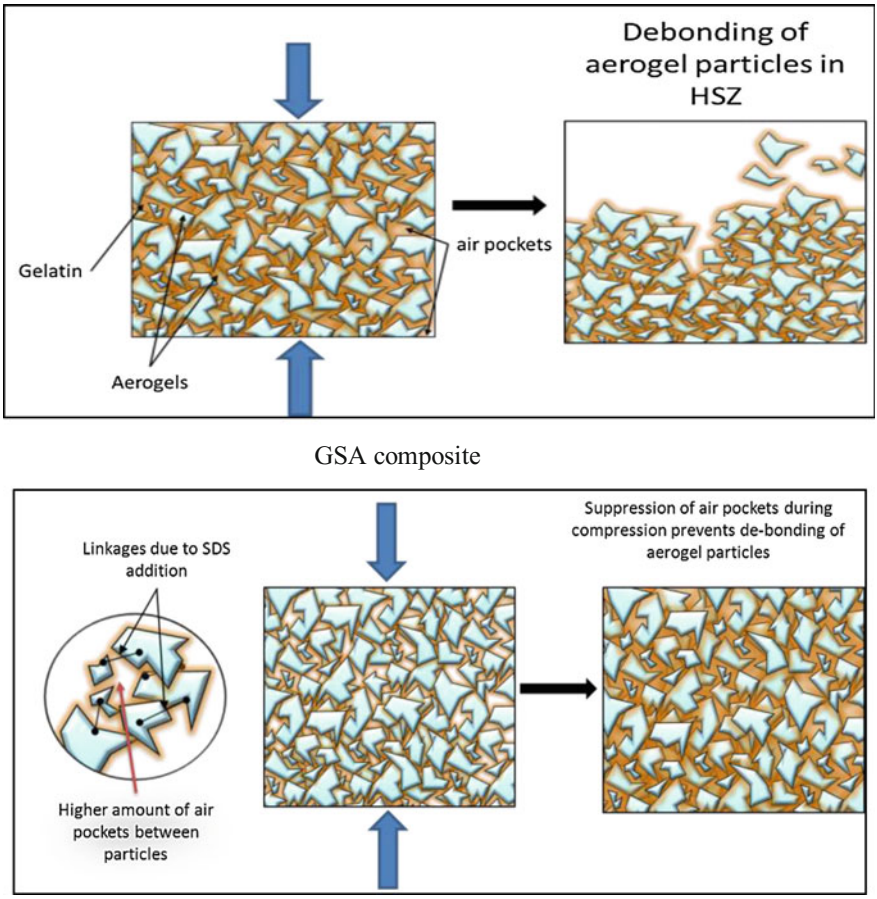


**Fig. 5.7** Schematic of the networked silica aerogel particles bonded with gelatin (*orange*) and linkages developed due to SDS polar and non-polar groups

network enables the particles in GSA–SDS composite to resist compressive load. During initial loading in LSZ, the pressure within the gelatin network provides huge resistance that causes steep slope in the stress–strain curve up to <20 %CS. Then the slope becomes more gradual with increasing %CS indicating that the pressure within the gelatin network is decreasing as annotated by HSZ in Fig. 5.5b. Upon unloading, the air re-enters the network and thus resulting in strain recovery. Figure 5.5a shows that without SDS, the composites fail prematurely in HSZ due to the de-bonding of the aerogel from gelatin and Fig. 5.5b shows sustained gradual increase of strength in HSZ with SDS thus preventing de-bonding of the particles from the gelatin network. However, further loading beyond HSZ will fully compress the network foam expelling all the trapped air but having densification as shown in stage III in Fig. 5.5b.

### 5.3.3 *Influence of SDS on Composite Properties from ANOVA*

Analysis of variance (ANOVA) is a procedure for assigning sample variance to different sources and deciding whether the variation arises within or among different population groups. It is an important tool in the designs of experiment (DOE) for comparing the variance from different data, investigating and identifying the factors, and interaction of the independent variables that have significant effects on the response variable (Besseris 2008; Alavi Nikje et al. 2009). ANOVA is especially useful where optimization of response variable is required (Sudharsan and Ng 2000). A full factorial design is used as the ANOVA technique in investigating and modeling an empirical relationship between the response variable and significant independent variables (i.e., the key parameters identified).

#### 5.3.3.1 Statistical Analysis of Measured Data

ANOVA is a useful and practical statistical tool in developing a model from scratch. ANOVA as a design of experiment tool has proven to aid in optimization studies (Sudharsan and Ng 2000; Meador et al. 2009), parametric and behavioral studies (Nguyen et al. 2009) and development of empirical models (Montgomery 2013). ANOVA uses different types of experimental design techniques and statisticians can deploy whichever strategy that is deemed adequate to their research.

In the experiments and studies carried out, a full quadratic empirical model including all main effects, second-order effects, and two- and three-way interactions were accounted via multiple linear regression analysis to determine the properties. Terms that were not significant in the model (<95 % confidence) were eliminated one at a time. The general empirical model for all the properties evaluated is given in Eq. (5.4). ANOVA present simple empirical formulation of the properties to be

evaluated based on the experimental data of the respective properties and the mass fraction of the constituent amounts.

$$\begin{aligned} Y = {} & \beta_0 + \beta_1 \mathrm{G} + \beta_2 \mathrm{S} + \beta_3 \mathrm{Sr} + \beta_4 \mathrm{C} + \mu_1 \mathrm{G}^2 + \mu_2 \mathrm{S}^2 + \mu_3 \mathrm{C}^2 + \gamma_1 (\mathrm{G} * \mathrm{S}) \\ & + \gamma_2 (\mathrm{G} * \mathrm{Sr}) + \gamma_3 (\mathrm{G} * \mathrm{C}) + \gamma_4 (\mathrm{S} * \mathrm{Sr}) + \gamma_5 (\mathrm{S} * \mathrm{C}) + \gamma_6 (\mathrm{C} * \mathrm{Sr}) \\ & + \emptyset_1 (\mathrm{S} * \mathrm{Sr} * \mathrm{G}) + \emptyset_2 (\mathrm{S} * \mathrm{C} * \mathrm{G}) + \emptyset_3 (\mathrm{C} * \mathrm{Sr} * \mathrm{G}) \\ & + \emptyset_4 (\mathrm{S} * \mathrm{Sr} * \mathrm{C}) + \emptyset_5 (\mathrm{S} * \mathrm{Sr} * \mathrm{G} * \mathrm{C}) \end{aligned} \tag{5.4}$$

where $Y$ = response of the property, G = gelatin, S = SDS, Sr = strain rate, C = compressive strain on the specimen, and, $(\beta, \mu, \gamma, \varnothing)$ = coefficients of main effects and interactions.

This technique helps to relate the mechanical and thermal properties to the physical properties in order to determine optimal values for further investigation. Thus, ANOVA is predominantly used in evaluating all the properties for the FM specimens. This above general empirical model is designed for the compressive modulus and strength evaluation. Therefore, the design of the model will have to be tweaked according to the property that is evaluated. For example it would not be appropriate to include strain rate as an input variable for evaluating thermal conductivity, but the mean temperature across the hot and cold boundary is a valid and essential variable. Therefore, the nomenclature of the model shall be adjusted to suit the property being evaluated.

Table 5.2 summarizes the significant effects of the main and interactive terms evaluated from the experiments carried out on the specimens. The empirical models based on Eq. (5.4) are developed from these significant terms for each property. As stated previously, parameters are evaluated to be significant if they show a $p$-value less than 0.05 (>95 % confidence). The $p$-value indicates the probability that a parameter is significant. Higher $p$-value corresponds to higher the probability of insignificance.

ANOVA showed that strain rate does not have any effect on any of the mechanical properties, thus the %Srate data are normalized at 1.0/min by averaging the response. However, it is noted that %CS is a significant term for strain recovery but not for the others. Therefore, the empirical analysis of strain recovery involves three variables, whereas the others involve only the mixing ratio of the constituents. The coefficient terms are solved using the regression analysis in MATLAB by

**Table 5.2** Summary of main effects and interactions

| Properties | Significant terms | $R^2$ |
|---|---|---|
| Density | $\mathrm{G}, \mathrm{S}, \mathrm{G}^2, \mathrm{S}^2$ | 0.9519 |
| Strain recovery | $\mathrm{G}, \mathrm{S}, \mathrm{C}, \mathrm{S}^2, \mathrm{C}^2, (\mathrm{G} * \mathrm{S})$ | 0.8385 |
| Compressive modulus | $\mathrm{G}, \mathrm{S}, \mathrm{G}^2, \mathrm{S}^2$ | 0.9815 |
| Compressive strength | $\mathrm{G}, \mathrm{S}, \mathrm{G}^2, \mathrm{S}^2$ | 0.9804 |

*G* Gelatin, *S* SDS, *C* % compressive strain

tabulating the variables. Six empirical models derived from Eq. (5.4) were developed to capture the trend lines observed in the experimental data minus the redundant data.

Figure 5.8 shows the comparison of the experimental and empirical data for both, the low (LC) and the high (HC) compressive strains. In Fig. 5.8a, the upper and lower bounds of strain recovery are within 15 % range for both, the experiment and empirical data when the compressive strain is less than 20 %. In Fig. 5.8b, the empirical and experimental data for HC strains show good correlation as well for composites subjected to compressive strain between 20 and 50 %. More significantly, the charts show the effects of SDS at HC strain to be remarkable on strain recovery as compared to LC strain. Without SDS, the lower bound line (at 0 %SDS) is influence by the mass fraction of gelatin where strain recovery is possible only after addition of more than 14 % gelatin experimentally. Empirically, the model shows low recovery at low mass fraction of gelatin. This is because the model is based on stepwise regressive line that interpolates between data points and thus showing only one zero value.

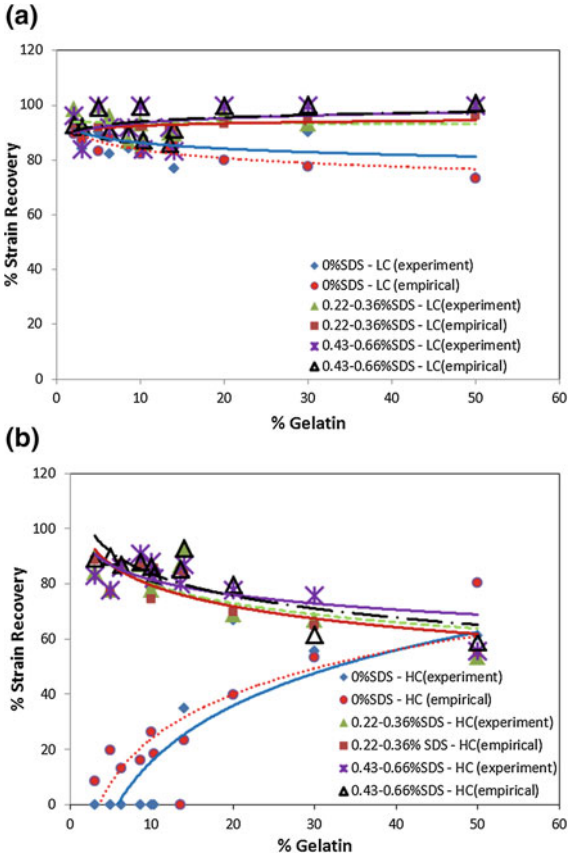


**Fig. 5.8** Empirical and experimental data and trend lines for **a** low compressive (LC: <20 %) strain and **b** high compressive (:20 % < HC < 50 %) strain: (*thick lines* show experiment trend-line while *dotted and dashed* lines indicate empirical trend-line)

However, with the addition of SDS, strain recovery is almost 80–90 % at low mass fraction of gelatin (<14 %). The upper bound lines for both empirical and experiment data are closely packed and there is little difference between them. Thus, the empirical model trend-line correlates well with the experimental data providing reasonable estimation of strain recovery for gelatin content of 2–50 % and SDS content between 0 and 0.66 %.

#### 5.3.3.2 General Trend of Density

The addition of SDS into the solution of gelatin increases the foaming capacity significantly as seen in Fig. 5.9b. As a result, the volume of the foamed solution increases thus reducing the density of the composite when compared with those without SDS additive. The density factor ($D_i$) is expressed as shown in Eq. (5.5).

$$D_i = \frac{\rho_i}{\rho_o} = C_i \ln A_i + B_i \tag{5.5}$$

where $\rho_i$ = Density of GSA − SDS, and $\rho_o$ = Density of GSA

$D_i$ is greatly influenced by the %SDS added to the solution. The box plot in Fig. 5.9 shows the median values of $D_i$ as a function of %SDS ($A_i$) after removing the single point observations and the outliers. In the experiments, the maximum amount of SDS used is 0.66 %. Ideally, the $D_i$ should not exceed the limiting value of 1. With this boundary condition, a natural logarithm function will be ideal to

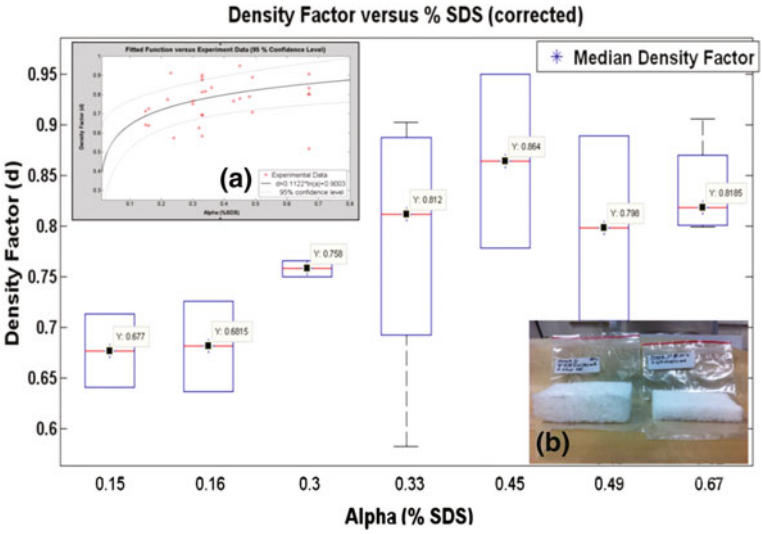


**Fig. 5.9** Median density factor, *inserts* **a** 95 % confidence of experimental data with fitted curve **b** reduced density due to SDS addition

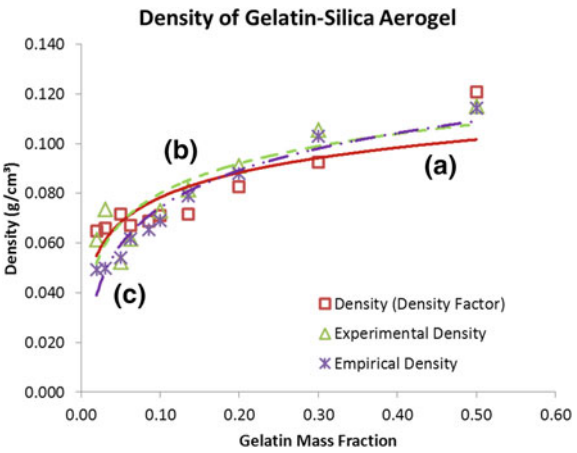


**Fig. 5.10** Comparison of density—**a** density factor analysis; **b** experimental data and **c** empirical model

express $D_i$ in terms of α as follows, where $C_i$ and $B_i$ are SDS concentration coefficient and the density factor limiting constant, respectively.

Median points are curve fitted to establish $D_i$ as a function of $A_i$ as shown in Fig. 5.4. The data points are within 95 % confidence interval which shows that the equation is a good fit; the $R^2$ is approximately 0.79. The $D_i$ in Fig. 5.9a approaches the limiting value of 1 with increasing %SDS. The established equation for the fitted curve is shown in Eq. (5.6).

$$D_i = 0.1122 \ln A_i + 0.9003 \tag{5.6}$$

The empirical model illustrated in Table 5.2 for density is compared with the experimental data and the density factor model derived previously as shown in Fig. 5.10. The trend lines between the experimental data and empirical model show very good correlation whereas the density factor analysis tend to underestimate the values. The density empirical model gives reasonable estimation of the composites density in terms of the amount of constituent material for both the gelatin and SDS in the ranges between 0 and 50 % for gelatin and 0–0.66 % for SDS respectively. Similarly, the models developed for compressive strength and modulus also showed close proximity between the experimental and empirical values of as shown in Figs. 5.11 and 5.12, respectively. Thus, it can be concluded that the empirical models developed via ANOVA in terms of process variables offer close estimation of the GSA and GSA–SDS composites experimental values.

### *5.3.4 Strain Recovery Optimization via Empirical Models*

Since the interest is on strain recovery of the composite at high compressive strain, the empirical models to validate the effect of SDS are plotted as shown in Fig. 5.13 at

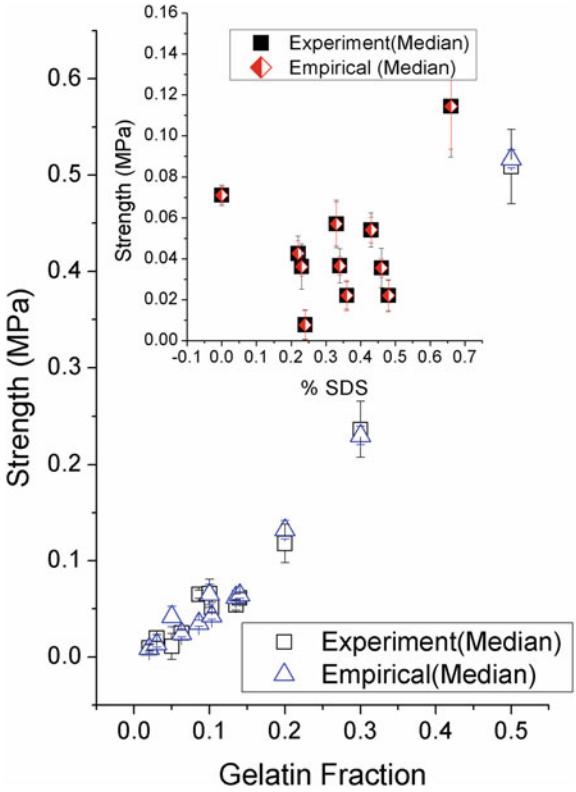


**Fig. 5.11** Empirical and experimental data for compressive strength as function of gelatin mass fraction %SDS (*insert*)

compressive strain of 45 % using empirical models and the coefficients derived from the experimental data. The maximum strain recovery of 86 % is achieved with a composite of 50 wt% gelatin and 0.41 wt% SDS. The optimal strain recovery of 0.74 is achieved for all the five variations of gelatin content when SDS is at 0.56 wt%. The optimal behavior of strain recovery with respect to compressive strength and modulus as a function of density was plotted in Fig. 5.14. Here the empirical models were plotted with increasing content of gelatin from 2 to 50 wt% which is reflected as the increase in the overall GSA–SDS composites' density at 0.56 wt% SDS.

Both the compressive modulus and strength show similar behavior. The GSA–SDS composites eventually reach the modulus and strength that is comparable to the brittle GSA composite and at the same time exhibiting significant strain recovery. The optimal combination for 0.56 wt%. SDS is when gelatin is approximately 45 % with strain recovery of 0.72, strength of 0.42 MPa, and modulus of 3.2 MPa with the density of 0.107 g/cm$^3$. The observation reveals a power law dependence of the mechanical properties on density. It is evaluated that an exponent of 2.87–3.27 for modulus and 3.16–4.00 for strength, respectively. The evaluated values incidentally agree well with the works of Woignier et al. (1989)

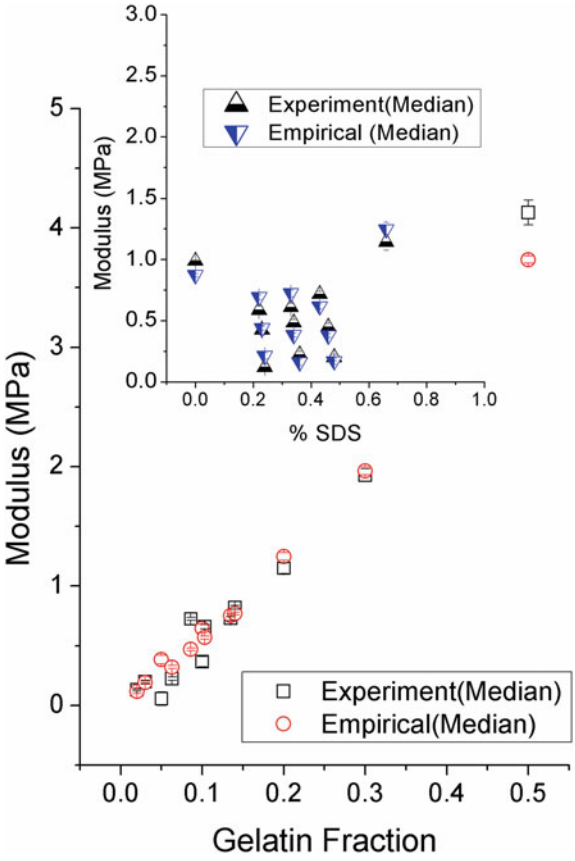


**Fig. 5.12** Empirical and experimental data for compressive modulus as function of gelatin mass fraction and %SDS (*insert*)

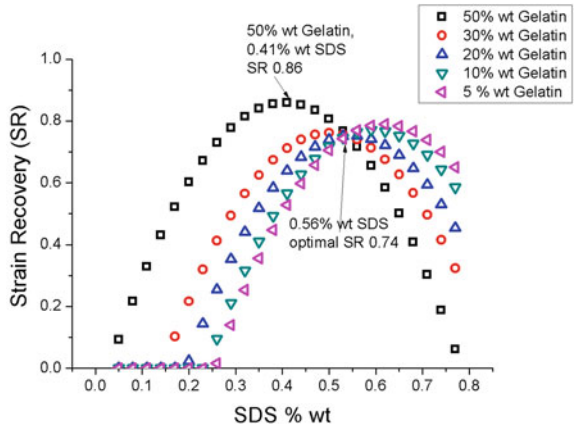


**Fig. 5.13** Graphs showing empirical %SR with increasing SDS wt% @ 45 % CS

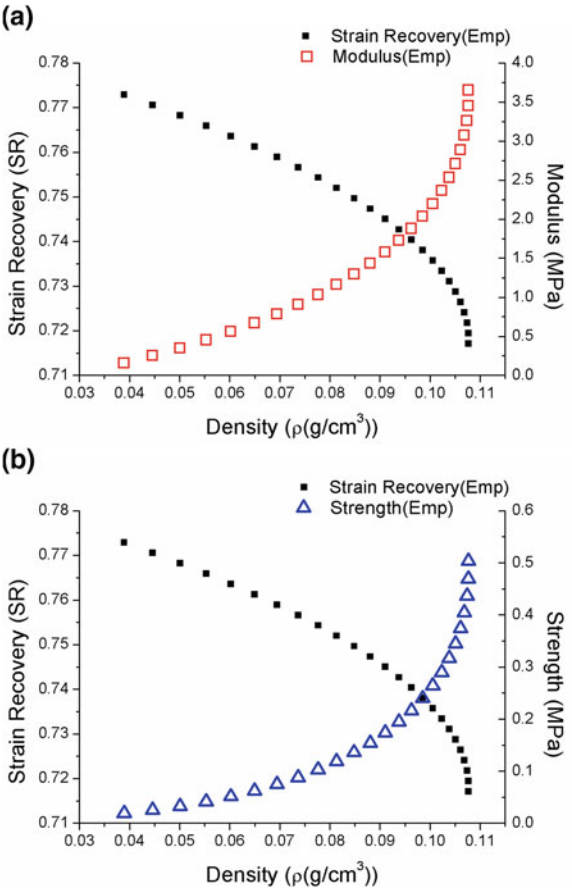


**Fig. 5.14** Optimal empirical illustration of **a** compressive modulus and SR versus density and **b** compressive strength and SR versus density @ 0.56 wt% SDS

who concluded that the process parameters, such as concentration of silicon compounds, catalytic conditions, and the preparation conditions affect an aerogel prepared via sol gel technique. The modulus of the aerogel obeys the power law dependence relative to its density with the exponent of 3.7.

## 5.4 Validation of Optimal Properties with GSA–SDS Composites

The optimized empirical model is validated with two sets of five sample blocks of 10–50 wt% gelatin mass fraction (four specimens from each block) with 0.56 wt% SDS loaded to 45 % compressive strain prepared via FM method and FD method respectively. The results are then compared with the optimized empirical model for consistency as shown in Fig. 5.15. The trends of the experimental results although

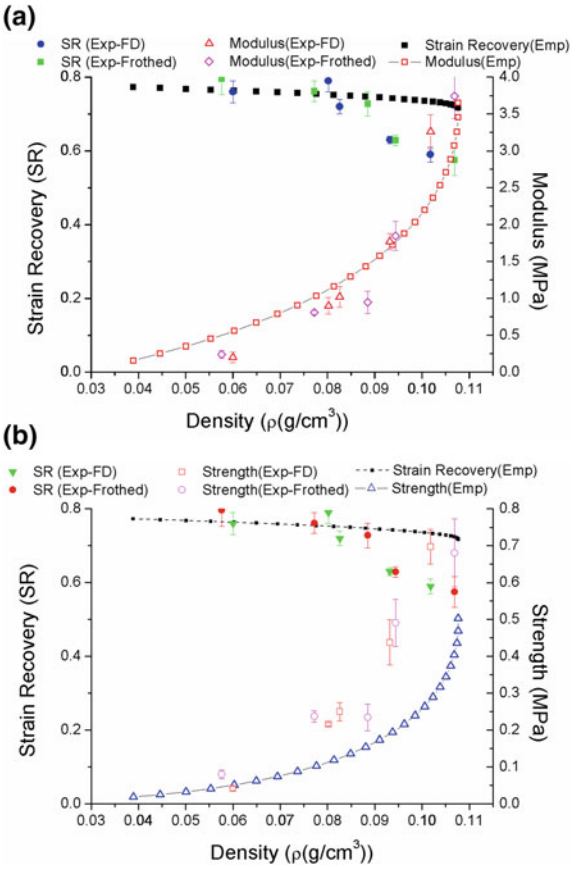


**Fig. 5.15** Comparison of validated optimal properties with FM and FD specimens **a** compressive modulus and SR versus density and **b** compressive strength and SR versus density

follow the general curve of the empirical model, they do not reflect as accurately as initially postulated. There could be several possible reasons for such an outcome.

First, the modulus is taken the steepest slope at as the function of time which usually occurs during the initial loading and it is different from the points for strength. Thus the compressive modulus seems to be inclined towards the empirical model. Second, the strength is taken as the maximum strength recorded when the specimens are unloaded, which explains why the strength is higher than the conservative empirical model. In addition, the maximum strength for the same composition varies due to irregular shapes of the aerogels that affect their binding efficiency. The irregular arrangement within the specimen could also attribute to the lower strain recovery recorded at higher density although the strain recovery was accurate up to 30 % gelatin mass fraction.

Lastly, the contribution of 'air pockets' or the lack of it could be another factor. The reduction of strain recovery corresponds to higher strength suggesting that there may be lesser 'air pockets' in the FD specimens. The specimens fabricated by FM method and FD method showed little visual difference in terms of trend but the

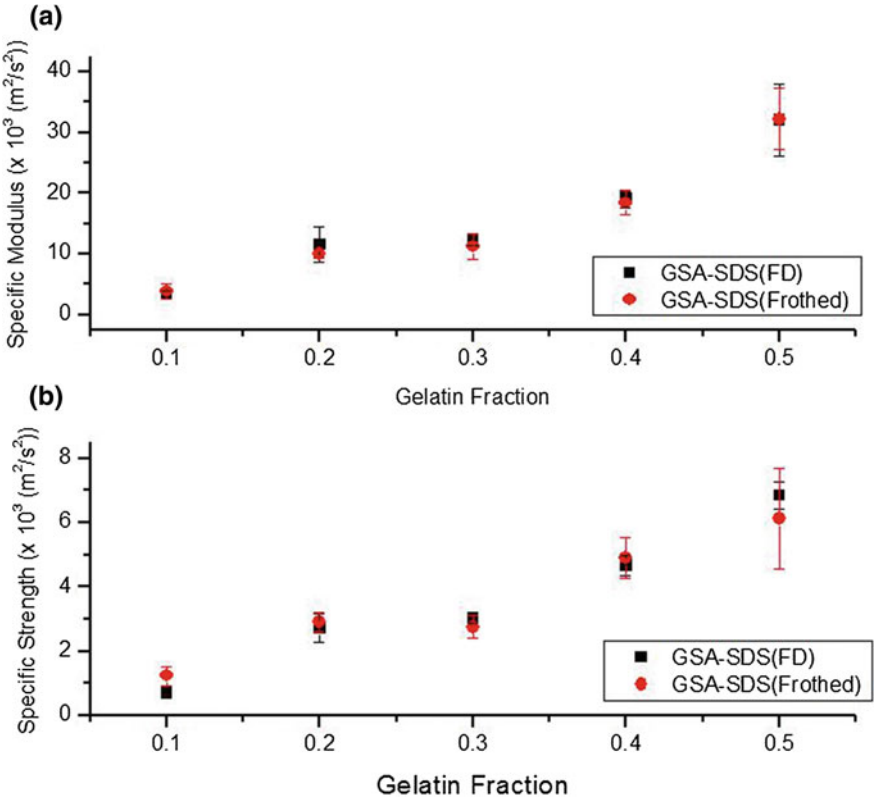


**Fig. 5.16** Comparison of validated properties of FM and FD specimens **a** specific modulus versus gelatin and **b** specific strength versus gelatin

FD specimens are observed to have slightly higher specific strength and specific modulus as compared to FM specimens as seen from Fig. 5.16. The modulus trend of the FD specimens also seems to follow the empirical model relatively better than FM specimens. The strain recovery for the FD specimens is marginally higher than the FM specimens as shown in Fig. 5.15.

### *5.4.1 Influence of Silica Aerogel Granules on Mechanical Properties of GSA–SDS Composites*

The influence of silica aerogel granule sizes is studied to analyze the above postulations further. The optimal conditions discussed thus far (i.e., 0.56 wt% SDS) are again used in the fabrication of the composites. Two configurations, one with 20 wt% gelatin and another with 40 wt% gelatin with four silica aerogel granules sizes are

studied. Table 5.3 shows the summary of the results for density, strain recovery, compressive strength and modulus obtain from the study.

The density of the composites for the various granule sizes showed good consistency between 0.067 and 0.084 g/cm$^3$. The increase in gelatin content although doubled, but the density is lesser than the GSA–SDS composite blocks tested with mixed granules in the previous sections indicating that they are much lighter. It is expected that isolating the granules by their sizes would affect the compactness and therefore one would expect marginal decrease in density.

Figure 5.17a–c shows the influence of silica aerogel granules on the strain recovery, compressive strength and compressive modulus as compared to the validated results for 20 and 40 wt% results extracted from the Fig. 5.16. The strain recovery is greater when the composites are fabricated according to the silica aerogel granule size but the compressive strength and modulus is much lesser than the mean values of the mixed granules. A few conclusions can be drawn from reduced density, strength and modulus accompanied by increase in strain recovery when the composites are isolated according to the granule sizes.

The mixed granules fabricated in the previous sections are made up of granule sizes from 0.1 to 4.0 mm consisting of irregular shapes. It was noted in the previous section that the irregular arrangement led to lower strain recovery. However, isolating the granules according to the sizes actually increased the strain recovery. This concludes that when the sizes of the granules are uniform, there will be an increase in strain recovery. On the contrary, the irregularly shaped granule sizes have higher strength and modulus than those shown in Fig. 5.17b, c. The irregularly shaped granules provided increased resistance as smaller granules sits in between the larger granules. The phenomenon is analogous to alloys where elemental particles occupy the space between the larger particles of another element preventing slippage of interstitial bonds between planes. Thus, the GSA–SDS composites with uniform granule sizes on the whole have lower strength and modulus with increased strain recovery than the mixed granules.

**Table 5.3** Summary of density, strain recovery, compressive strength, and modulus of GSA–SDS composites in terms of aerogel granule sizes under optimal conditions

| | Granule size (mm) | Density $\rho$ (g/cm$^3$) | Strain recovery | Compressive strength (MPa) | Compressive modulus (MPa) |
|---|---|---|---|---|---|
| GSA–SDS (20/80/0.56) | 1.2 | 0.067 ± 0.01 | 0.786 ± 0.04 | 0.120 ± 0.02 | 0.434 ± 0.05 |
| | 1.7 | 0.070 ± 0.01 | 0.759 ± 0.05 | 0.121 ± 0.03 | 0.409 ± 0.05 |
| | 2.18 | 0.068 ± 0.01 | 0.830 ± 0.04 | 0.105 ± 0.03 | 0.328 ± 0.05 |
| | 2.58 | 0.068 ± 0.01 | 0.749 ± 0.05 | 0.142 ± 0.02 | 0.347 ± 0.04 |
| GSA–SDS (40/60/0.56) | 1.2 | 0.081 ± 0.01 | 0.647 ± 0.04 | 0.286 ± 0.02 | 1.527 ± 0.09 |
| | 1.7 | 0.075 ± 0.01 | 0.697 ± 0.06 | 0.266 ± 0.04 | 0.994 ± 0.06 |
| | 2.18 | 0.079 ± 0.01 | 0.772 ± 0.06 | 0.223 ± 0.03 | 0.874 ± 0.10 |
| | 2.58 | 0.084 ± 0.01 | 0.680 ± 0.04 | 0.303 ± 0.03 | 1.301 ± 0.14 |

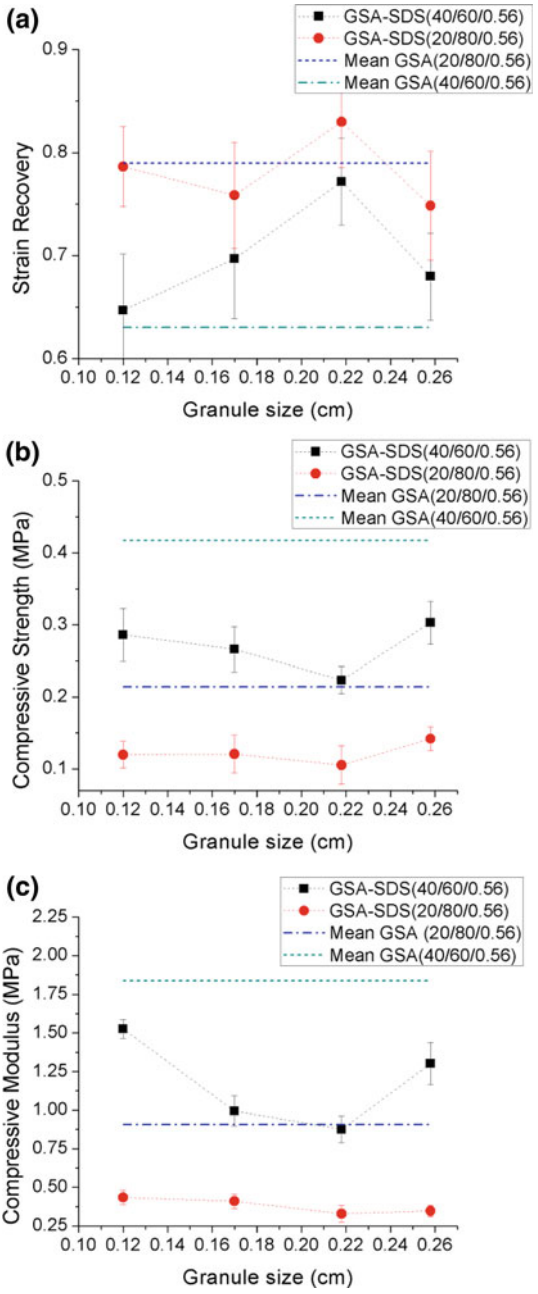


**Fig. 5.17** Influence of silica aerogel granule size on **a** strain recovery; **b** compressive strength and **c** compressive modulus

However, it is observed that the smaller the granule size the higher the strength and modulus. Interestingly, the maximum strain recovery recorded for 2.18 mm silica aerogel granule size also showed the minimum strength and modulus.

The strength and modulus decreased from 1.2 to 2.18 mm and reversed when the size is 2.58 mm. For the same mass of silica aerogel granules, the smaller granules have larger number of granules and as well as greater exposed surface area that binds with the gelatin.

This results in greater resistance collectively when subjected to compression load which leads to higher strength and modulus experienced by the smaller granules. But 2.58 mm silica aerogel granules show the highest strength and modulus. It can therefore be concluded that the granules of 2.18 mm size offer the least resistance, thus, experiencing the highest strain recovery but least strength and modulus. An increase in the granule size means a lesser number of granules for the same mass with increased amount of gelatin network around the granules. Possibly, this increase in strength and modulus from 2.18 to 2.58 mm is influenced by the strength of the gelatin network around the granules rather than the granules themselves. The gaps between the 2.58 mm granules are larger which lead to weakened gelatin structure after compression resulting in the lowest strain recovery for the four silica aerogel granule sizes.

The influence of silica aerogel granules has further enhanced the understanding of the mechanism behind the strain recovery. If strain recovery is the objective, then the composites with regularly shaped granules will give the best results, especially 2.18 mm granule size albeit the lowest strength and modulus. If the objective is strength and modulus, then the composite with mixed granules will give the best results with reasonable strain recovery.

## 5.5 FMWNT-Doped GSA and GSA–SDS Composites (FM)

GSA-CNT and GSA–SDS/FMWNT composite blocks are fabricated in the same manner using the FM method as previously described in Chap. 3 with an addition 0.042 and 0.084 wt% of MWNT-COOH (FMWNT) into an aqueous gelatin solution. A total of 24 composite blocks comprising 144 specimens are tested for the same properties as previously described using the same experimental techniques but for only high compressive strains at 33.3 and 44.4 % since the interest is on the response of the composites under high compressive strain with the addition of very insignificant amounts (max. 0.084 wt%) of FMWNT.

### *5.5.1 Influence of FMWNT on Composites*

The general empirical model from Eq. (5.4) has been modified to include the constituents of FMWNTs and to exclude the strain rate as shown in Eq. (5.7).

**Table 5.4** ANOVA-evaluated significant process variable with the addition of FMWNT on GSA and GSA–SDS composites

| Properties | Significant terms |
|---|---|
| Density | $G, S, G^2, S^2$ |
| Strain recovery | $G, S, Cn, C, G^2$ |
| Compressive modulus | $G, S, Cn, G^2, S^2,$ |
| Compressive strength | $G, Cn, G^2$ |

*G* gelatin, *S SDS*, *C* % compressive strain and *Cn FMWNT*

$$\begin{aligned} Y = {} & \beta_0 + \beta_1 G + \beta_2 S + \beta_3 Cn + \beta_4 C + \mu_1 G^2 + \mu_2 S^2 + \mu_3 Cn^2 + \gamma_1 (G * S) \\ & + \gamma_2 (G * Cn) + \gamma_3 (G * C) + \gamma_4 (S * Cn) + \gamma_5 (S * C) + \gamma_6 (C * Cn) \\ & + \emptyset_1 (S * Cn * G) + \emptyset_2 (S * C * G) + \emptyset_3 (C * Cn * G) \\ & + \emptyset_4 (S * Cn * C) + \emptyset_5 (S * Cn * G * C) \end{aligned} \tag{5.7}$$

where $Y$ = response of the property, $G$ = gelatin, $S$ = SDS, Cn = FMWNT, $C$ = compressive strain on the specimen, and, $(\beta, \mu, \gamma, \emptyset)$ = coefficients of main effects and interactions.

From Table 5.4, the addition of FMWNTs has significant terms in all the properties except for density. The empirical models based on significant terms have been derived for each of the property based on the experimental data and the terms in Table 5.4. The new empirical models with the addition of FMWNTs will be compared with the ones developed in the earlier part of this chapter to evaluate the effects of the FMWNTs on the composite.

### 5.5.2 *Experimental Result—General Trend of Stress–Strain Curves*

Figure 5.18 shows the stress–strain curve of the composites in the following nomenclature; (1) GSA (2) GSA–SDS (3) GSA-FMWNT (4) GSA–SDS/FMWNT. The stress–strain curves of GSA and GSA-FMWNT show marginal increase in strength with addition of FMWNT. On the other hand, the strength with FMWNT addition is significantly lower with SDS while developing longer stress plateau as compared with GSA–SDS composites.

The general trends of strain recovery with additions of FMWNT are shown in Fig. 5.19. The black hollow markers are the data abstracted GSA and GSA–SDS composites. The red markers are composites with 0.042 wt% FMWNT and the green markers are those with 0.084 wt% FMWNT. As with SDS, the addition of FMWNTs generally increases the strain recovery as seen by the converging envelops of green- and red-hatched lines over the black ones. In fact, the lines converge higher and at reduced content of gelatin to approximately 8–10 % as compared with GSA and GSA–SDS composites.

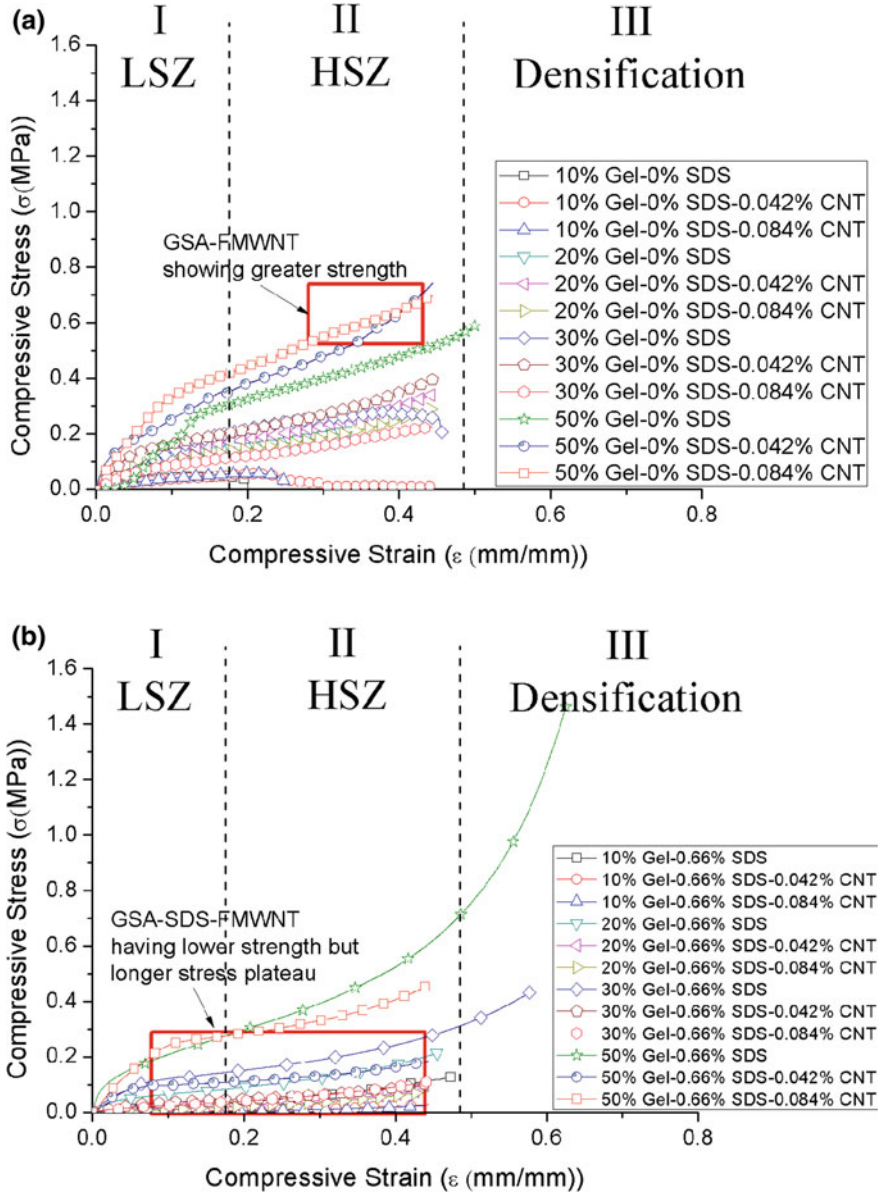


**Fig. 5.18** Addition of FMWNTs doped in composites showing **a** increased strength over GSA composites **b** increased compressibility over GSA–SDS composites

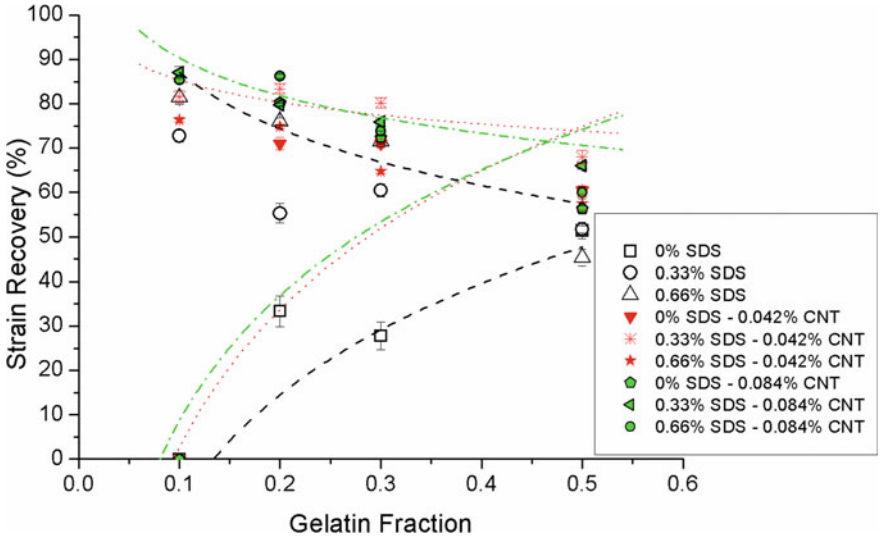


**Fig. 5.19** Comparison of experimental strain recovery trends with addition of FMWNT

### *5.5.3 Empirical Analysis of Various Properties*

The coefficient constants of the empirical models are resolved using the regression analysis in MATLAB from the experimental data. The addition of FMWNTs did not significantly affect the density as seen from ANOVA and thus the empirical model remains the same.

#### 5.5.3.1 Strain Recovery

Although quadratics terms for SDS and FMWNT are initially included in the regression analysis, the terms are deemed too small (order of −14), and are removed when solving the coefficient. Thus, only the linear terms are included in the model. The empirical models for GSA-FMWNT and GSA–SDS/FMWNT are derived based on experimental data. For GSA and GSA–SDS, the previously derived equations are maintained. In Fig. 5.20, the empirical models and the experimental data correlated well as seen from the cluttering of the trend lines.

Empirically, the maximum strain recovery is at 90.4 % while the experimental data shows 92.4 %. Comparing with Fig. 5.9, there is an increase in strain recovery at higher gelatin and convergence occurring at approximately 35–37 % gelatin content. Even though the GSA–SDS/FMWNT composites exhibit higher strain recovery in terms of percentage, in absolute terms, it is actually 1.05 mm lesser than GSA–SDS composite as seen from Table 5.5. Thus, SDS remains the main component for strain recovery exhibited in all the composites regardless the composition of FMWNTs present.

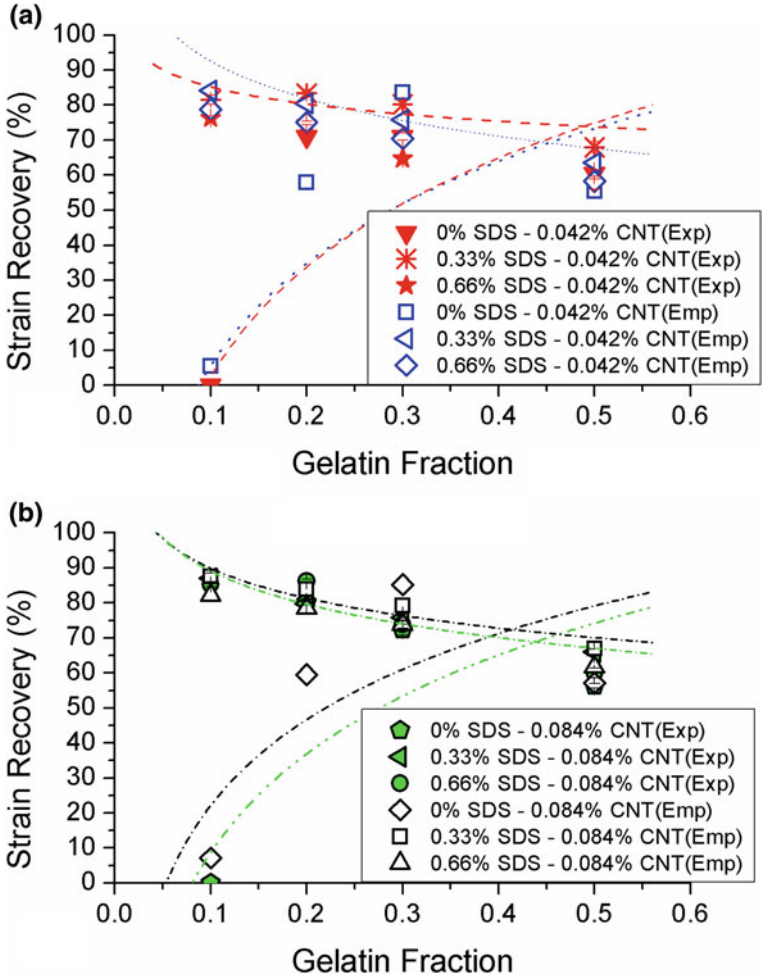


**Fig. 5.20** Empirical and experimental data and trend lines for **a** 0.042 wt% FMWNT and **b** 0.084 wt% FMWNT

**Table 5.5** Comparison of absolute and percentage values of strain recovery

| Recovery | mm | Change | Recovery | % | Change |
|---|---|---|---|---|---|
| GSA | 2.69 | | GSA | 28.13 | |
| GSA–SDS | 6.65 | 3.96 | GSA–SDS | 64.22 | 36.09 |
| GSA-CNT | 3.60 | 0.92 | GSA-CNT | 51.19 | 23.07 |
| GSA–SDS/CNT | 5.60 | 2.91 | GSA–SDS/CNT | 74.81 | 46.68 |

### 5.5.3.2 Compressive Strength and Modulus

Figure 5.21 shows the compressive strength and modulus of the composites with FMWNTs compared with GSA–SDS. It also shows the relative proximity of the experimental data with the empirical model. Generally, GSA–SDS/FMWNT composites yield a lower modulus and strength than those without it. The empirical

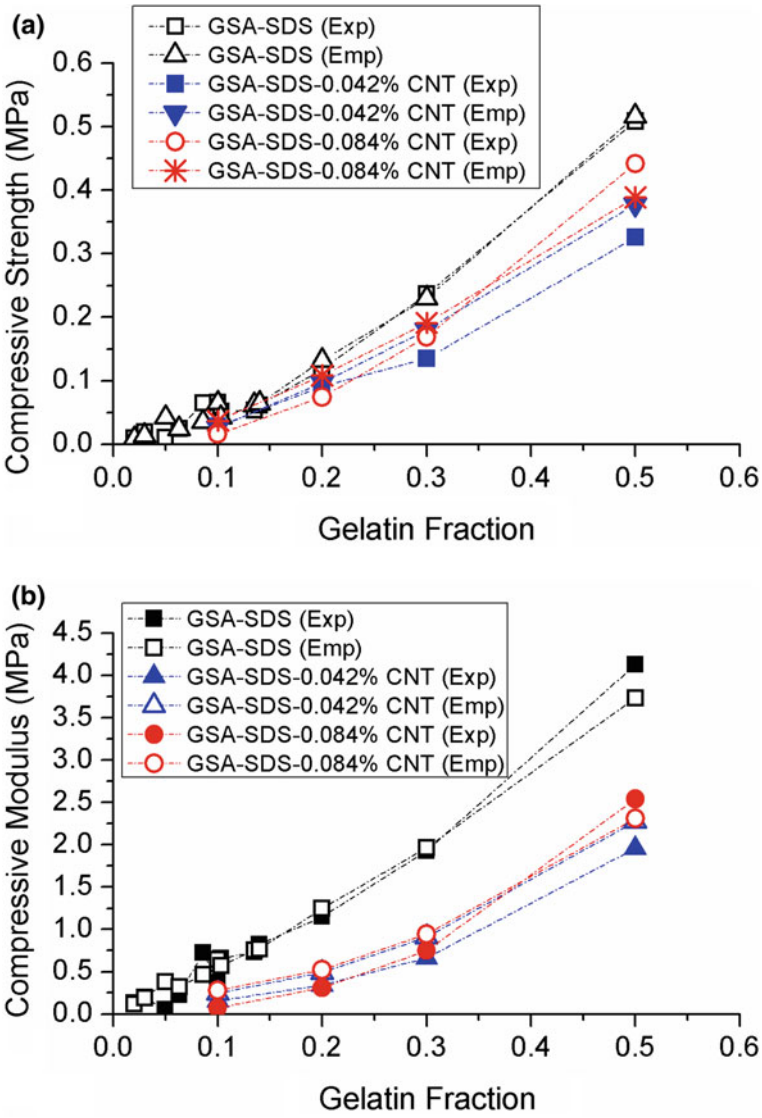


**Fig. 5.21** Empirical and experimental data and trend lines for **a** compressive modulus and **b** compressive strength

model showed good fit with the experimental data in the range $R^2 = 0.89–0.96$. The FMWNTs used in the experiment are functionalized with COOH, and thus in a given volume of water, the dissociation into $H^+$ ions becomes limited with gelatin. Gelatin draws its strength through its viscosity and ability to swell. The swelling of gelatin is observed to be hindered by the addition of FMWNTs with reduction in the viscosity. Thus, FMWNTs being nano-sized attach themselves to the end group of gelatin chain preventing them from creating intramolecular bonding and at the same time occupy the spaces between water molecules. By doing so, the chains strength is affected resulting in the lower strength and modulus.

## 5.6 Concluding Remarks

The two fabrication methodologies, via FM method and FD method, are deployed in making GSA composites of various amounts of gelatin and SDS content. The results are presented and the effects of SDS and FMWNT on density, strength, and modulus are discussed. Most significantly, composites with SDS have shown the ability to recover after strain loadings. GSA–SDS composites have strain recovery between 80–95 % in LSZ and 70–90 % in HSZ exhibiting ductile behavior. The transition from brittle to ductile behavior is explained via schematic diagrams that are analogous to creep-like response of polymeric materials. The contribution of 'air pockets' induced during the frothing of gelatin solution with SDS have been accorded as the reason for the GSA–SDS composites to have high strain recovery even under high compressive strain of up to 45 %. This phenomenon is unusual for the brittle silica aerogel granules and dried gelatin.

Empirical models developed via ANOVA proved to be consistent with the experimental data and it was determined that by adding 0.56 wt% SDS into the composite mix would result in optimization of strain recovery (in the range 70–80 %). Validation on the optimized set of parameters is carried experimentally with both the FM and the FD specimens. The validated data show slight difference from the empirical estimation but the FD specimens show better strength-to-weight and modulus-to-weight ratios. The overall quality of the fabricated FD specimens is better since the air pockets between the particles are reduced thus facilitating better physical adhesion. The influence of silica aerogel granules using the optimized configuration is studied. It is concluded that the irregularly shaped granules contribute to higher strength and modulus as compared to the regularly shaped granules. However, the regularly shaped granules increase the strain recovery than the mixed granules.

The influence of FMWNTs on the mechanical properties are investigated and reported. While it is thought that the FMWNTs, which supposedly having high strength and modulus (Jie 2004) will reinforce to the strength and modulus of GSA–SDS composites; experiments carried out showed otherwise. FMWNTs have lowered the strength and modulus especially when compared with the GSA–SDS composites.

# Appendix 5A—Failed Specimen Analysis (FM Method)

| Gelatin (%) | SDS(%) | Compression (%) | Strain Recovery (%) |
|---|---|---|---|
| 2 | 0 | 17 | 0 |
| 2 | 0 | 21 | 0 |
| 2 | 0.24 | 21 | 0 |
| 2 | 0.36 | 21 | 0 |
| 2 | 0.48 | 21 | 0 |
| 3 | 0 | 21 | 0 |
| 5 | 0 | 24 | 0 |
| 5 | 0 | 33.3 | 0 |
| 5 | 0 | 44.4 | 0 |
| 6.3 | 0 | 21 | 0 |
| 8.6 | 0 | 21 | 0 |
| 10 | 0 | 24 | 0 |
| 10 | 0 | 33.3 | 0 |
| 10 | 0 | 44.4 | 0 |
| 10.3 | 0 | 21 | 0 |
| 20 | 0 | 44.4 | 0 |
| 30 | 0 | 44.4 | 0 |

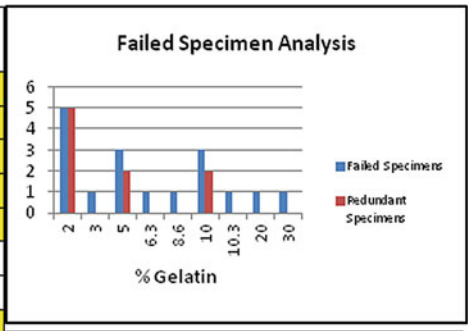


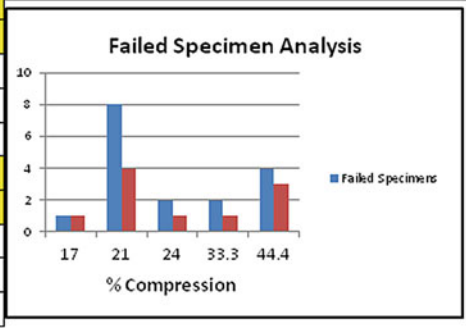


## References

Alaoui, A.H., T. Woignier, G.W. Scherer, and J. Phalippou. 2008. Comparison between flexural and uniaxial compression tests to measure the elastic modulus of silica aerogel. *Journal of Non-Crystalline Solids* 354(40–41): 4556–4561.

Alavi Nikje, M.M., M. Khanmohammadi, A.B. Garmarudi, and K. Ghasemi. 2009. Analysis of variance (ANOVA) for optimizing the nano-$SiO_2$ content of high performance epoxy nanocomposites. *Journal of Macromolecular Science Pure and Applied Chemistry* 46(1): 116–120.

Ashby, M.F., and L.J. Gibson. 1997. *Cellular solids—structure and properties.* Cambridge: Cambridge University Press.

Besseris, G.J. 2008. Analysis of an unreplicated fractional-factorial design using nonparametric tests. *Quality Engineering* 20(1): 96–112.

Emmerling, A., and J. Fricke. 1997. Scaling properties and structure of aerogels. *Journal of Sol-Gel Science and Technology* 8(1): 781–788.

Groβ, J., and J. Fricke. 1995. Scaling of elastic properties in highly porous nanostructured aerogels. *Nanostructured Materials* 6(5–8): 905–908.

Jie, H. 2004. *Structures and properties of carbon nanotubes*. *Carbon Nanotubes*. Boca Raton: CRC Press, 1–24.

Lu, G., G.Q. Lu, and Z.M. Xiao. 1999. Mechanical properties of porous materials. *Journal of Porous Materials* 6(4): 359–368.

Ma, H.-S., A.P. Roberts, J.-H. Prévost, R. Jullien, and G.W. Scherer. 2000. Mechanical structure–property relationship of aerogels. *Journal of Non-Crystalline Solids* 277(2–3): 127–141.

Ma, H.-S., J.-H. Prévost, R. Jullien, and G.W. Scherer. 2001. Computer simulation of mechanical structure–property relationship of aerogels. *Journal of Non-Crystalline Solids* 285(1–3): 216–221.

Meador, M.A.B., A.S. Weber, A. Hindi, M. Naumenko, L. McCorkle, D. Quade, S.L. Vivod, G.L. Gould, S. White, and K. Deshpande. 2009. Structure–property relationships in porous 3D nanostructures: epoxy-cross-linked silica aerogels produced using ethanol as the solvent. *ACS Applied Materials and Interfaces* 1(4): 894–906.

Mills, N.J., and H.X. Zhu. 1999. The high strain compression of closed-cell polymer foams. *Journal of the Mechanics and Physics of Solids* 47(3): 669–695.

Moner-Girona, M., A. Roig, E. Molins, E. Martinez, and J. Esteve. 1999. Micromechanical properties of silica aerogels. *Applied Physics Letters* 75(5): 653–655.

Montgomery, D.C. 2013. *Design and analysis of experiments [electronic resource]*, 8th edition. Hoboken, NJ: John Wiley & Sons, Inc.

Nguyen, B.N., M.A.B. Meador, M.E. Tousley, B. Shonkwiler, L. McCorkle, D.A. Scheiman, and A. Palczer. 2009. Tailoring elastic properties of silica aerogels cross-linked with polystyrene. *ACS Applied Materials and Interfaces* 1(3): 621–630.

Obrey, K.A.D., K.V. Wilson, and D.A. Loy. 2011. Enhancing mechanical properties of silica aerogels. *Journal of Non-Crystalline Solids* 357(19–20): 3435–3441.

Parmenter, K.E., and F. Milstein. 1998. Mechanical properties of silica aerogels. *Journal of Non-Crystalline Solids* 223(3): 179–189.

Roberts, A.P., and E.J. Garboczi. 2001. Elastic moduli of model random three-dimensional closed-cell cellular solids. *Acta Materialia* 49(2): 189–197.

Roberts, A.P., and E.J. Garboczi. 2002. Elastic properties of model random three-dimensional open-cell solids. *Journal of the Mechanics and Physics of Solids* 50(1): 33–55.

Scherer, G.W., D.M. Smith, X. Qiu, and J.M. Anderson. 1995a. Compression of aerogels. *Journal of Non-Crystalline Solids* 186: 316–320.

Scherer, G.W., D.M. Smith, and D. Stein. 1995b. Deformation of aerogels during characterization. *Journal of Non-Crystalline Solids* 186: 309–315.

Sudharsan, N.M., and E.Y.K. Ng. 2000. Parametric optimization for tumour identification bioheat equation using ANOVA and the Taguchi method. *Proceedings of the Institution of Mechanical Engineers Part H-Journal of Engineering in Medicine* 214(H5): 505–512.

Woignier, T., J. Phalippou, and R. Vacher. 1989. Parameters affecting elastic properties of silica aerogels. *Journal of Materials Research* 4(03): 688–692.

Woignier, T., J. Reynes, A. Hafidi Alaoui, I. Beurroies, and J. Phalippou. 1998. Different kinds of structure in aerogels: relationships with the mechanical properties. *Journal of Non-Crystalline Solids* 241(1): 45–52.

Zhu, H.X., J.F. Knott, and N.J. Mills. 1997a. Analysis of the elastic properties of open-cell foams with tetrakaidecahedral cells. *Journal of the Mechanics and Physics of Solids* 45(3): 319–343.

Zhu, H.X., N.J. Mills, and J.F. Knott. 1997b. Analysis of the high strain compression of open-cell foams. *Journal of the Mechanics and Physics of Solids* 45(11–12): 1875–1904.

# Chapter 6
# Superhydrophobic and Ultralow Thermal Insulation

## 6.1 Introduction

Silica aerogels are very light, highly porous nanomaterial with large internal surface area possessing excellent thermal insulation that may get affected when the binders and additives used in aggregation. The most significant of all the properties is the extremely low thermal conductivity, reportedly to be in the range 0.017–0.024 W/m-K as highlighted by Schmidt and Schwertfeger (1998).

Thermal conductivity, $\lambda$, is the property of a material to conduct heat that is primarily governed by the Fourier's Law of heat conduction. Silica aerogel has unique properties resulting from the sol–gel method that produce extremely low density transparent solids having small pore size that has extremely high thermal resistance. When evacuated under partial vacuum (0.1 bar), the effective thermal conductivity is reduced by a factor of three to about 0.007 W/m-K at 280 K (van Bommel et al. 1997). Reim et al. (Reim et al. 2004) studied the thermal and optical properties of the silica aerogel granules as compared to its monolith, noting the similarity in the reduction of gaseous conductivity at 0.1 bar. Reim et al. (Reim et al. 2005) studied the use of silica aerogel granules as an embedded material in a glazing element for optical and thermal properties achieving heat transfer coefficient of less than 0.4 W/($m^2$-K) and total solar energy transmittance of 35 %. Measuring the individual mode of thermal transport, that is, conduction, convection, and radiation can be difficult as each mode is interdependent on the other. Total thermal conductivity measurements are usually done to gage the thermal conductivity of the silica aerogels.

Researchers have different models and means of measuring the thermal conductivity, some of which are sandwiched panel design between two conductive plates (Hunt et al. 1991), guarded hot plate method (Ge et al. 2009), vibrational thermal relaxation technique developed by Bernasconi et al. (1992) and modified Tsao's model predictive theoretical technique (Cheng and Vachon 1969).



M. Sachithanadam and S.C. Joshi, *Silica Aerogel Composites*,
Engineering Materials, DOI 10.1007/978-981-10-0440-7_6

Commercially manufactured silica aerogels from Cabot Corp are mostly irregularly shaped granules. The various sizes and irregular shapes of the aerogel granules result in a heterogeneous distribution in a given sample. As a result, material properties such as density, strength, thermal conductivity, and acoustic absorptivity vary from one sample lot to another, thereby affecting experimental results. It is, therefore, necessary to evaluate the distribution of the granule sizes and its corresponding effects on the basic material properties and when used as a constituent material in a composite with other materials. The effects of silica aerogel granule size and mass ratio of FMWNT on the thermal conductivity are investigated.

### 6.1.1 Hydrophobicity

Silica aerogels can be either hydrophilic or hydrophobic. A material that resists water or insoluble in water is said to possess hydrophobic properties and vice versa for hydrophilic. Both characteristics of the aerogels depend vastly on the precursors, solvents, drying methods, and silylating agents used (Qin et al. 2013). Hydrophilic aerogels due to its water absorbing nature and subsequent collapse of its solid fractal component are rarely used, till recently with growing interest in drug delivery systems especially ketoprofen (Alnaief and Smirnova 2010) and griseofulvin (Smirnova et al. 2004). Thus, most of the aerogels in applications are hydrophobic. As mentioned previously, silica aerogels will lose its hydrophobic qualities at above 350 °C or after a prolonged period. This process of oxidation revert the aerogels back to its hydrophilic state. However, it can regain its hydrophobicity from reaction with gaseous methanol (Lee et al. 1995) and subsequently, the chemical bonds in the aerogels can be examined by Fourier Transform Infrared Spectroscopy (FTIR) or other means.

Hydrophobicity is measured through the contact angle $(\theta)$ of a water droplet on the aerogel surface as shown in Fig. 6.1. Contact angle, $\boldsymbol{\theta}$, is a quantitative measure of wetting of a solid by a liquid. It is defined geometrically as the angle formed by a

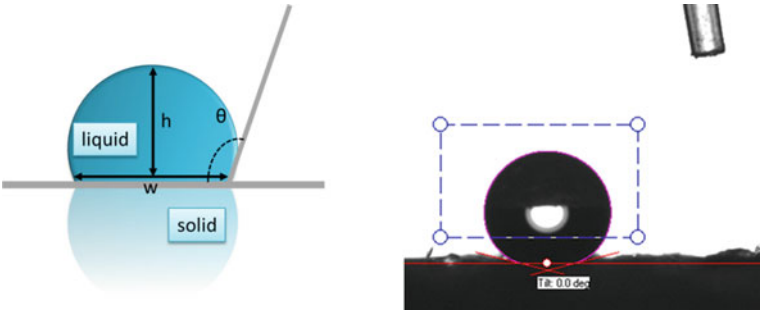


**Fig. 6.1** Contact angle measurements on silica aerogels using water drop test

liquid at the three-phase boundary where a liquid, gas, and solid intersect. The contact angle is calculated as in Eq. 6.1 where $\boldsymbol{h}$ is the height and $\boldsymbol{w}$ is the width of the water droplet (Rao et al. 2005).

$$\theta = 2\tan^{-1}\left(\frac{2h}{w}\right) \tag{6.1}$$

The liquid is known to have wet the surface when the contact angle is less than 90°; achieving complete wetting when the contact angle is zero (Scientific 2015). For contact angles greater than 90°, the surface is said to be non-wetting with that liquid. Generally, contact angle measurements that show more than 90° indicate that the material is hydrophobic. For superhydrophobic materials the contact angles are greater than 150° (Rao et al. 2005).

Contact angles can be divided into static and dynamic angles. Movement of the three-phase boundary determines the measurement of static or dynamic angles. Moving three-phase boundary measures the dynamic contact angles and static contact angles are measured when droplet is standing on the surface and the three-phase boundary is not moving (Scientific 2015). When the three-phase boundary is moving, dynamic contact angles are referred as advancing and receding angles (Chibowski 2007). In practice, a droplet is placed on the solid surface and the image of the drop is recorded as shown in Fig. 6.1. Static contact angle is then defined by fitting Young–Laplace equation around the droplet (Scientific 2015).

The thermal stability of aerogels in terms of hydrophobic degradation can be estimated by means of thermogravimetric and differential thermal analysis (TGA-DTA). Alternatively, silica aerogels can be heated in periodic intervals and then measure the contact angle $(\theta)$ to determine the hydrophobicity at elevated temperatures. This chapter discusses the variations in thermal conductivity of a binder-treated gelatin silica aerogel-sodium dodecyl sulfate (GSA–SDS) composite blocks doped with FMWNT prepared via FD and FM methods. The effects of FMWNT on the hydrophobicity measured via static contact angles are also studied. Thermal conductivity of GSA–SDS and GSA–SDS/FMWNT composites is evaluated with several mass ratios of the composite mix for 1-D steady-state heat transfer at mean temperature, $T_m$ (300–370 K), using Lee's Disc method. The experimental technique and the related calculations will be aerogel-sodium dodecyl sulfate. Thermal conductivity tests are carried out in an enclosed chamber under ambient conditions using Thermotron Model SE-300 as per ASTM C177-13. Acoustic properties are measured as per ASTM E1050 using B&K Type 4206 Impedance Tube. The aerogel granules distribution analyses are carried out using mechanical sieve shaker. The hydrophobic qualities of the specimens are evaluated by measuring the contact angles using Attension Theta Optical Tensiometer as per ASTM D-7334. The experimental technique and the related calculations will be described in the following sections.

## 6.2 Thermal Conductivity Measurements

The thermal conductivities of the composites and silica aerogel granules are evaluated using the Lee's Disc method as per ASTM C177-13 as shown in Fig. 6.2. It consists of three copper plates (CP) with the dimensions of 75 × 45 × 3 mm and a heater measuring 75 × 45 × 1 mm. The heater is connected to the constant power source at 5 levels of input: 1.18, 1.92, 3.16, 4.75, and 6.84 W. Thermal probes are placed on the top of the 1st CP, at the side of 2nd CP, at the side of the composite block, and at the bottom of the 3rd CP. The composite is sandwiched between the CPs and placed in an enclosed chamber shown in Fig. 6.3 at ambient pressure and temperature for 1–2 h until the thermal probe temperatures reached steady state and recorded during this period. Typical temperature profile of silica aerogel and composite under the 5 level of power input is shown in Fig. 6.4.

The thermal conductivity of any substance is given by Eq. 6.2, where $\dot{Q}$, is the quantity of heat flowing in watts; $\lambda$ is the thermal conductivity in W/K-m; d$T$/d$x$ is the temperature gradient in K/m, across a sample of the material of uniform cross-sectional area $A_y$ m$^2$.

$$\dot{Q} = (\lambda A_y)_{com} \frac{(T_2 - T_3)}{t_{com}} \tag{6.2}$$

When the electrical heater is turned on, heat will flow from the heater into CPs 1 and 2 and from CP2 across the composite block to CP3. The heat will be lost to the environment by emission and convection from the surface areas of CP1 and

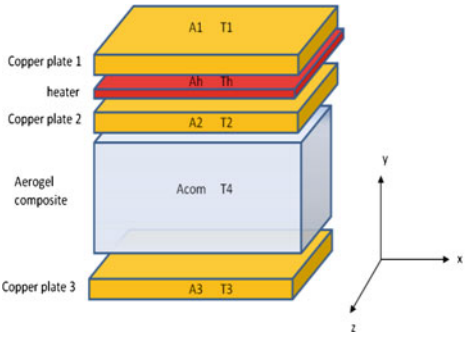


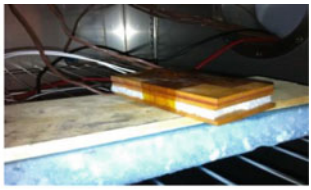

$A_1$ - Emitting surface area of CP1
$A_2$ – Emitting rim surface area of CP2
$A_3$ – Emitting surface area of CP3
$A_{com}$ - Emitting surface area of composite block
$A_h$ – Emitting rim surface area of heater
$T_h$- Temperature of heater
$T_{1,2,3}$– Temperature of CP
$T_4$ – Temperature of composite block
VI – Power supplied

**Fig. 6.2** Thermal conductivity experimental setup using Lee's Disc method


| Thermotron SE-300 Specification | |
|---|---|
| **Operating Temp (°C)** | -70 to 180 |
| **Relative Humidity (%)** | 10 - 98 |
| **Application:**<br>**Behavior of composite materials under controlled temperature and humidity.**<br>**Monitor thermal response of composites under pre-defined thermal cycles.** | |

**Fig. 6.3** Thermotron SE-300 enclosed chamber to monitor behavior of composite materials under controlled temperature and humidity

CP3 and from the rim of CP2, the rim of the heater, and the rim of composite. The rate of loss of heat of a particular plate will be proportional to the temperature difference between the disc and its surroundings, provided this temperature difference is small (Newton's law of cooling). The temperature of the three plates and the composite will increase until the rate of heat loss to the room is equal to the rate of heat generation in the electrical heater assuming the temperature boundary is uniform across the surfaces and edges for the individual parts. When this occurs equilibrium has been reached and therefore,

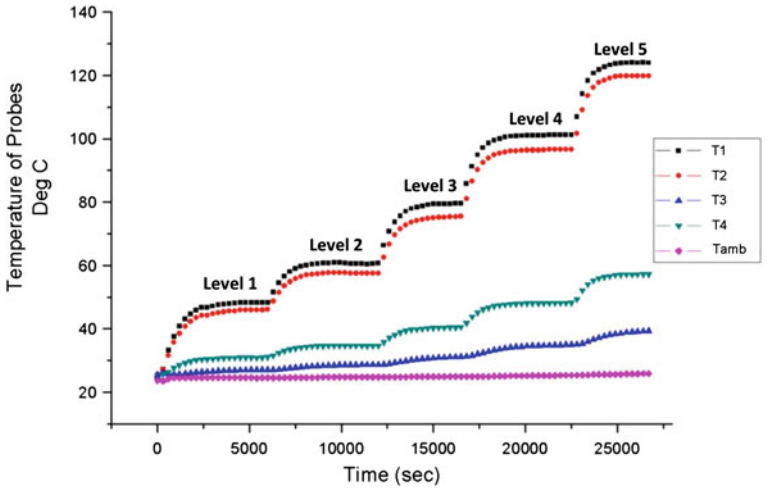


**Fig. 6.4** Experimental temperature profile of silica aerogel granules under various power loading

$$VI = e_1\{A_1(T_1 - T_s) + A_2(T_2 - T_s) + A_3(T_3 - T_s) + A_h(T_h - T_s)\} + e_2 A_{com}(T_4 - T_s) \tag{6.3}$$

where,

$e_1, e_2$ = Heat loss per unit area of copper and composite respectively,
$T_s$ = Ambient temperature,
$VI$ = Power supplied by the heater in watts

Given that the cross-sectional area remains the same across all CPs, heater and the composite, the above equation can be written in terms of the thickness ($t$) and perimeter ($P$).

$$\begin{aligned} VI = [e_1\{(A_1(T_1 - T_s) + (Pt_2(T_2 - T_s) + (A_3(T_3 - T_s) \\ + (Pt_h(T_h - T_s)\} \ + e_2 P(t_{com}(T_4 - T_s)] \end{aligned} \tag{6.4}$$

The above Eq. 6.4 has two heat loss constants that can be converted into single heat loss constant by using the thermal mass relationship between the copper and composite. For a body of uniform composition, thermal mass, $C_{th}$, can be approximated by $C_{th} = m * c_p$, where $m$ is the mass of the body and $c_p$ is the isobaric specific heat capacity of the material averaged over temperature range in question. Thus, the equivalent thermal mass for a copper plate to aerogel composite for a constant cross-sectional area ($A_{xz}$) will be as follows:

$$(t)_{copper(eq)} = \frac{t_{com}(\rho * c_p)_{com}}{(\rho * c_p)_{copper(eq)}} \tag{6.5}$$

Equation 6.5 shows the equivalent thickness of a copper plate that will have the same thermal mass as the aerogel composite. Table 6.1 shows the specific heat capacities of the materials used in the experiment. The specific heat capacity for the aerogel composite is estimated using the rule of mixture as shown where $x$ is the weight fraction of the aerogels and $y$ is the weight fraction of FMWNT. Where there

**Table 6.1** Thermal conductivity, density, and specific heat capacity data

| Material | $c_p$ (J/g-K) | $\rho$ (g/cm$^3$) | $\lambda$ (W/m-K) |
|---|---|---|---|
| Copper | 0.39 | 0.89 | 390 |
| Aerogel | 0.7–1.15 (Reim et al. 2004) | 0.07123 | 0.01–0.04 (Reim et al. 2004) |
| Gelatin | 1.256–3.98 (Chen et al. 2009) | [a]0.8925–1.1940 | 0.1924–0.356 (Chen et al. 2009)<br>[a]0.152–0.235 |
| FMWNT | 0.75–0.9 @ 360 K (Pradhan 2010) | 2.1 | |

[a]Data from in-house experiments of gelatin films for density, modulus, strength, and thermal conductivity

are more than two constituent materials involved in the composite, their individual weight fractions are to be accounted in the rule of mixture equation as follows in Eq. 6.6.

$$(c_p)_{com} = x(c_p)_{aerogel} + (1-x)(c_p)_{gelatin} + y(c_p)_{FMWNT} \tag{6.6}$$

Combining Eqs. (6.4), (6.5), and (6.6) will yield new equations as follows; Eq. 6.7a—accounted for heat loss from composite due to the side surface area and Eq. 6.7b—without heat loss from composite that can be used in determining the heat loss per unit area.

$$e_{1(\text{with HL})} = VI/\left[\{A_1(T_1+T_3-2T_s)\} + \left\{A_2\left(T_2+\frac{1}{3}T_h-\frac{4}{3}T_s\right)\right\} + \left\{P_{com}t_{copper(eq)}(T_4-T_s)\right\}\right] \tag{6.7a}$$

$$e_{1(\text{without HL})} = VI/\left[\{A_1(T_1+T_3-2T_s)\} + \left\{A_2\left(T_2+\frac{1}{3}T_h-\frac{4}{3}T_s\right)\right\}\right] \tag{6.7b}$$

The amount of heat crossing the aerogel sample is the amount of heat emitted from CP3, which is

$$\dot{Q} = e_{1(\text{with HL})}A_3(T_3-T_s) \tag{6.8a}$$

$$\dot{Q} = e_{1(\text{without HL})}A_3(T_3-T_s) \tag{6.8b}$$

Substituting Eqs. 6.8a and 6.8b into Eq. 6.2 will yield the 1-D steady-state heat transport Eqs. 6.9a and 6.9b that relate to the thermal conductivity of the composite by accounting for heat loss due to the side surface. The two equations will show the effect on the composite due to heat loss to surrounding.

$$\lambda_{com(\text{withHL})} = \frac{\left[t_{com}e_{1(\text{withHL})}A_3(T_3-T_s)\right]}{A_{ycom}(T_2-T_3)} \tag{6.9a}$$

$$\lambda_{com(\text{without HL})} = \frac{\left[t_{com}e_{1(\text{without HL})}A_3((T_3-T_s)\right]}{A_{ycom}(T_2-T_3)} \tag{6.9b}$$

## 6.3 Operating Temperature of GSA–SDS Composites

It is important that the operating temperatures of the composite blocks are determined prior to the thermal conductivity experiments. Silica aerogels have high melting temperature beyond 1000 °C. Their useful operating temperature is around 300–500 °C and thus any thermal deterioration of the composites will be due to the

gelatin network since gelatin has lower melting points. A preliminary experiment on the operating temperatures of the composite is carried out by heating each specimen at 150–350 °C every 50 °C interval for 3 h in a convectional binder oven. The change in the color of the composite from very light brown to blackish brown above 200 °C is considered to suggest deterioration of the gelatin; refer Fig. 6.5a, b. The composite blocks, however, are able to hold its form at 150–200 °C range.

The lower temperature threshold is tested by submerging the specimens in boiling liquid nitrogen held at −196 °C in a Dewar's Flask for 6 h to examine signs of deterioration of the gelatin network on the aerogel. The specimens were able to stay intact despite being subjected to extremely low temperature as shown in Fig. 6.5c. Thus, the composites have shown to possess a wide temperature range from cryogenic to elevated temperatures, from −196 to 180 °C respectively.

## 6.4 Silica Aerogel Granule Size Distribution

The aerogel granules are placed in a mechanical sieve shaker consisting of 7 sieve sizes and a pan. The granules are sorted according to their particle distribution from 10 sample sets. Appendix 6A shows the distribution of the various sizes from the 10 sets of these granules. The distribution shows that the bulk of the sizes range from 1.4 to 1.99 mm accounting for more than 70 % in all the 10 sets. As observed, most of the granule sizes are in the range of 1.00–2.8 mm accounting for 95 % of

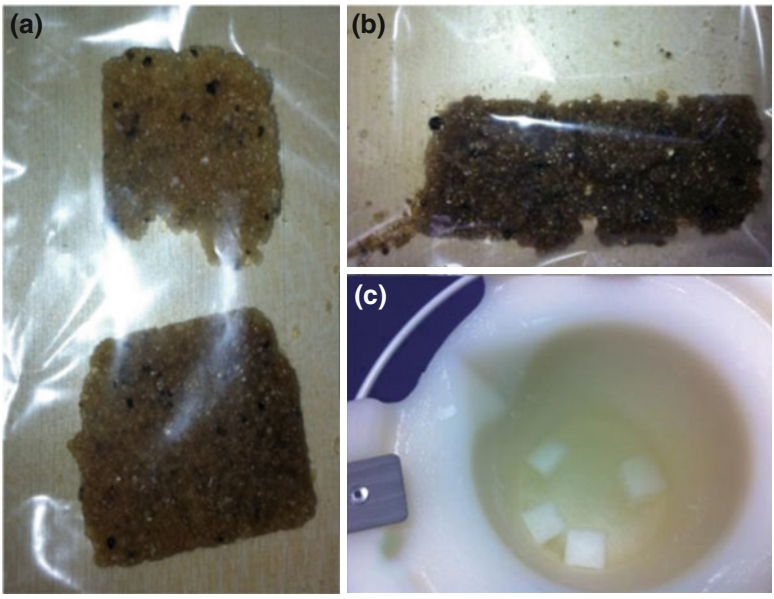


**Fig. 6.5** Specimens **a** heated at 250 °C; **b** heated at 350 °C; **c** submerged in LN2 @ −196 °C

the distribution. Thus, the median granule size is determined to be 1.76 mm by performing the cumulative frequency distribution.

For any given sample of the aerogel granules, the average distribution of the sizes in the sample can be estimated by fitting a two-term Gaussian function as shown in Fig. 6.6. Therefore, the aerogel bulk property $\emptyset_a(d)$, in terms of the granule size $d$ in a given sample can generally be estimated by the product of the two-term weighted Gaussian function and the material property determined for the particular granule size. The coefficients for the function are resolved using curve fitting function in MATLAB as shown in Eq. 6.10. For simplicity, the given two-term weighted Gaussian function herein will be expressed as $\sum_{i=1}^{N} w_i(d_i)$.

$$\emptyset_a(d) = \frac{\sum_{i=1}^{N}\left(\left\{0.5794 * e^{-\left[\left(\frac{d_i - 0.173}{0.03751}\right)^2\right]} + 0.08827 * e^{-\left[\left(\frac{d_i - 0.2067}{0.07171}\right)^2\right]}\right\} * \emptyset\right)}{\sum_{i=1}^{N}\left\{0.5794 * e^{-\left[\left(\frac{d_i - 0.173}{0.03751}\right)^2\right]} + 0.08827 * e^{-\left[\left(\frac{d_i - 0.2067}{0.07171}\right)^2\right]}\right\}} \quad (6.10)$$

## 6.5 Thermal Conductivity of Silica Aerogel Granules

A total of four sets of silica aerel granule sizes ranging from 1.00 to 2.80 mm and one sample of mixed size granules (1.00–4.00 mm) are evaluated for thermal conductivity, $\lambda_a$, in the same manner as described in the previous section. Figure 6.7a shows the experimentally determined thermal conductivity of the

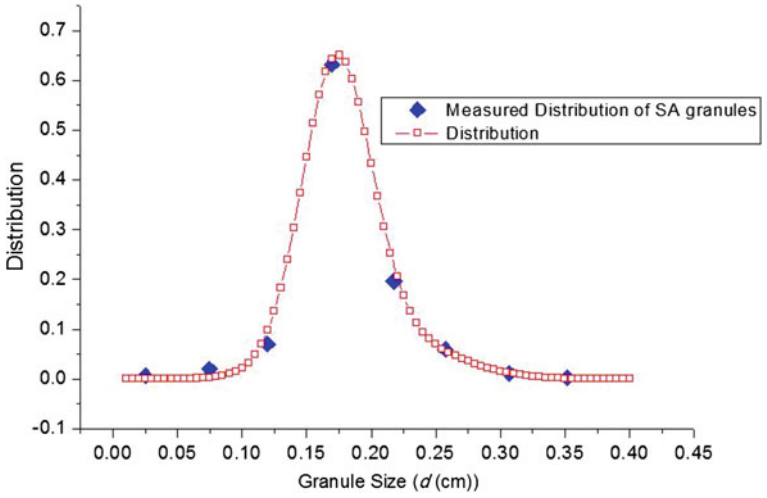


**Fig. 6.6** Weighted two-term Gaussian fitted function to represent the distribution of silica aerogel granules in terms of size $d$ (cm)

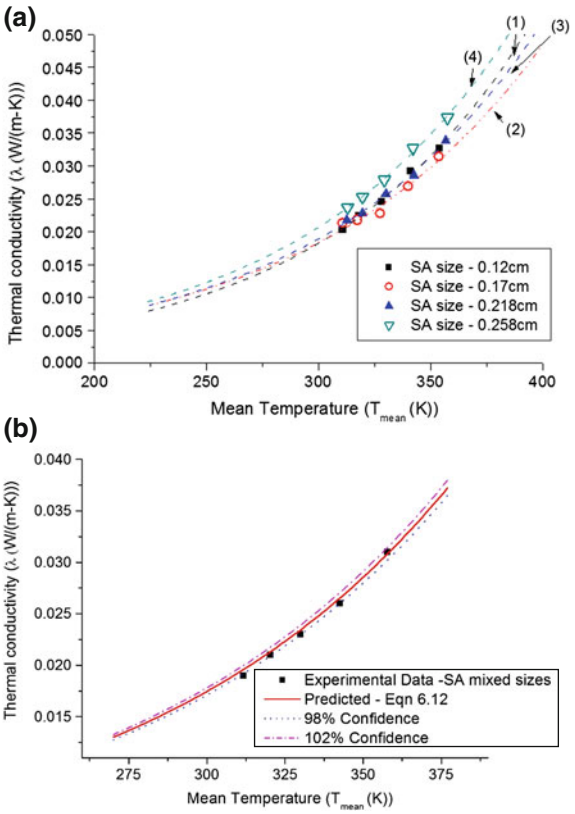


**Fig. 6.7** **a** Thermal conductivity of silica aerogel granules of various sizes as a function of $T_{mean}$; **b** experimental versus predicted formulation (Eq. 6.12)

granules of various sizes plotted from the data as per Eq. 6.9a. The error from the difference between Eqs. 6.9a and 6.9b is approximately 3.4 %. The mean temperature ($T_{mean}$) is the average between CP1 and CP3. The thermal conductivity of each size of aerogel granules can be best represented as an exponential function as shown in the figure for temperature profile from 270 to 377 K. Therefore, the general equation (Eq. 6.11) of thermal conductivity for the silica aerogels is as follows, where the coefficients $A$ and $B$ are the constants of the respective granule size given in Table 6.2. The constants are resolved by curve fitting function using MATLAB.

$$\lambda_a(d, T_{mean}) = A(d) * \exp[B(d) * T_{mean}] \tag{6.11}$$

The thermal conductivity in general increased with increasing the granule size and the value of $T_{mean}$. For a sample lot of granules of sizes varying from 1.0 to 2.8 mm, the thermal conductivity can be empirically estimated as the product of two-term Gaussian function and the above exponential function for each granule size as shown in Eq. 6.12 as functions of $T_{mean}$ and granule size.

**Table 6.2** $A$ and $B$ constants and $R^2$ values of respective aerogel granule size thermal conductivity

| | Size range | Median | Constants | | $R^2$ |
|---|---|---|---|---|---|
| | $d$ (mm) | $d$ (cm) | $A$ | $B$ | |
| (1) | $1.00 \le x < 1.40$ | 0.12 | 0.00068 | 0.0101 | 0.9917 |
| (2) | $1.40 \le x < 2.00$ | 0.17 | 0.00099 | 0.0097 | 0.9524 |
| (3) | $2.00 \le x < 2.36$ | 0.218 | 0.00092 | 0.0101 | 0.9933 |
| (4) | $2.36 \le x < 2.8$ | 0.258 | 0.00091 | 0.0104 | 0.9946 |

$$\lambda_{\text{abulk}}(d, T_{\text{mean}}) = \frac{\sum_{i=1}^{N} w_i(d_i)\{A(d) * \exp[B(d) * T_{\text{mean}}]\}}{\sum_{i=1}^{N} w_i(d_i)} \tag{6.12}$$

The estimated model from Eq. 6.12 is plotted in Fig. 6.7b—red line. The estimated model exhibits good correlation when compared with the measured values of mixed granules sizes (sample size from 1.00 to 4.00 mm). The measured values for the mixed granule sizes lie between ±2.0 % accuracy of the predicted equation. This is a significant result as the predictive model in Eq. 6.12 shows that the thermal conductivity of the silica aerogel granules in a given sample can be determined from its distribution and using the coefficients in Table 6.2. The 2 % error is less than the expected margin of 5 % since the equations account for 95 % distribution of the granules.

## 6.6 Thermal Conductivity of GSA–SDS Composites

Figure 6.8a shows the results of the experimental thermal conductivities for PG, GSA, and GSA–SDS evaluated at $T_{\text{mean}} = 320 \pm 15$ K. The aerogel granules in the GSA and GSA–SDS blocks are of mixed sizes, whereas the PG blocks are purely foamed gelatin that are freeze-dried. PG blocks show higher thermal conductivity in the range of 0.100 ± 0.04 W/m-K for gelatin mass fraction of 0.05–0.5 and have a power law function in the form of $\lambda_{\text{gel}} \propto g^n$, where $g$ is the weight fraction of gelatin. Given that the thermal conductivity of PG is higher than of the aerogels, it is expected that its addition in the composites will increase the overall thermal conductivity. The thermal conductivities of GSA and GSA–SDS composite blocks are observed to be in the range of 0.025 ± 0.005 W/m-K which is approximately 0.006 W/m-K higher than the aerogel granules.

The results between the FM and FD specimens show insignificant difference, although the FD specimens showed an overall increase of 0.003 ± 0.001 W/m-K. However, the FD specimens offer greater consistency as the aerogel granules are closely packed under vacuum. The ‘closeness’ of the granules reduces the ‘air pockets’ within the gelatin network and thus resulting in the marginal increase of the thermal conductivity for the FD specimens. The results of the specimens without SDS are marginally lower but as mentioned in Chap. 5, the GSA

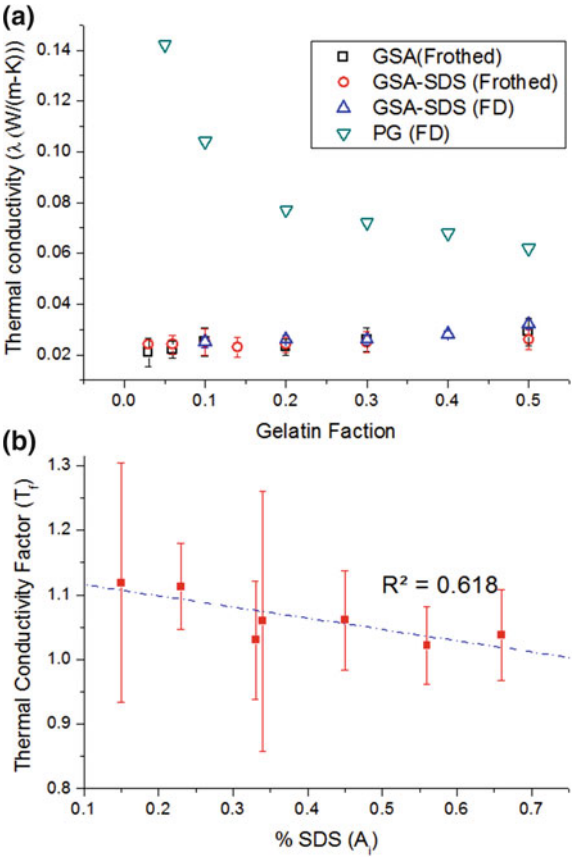


**Fig. 6.8** **a** Thermal conductivity of PG, GSA, GSA–SDS (both FM and FD) specimens evaluated @ $T_m = 320 \pm 5$ K; **b** influence of SDS% on the $T_f$ of the composites

composites do not offer flexibility and high strain recovery (Sachithanadam and Joshi 2013).

The term $T_f$ is introduced here to account for the influence of SDS added into the composite and is the ratio of the thermal conductivities of the composite with SDS and without SDS. The analogy is similar to the relative density and has been used in numerous literatures (Woignier and Phalippou 1988). In Fig. 6.8b, the addition of SDS, however, initially increases the thermal conductivity factor, $T_f$, by $1.066 \pm 0.036$ and exhibits a gradual downward slope even with increasing amount of SDS. It follows a linear function with fit $R^2 = 0.618$.

In the previous chapter, the optimized mechanical properties are achieved when 0.56 %wt. SDS was added to the GSA composites. The GSA–SDS composites of various aerogel granule sizes are fabricated with 0.56 %wt. SDS for gelatin to silica aerogel granules mass fraction ratios of 0.2:0.8 and 0.4:0.6 respectively. The effects of the granule size on the thermal conductivity are investigated for the temperature profile described in Sect. 6.1 is shown in Fig. 6.9.

### 6.6.1 *Influence of Silica Aerogel Granules on the Thermal Conductivity of GSA–SDS (FD) Composites*

It is evident from Fig. 6.9 that the bigger granule sizes have increased thermal conductivity over the smaller ones following the similar trend to that of silica aerogels in Fig. 6.7a. The bigger granules have smaller total surface areas as compared to the smaller granules for the same silica content mass. This ultimately allows the heat transfer to be more prominent for the composites with bigger aerogel granules than the smaller ones thus having higher thermal conductivity. Comparatively, the increase in aerogel granule size increases the thermal conductivity by 0.002–0.005 W/m-K (Fig. 6.9a), whereas the increase was 0.002–0.003 W/m-K when the gelatin content was doubled (Fig. 6.9b). Although the differences are marginal, it can be said that the size of the aerogel granules had greater influence than the gelatin content in deciding the thermal conductivity.

From the experimental results and observations, it can be deduced that the thermal conductivity of the GSA–SDS composite blocks is a function of $T_f$, weight fractions and thermal conductivities of constituent materials and as well as mean temperature, $T_{mean}$. Hence, it can be expressed as $\lambda_{gsasds} = f(T_f, \lambda_{abulk}(d, T_m), \lambda_{gel})$. The predictive model for the thermal conductivity of GSA–SDS is shown in

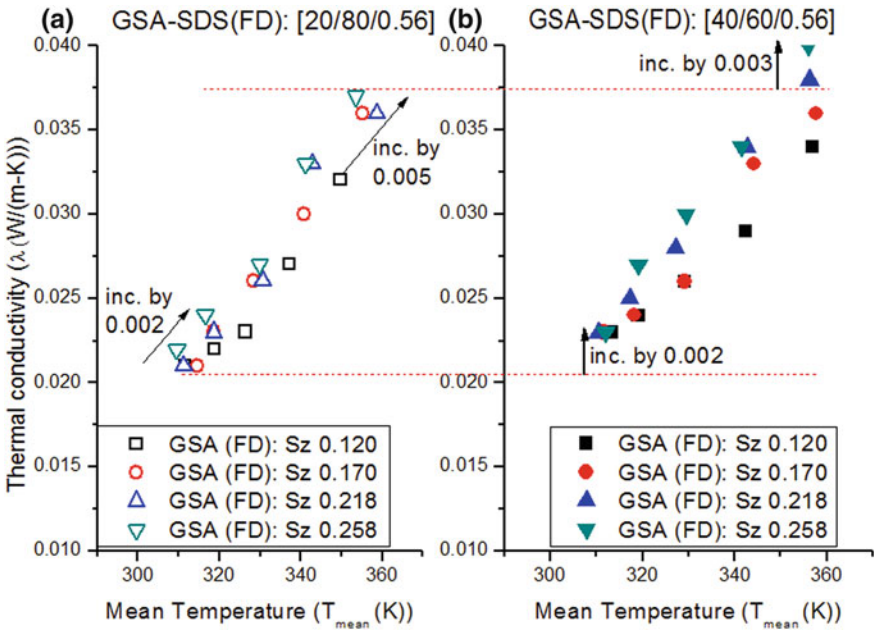


**Fig. 6.9** Influence of granule size and gelatin on thermal conductivity of GSA–SDS composite blocks—**a** 20 %wt gelatin, 80 %wt SA,0.56 %wt SDS; **b** 40 %wt gelatin, 60 %wt SA, 0.56 %wt SDS

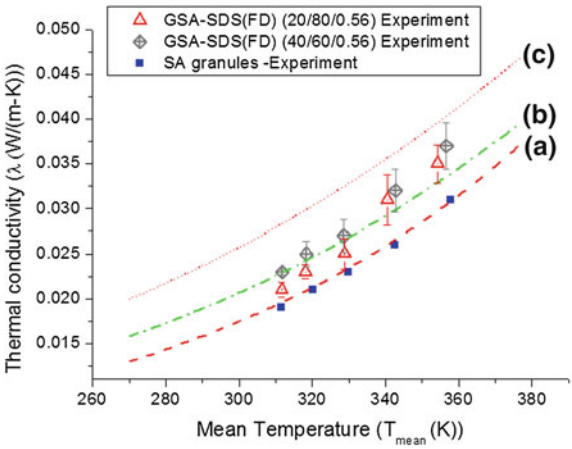


**Fig. 6.10** Predictive model: **a** Aerogel granules; **b** GSA–SDS(20-80-0.56); **c** GSA–SDS(40-60-0.56) versus experimental results

Eq. 6.13 for which the equations of thermal conductivity of the silica aerogel granules and porous gelatin were derived earlier and plotted against the experimental data as shown in Fig. 6.10.

$$\lambda_{\text{gsasds}}(d, T_{\text{m}}) = (1.1277 - 0.1658A_{\text{i}}) * \left[\left(\frac{1-g}{\lambda_{abulk}(d, T_m)}\right) + \left(\frac{g}{\lambda_{gel}}\right)\right]^{-1} \quad (6.13)$$

The predictive model for aerogel granules (depicted by the red dash line) is the same as the one in Fig. 6.7b. The predictive model (green dotted line) for the GSA–SDS (20/80/0.56) composites revealed better correlation with the experimental value with a difference of 0.004 ± 0.001 W/m-K as compared with the predictive model for GSA–SDS (40/60/0.56) (red dotted line) which exhibited a wider difference of approximately 0.006 ± 0.002 W/m-K between the experimental and estimated values.

The error from the predictive model could be attributed to the fact that the $\lambda_{\text{gel}}$ is evaluated at only one temperature profile of 320 K, thus the effects due to temperature variation for the PG blocks are not accounted in the Eq. 6.13. This was also evident with the GSA–SDS (20/80/0.56) composites at the higher temperatures where the predictive model seems to underestimate from the measured data. However, given that the GSA–SDS (20-80-0.56) estimation is closer to the predictive model, this configuration is used in developing the model for the GSA–SDS/FMWNT blocks.

## 6.7 Thermal Conductivity of GSA–SDS/FMWNT Composites

The thermal conductivity experiments for GSA–SDS/FMWNT composite blocks are carried out in the same manner as the other composites for various %wt of FMWNT. The lowest measured thermal conductivity 0.016 W/m-K is obtained

when no SDS is added to GSA in the ratio of 0.1:0.9 by mass fractions of gelatin and silica aerogel respectively. However, as reported in Chap. 5, without SDS the composites offer little functionality and the ability to absorb compression loads.

Similar to the term $T_f$, $T_c$ accounts for the influence of FMWNT in the GSA–SDS composites and is expressed as $T_c = \frac{\lambda_{cn}}{\lambda_{gsasds}}$. Given that $T_f = \frac{\lambda_{gsasds}}{\lambda_{gsa}}$, substituting the two terms and equating the two expressions will result in $\lambda_{cn} = T_c * T_f * \lambda_{gsa}$. Figure 6.7a shows comparison of FMWNT influence on the thermal conductivity of GSA–SDS composites as a ratio $T_c$ with $T_f$. These ratios are evaluated at the mean temperature of 320 ± 5 K for the FM specimens. $\lambda_{gsa}$ is defined to have the baseline coupled factor of 1. The coupled effects of both $T_f$ and $T_c$ exhibit converging trends indicating interdependence of FMWNT and SDS on the thermal conductivity. It is shown that GSA-FMWNT composites have lower conductivity that those without FMWNTs, i.e., $\lambda_{gsa}$. However, with the increasing addition of SDS, the coupled factors with FMWNT show a gradual increase while the one without FMWNT move in the opposite direction till they converge at approximately 0.64–0.67 %wt SDS. The graph with green inverted triangle in Fig. 6.11a represents the average of the coupled factors for the GSA–SDS/FMWNT (FD) specimens evaluated at 0.033 ± 0.017 %wt FMWNT at 0.56 %wt SDS.

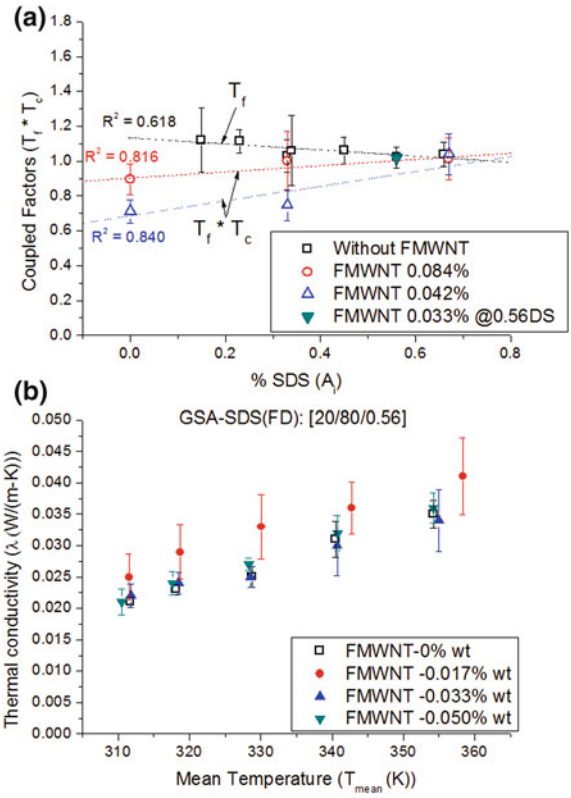


**Fig. 6.11** **a** Influence of both SDS and FMWNT; **b** variations in thermal conductivity of GSA–SDS with doped FMWNT from 0 to 0.05 %wt

The value of the coupled factor is $1.017 \pm 0.17$ which is within the upper and the lower limits of the region. The slightly higher than baseline value of 1 is attributed to the higher thermal conductivities measured for 0.017 %wt FMWNT. Figure 6.11b shows the corresponding thermal conductivities measured for various %wt FMWNT in GSA–SDS composition of 20/80/0.56. It is noteworthy that the composites with 0.033 %wt FMWNT had the lowest thermal conductivities than the rest including the GSA–SDS composites in Fig. 6.10 (red triangles). Therefore, experimental measurements consolidated from FM and FD specimens seem to suggest that thermal conductivities of the GSA–SDS composites doped with FMWNT are lower when 0.033–0.042 %wt FMWNT is added.

A surface response fitting of second-order polynomial function with $R^2 = 0.71$ was plotted in MATLAB to further explore the coupling effects of $T_c * T_f$. Thus, the thermal conductivity for the GSA–SDS/FMWNT composites can be expressed as $\lambda_{cn} = f(T_f, T_c, \lambda_{abulk}(d, T_m), \lambda_{gel})$ and can be evaluated as shown in Eq. 6.14. The full polynomial equation for $(T_f * T_c)$ is given in Appendix 6B.

$$\lambda_{cn}(d, T_m) = (T_f * T_c) * \left[ \left( \frac{1-x}{\lambda_{abulk}(d, T_m)} \right) + \left( \frac{x}{\lambda_{gel}} \right) \right]^{-1} \tag{6.14}$$

Thermal conductivity derived in Eq. 6.14 is plotted and compared with the experimental data of GSA–SDS/FMWNT composites as in Fig. 6.12. The predicted values of the composites differ by $0.003 \pm 0.002$ W/m-K which is marginally small for a temperature profile from 290 to 370 K. Correlation coefficient is a numerical measure of the strength of the relationship between two random variables. The value of correlation coefficient varies from −1 to 1. A value close to +1 or −1 reveals the two variables are highly related. Pearson's product moment correlation coefficient measures the linear relations between two data sets and was determined to be 0.935 between the predicted model (Eq. 6.14) and the experimental data.

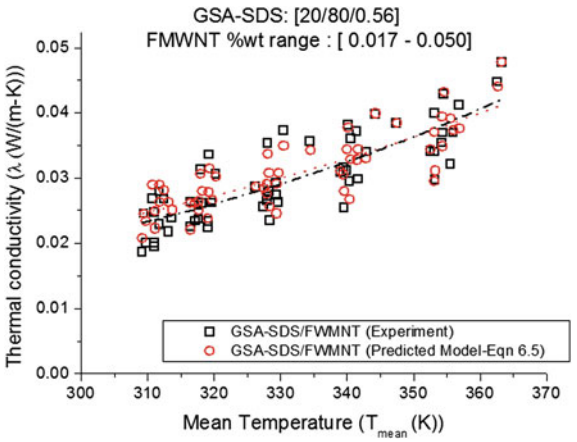


**Fig. 6.12** Comparison of experimental and predictive model GSA–SDS/FMWNT composites thermal conductivity @ 0.56 %SDS

Another statistical correlation tool called the Spearman rank correlation coefficient is more suitable for data that does not fulfill normal distribution and works better in detecting nonlinearity between two variables. The Spearman rank correlation coefficient was determined to be 0.928. Both values show high correlation between the experimental and the predicted model in Eq. 6.14.

### 6.7.1 Optimization and Validation

The coupled function of $f(\alpha, \mathrm{CNT}) = T_c * T_f$ is a second-order polynomial function. The optimal values of the SDS and FMWNT can then be determined using the first and second derivative tests that are commonly used in determining the saddle points and the critical points. Setting $\frac{\partial f}{\partial a}$ and $\frac{\partial f}{\partial \mathrm{cnt}}$ to zero will yield the optimal values of SDS and FMWNT which can be solved simultaneously. Substituting these values into the expression $|H| = \left[\left(\frac{\partial^2 f}{\partial \alpha^2}\right)\left(\frac{\partial^2 f}{\partial \mathrm{cnt}^2}\right) - \left(\frac{\partial^2 f}{\partial a \partial \mathrm{cnt}}\right)^2\right]$ will determine whether the critical points will give the maximum or minimum. The coupled function is optimized when $\frac{\partial^2 f}{\partial \alpha^2} > 0$ and $|H| < 0$. The derivation and the associated calculations for the above test are illustrated in Appendix 6B. The coupled function is optimized when SDS %wt and FMWNT %wt are 0.323 %wt and 0.0303 %wt, respectively, resulting in $T_c * T_f = 0.93$. The above statement translates to the possibility of achieving 7 % lower thermal conductivity using this configuration of SDS and FMWNT as compared to the composite fabricated without the additives, i.e., just a GSA composite. However, this value is mathematically derived from the surface response fitting function of experimental data which may differ if there are more data points. The optimal values though offer a good start point to achieve lower thermal conductivity using FMWNT and SDS as compared to GSA composites. It was noted that the $T_c T_f$ is lower when FMWNT content is between 0.033 and 0.042 %wt and SDS is below 0.33 %wt.

The predictive model was validated with two additional specimens of 0.134 %wt SDS with 0.0167 and 0.0534 %wt FMWNT. The predictive model using the above parameters and the experimental data for validation were plotted as shown in Fig. 6.13. The experimental data as predicted exhibited lower thermal conductivity of approximately 7 % as compared to GSA (without SDS and FMWNT) composites. Furthermore, the data also showed extremely good correlation with the predictive model in Eq. 6.14 offering good measure of approximation to the experimental values.

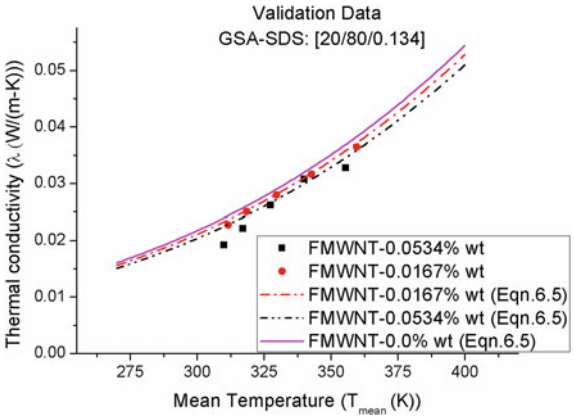


**Fig. 6.13** Validated thermal conductivity of 0.134 % SDS—0.0167 % FMWNT (*red*) and 0.134 % SDS—0.0534 % FMWNT (*black*) with the predictive model (Eq. 6.5) showing lower values of approximately 7 % as compared to GSA (*pink*)

## 6.8 Thermal Transport Phenomenon in GSA–SDS/FMWNT Composites

The transfer of thermal energy occurs via three mechanisms. They are via solid conductivity, gaseous conductivity, and infrared radiation. Figure 6.14 shows a schematic presentation of various modes of thermal transport mechanisms in the GSA–SDS/FMWNT. In addition, the GSA–SDS and GSA–SDS/FMWNT exhibit mechanical properties similar to that of polymeric foam, and thus thermal convection within the cells shall be considered as an additional component in deriving total thermal conductivity, which can be represented by Eq. 6.15.

$$\lambda_T = \lambda_s + \lambda_g + \lambda_c + \lambda_r \tag{6.15}$$

where
$\lambda_T$ is the total thermal conductivity
$\lambda_s$ is the thermal conduction via solid
$\lambda_g$ is the thermal conduction via gas
$\lambda_c$ is the convection within the cells
$\lambda_r$ is the radiation through cell walls and across the cell voids

Minimizing any of the four components of the thermal conductivity will effectively reduce the porous material's overall thermal conductivity. Solid conductivity, $\lambda_s$, is an intrinsic property of a specific basic material. Silica aerogels possess a very small fraction of silica mass (approximately 1–2 %) as compared to the overall

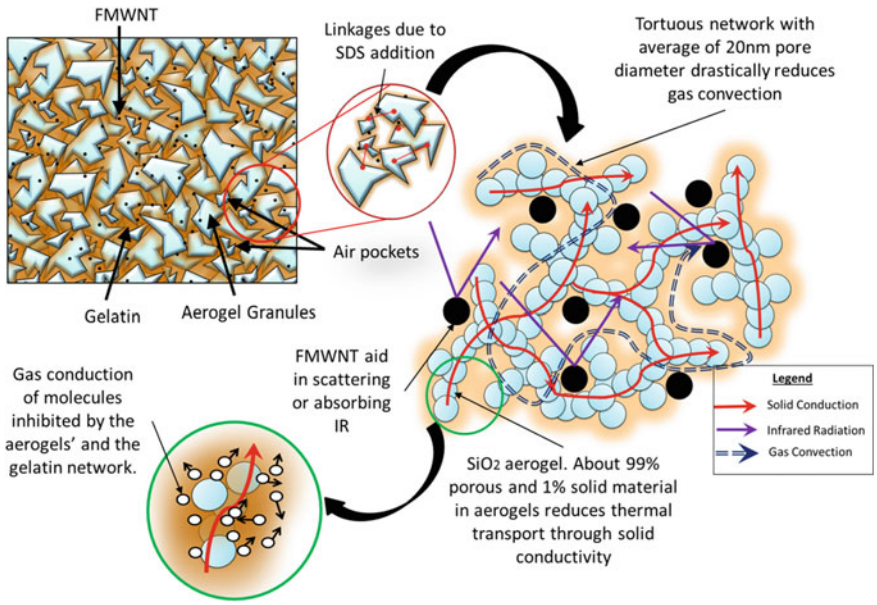


**Fig. 6.14** Schematic representation of the various modes of thermal transport mechanisms in GSA–SDS and GSA–SDS/FMWNT composites

volume. These extremely light nanoparticles are arranged in a 3D amorphous network with many dead ends essentially reduce the thermal transport through solid conduction. Moreover, silica itself is a poor conductor of heat. The spaces not occupied by solids are filled with air or gas which accounts for almost 99 % of the total volume in the aerogels.

The gas conductivity, $\lambda_g$, likewise is inhibited by both the aerogels and porous gelatin network as the gas molecules have limited space to vibrate and move randomly. Gaseous convection, $\lambda_c$ in the aerogels has major influence on the overall thermal conductivity; it is primarily affected by the ratio of the mean free path length of the gas molecules to that of the free space and porosity of the aerogel as reported by Zeng et al. (1995). It was reported that if the mean free path of a particular gas is longer than the pore diameter of the aerogel, the gas molecules will collide with the walls and amongst themselves at a higher rate transferring the thermal energy to the solid particles which already has low intrinsic conductivity. Unlike foams, the aerogel's $\lambda_c$ can be reduced further by simply sealing them in commercially available storage vacuum bags (Zeng et al. 1994). The aerogel granules were purchased commercially with an average pore size of 20 nm is deemed reasonable and adequate. For the gelatin foamed network that binds the aerogels, the Grashof, Gr number is an important consideration in convective thermal transport. It describes the ratio of the buoyant force driving convection to the viscous forces opposing it when it is greater than 1000. It is a function of the cell size, temperature difference of gas across one cell, volumetric expansion of gas,

density and dynamic viscosity of the gas and finally the acceleration due to gravity (Ashby and Gibson 1997). The minimum cell size is determined to be 10 mm when Gr *number* is set to 1000 and given that the aerogels are nanomaterials with the particle sizes in the range of 0.1–4.0 mm and the gelatin network to be in the similar range, the contribution of $\lambda_c$ should be suppressed completely as reported by Baxter and Jones (1972).

The open pores allow thermal transport of gas through the material. At low temperature, radiative thermal transport, $\lambda_r$, is low; however, at high temperature radiation transport becomes dominant and should be suppressed. This can be accomplished by adding carbon which is an effective absorber of infrared radiation. The maximum operating temperature of the GSA–SDS and GSA–SDS/FMWNT composites is approximately 180–200 °C. Although the aerogels can withstand higher temperature, the gelatin network and the binding capacity will deteriorate beyond the operating temperature. Even though all experiments were carried out below the maximum operating temperature, FMWNTs are added nevertheless to study the influence on the overall thermal conductivity at temperatures below 200 °C.

Thus, the thermal conductivity analyzed in this chapter is limited to heat transfer through the solid and gas components of the composites and most importantly the development of predictive model based on the aerogel granule sizes. The thermal conductivity of the aerogels regardless of their irregular shape and size can be expressed as an empirical relation with respect to their mean granule size, and aspect ratio as shown in Fig. 6.7. The experimental results of mixed granules showed excellent correlation with the predictive model given in Eq. 6.12. This forms the basis of expanding the equation to include the effects of other material constituents, namely gelatin, SDS, and FMWNT. While it is generally accepted that thermal conductivity increases with the increasing temperature, the infusion of addition material also affects the heat insulating performance of the aerogel. In the current study, rule of mixture equation to account for the effects of gelatin, SDS, and FMWNT is used, which have been expanded to include the aerogel granules distribution function (i.e., two-term Gaussian function).

The PG blocks thermal conductivity were evaluated in the same corresponding proportions and were used in the rule of mixture equation as shown in the previous section. The effects of SDS were charted as a ratio of composites ($T_f$) with SDS and without SDS as shown Fig. 6.11a. Similarly, given the extremely small amounts of FMWNT used in the composite, the ratio of composites with CNT and without CNT ($T_c$) is also shown in the same figure. These ratios were tabulated from the experimental data and a functional relationship is derived as a result. While the composites have higher thermal conductivity as compared to the neat aerogel granules, it is interesting to know that addition of SDS and FMWNT reduces the mean thermal conductivity of the composites.

Furthermore, the inclusion of FMWNT showed $T_cT_f$ for composites without SDS which is approximately 0.7 and 0.85 for 0.042 %wt and 0.084 %wt respectively. In addition, it was also observed that the coupled effects of FMWNT and SDS showed an increasing trend that eventually converge toward values that are

similar to GSA–SDS. This can be seen from the experimental results of GSA–SDS/FMWNT of 0.033 %wt CNT @ 0.56 %wt SDS annotated by the green inverted triangle on Fig. 6.11a. Thus to achieve lower thermal conductivity, it is best not to use SDS in the mixture. However, as previously reported (Sachithanadam and Joshi 2013, 2014) in our works, without SDS the composites offer little flexibility and application due to brittleness of aerogel granules.

## 6.9 Superhydrophobicity of FMWNT doped GSA–SDS Composites

The GSA composite (FM) was tested for hydrophobic qualities by placing in a beaker of water. The composite was seen floating on top of the water but there was no noticeable surface tension at the edges of the composite. The gelatin network that bonded the silica aerogel granules eventually dissolved in water after 14 days as shown in Fig. 6.15a. The de-bonded granules were still floating on the surface thus the hydrophobic qualities of the aerogels were not significantly compromised. It was also observed that some of the aerogels remained clustered together; again proving that a certain degree of bonding between the $NH_2$ groups gelatin and the oxy-TMS groups of aerogel has taken place. On the contrary, GSA–SDS (FD) composite lasted 7 days longer before the de-bonding of the particles started. This shows that the FD specimens are more compact that the FM specimens aided by physical adhesion between the gelatin network and the aerogel granules during the curing stage. Another specimen that was doped with functionalized FMWNTs

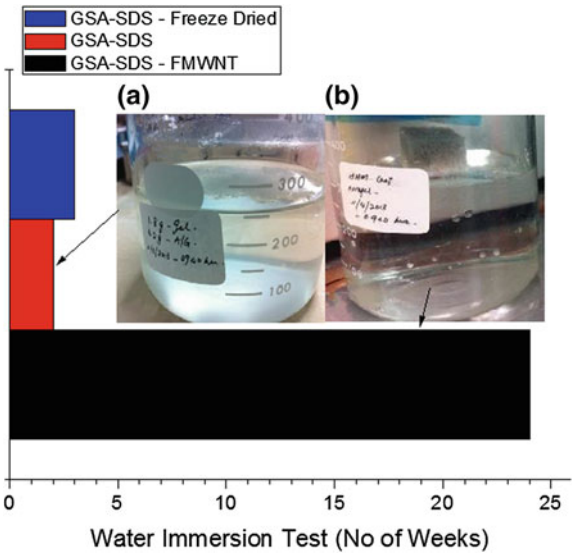


**Fig. 6.15** Water immersion test for hydrophobic quality: **a** GSA–SDS, **b** GSA–SDS/FMWNT specimen

into the aqueous gelatin solution was tested in the same manner as above. The GSA–SDS/FMWNT composite remained in its form for maximum 24 weeks before the gelatin network deteriorated. Furthermore, a surface tension was evident throughout till the last 3 weeks suggesting that deterioration was taking place.

The specimens tested in the preceding sections were evaluated for hydrophobicity by measuring the contact angle. GSA–SDS/FMWNT composite blocks were fabricated in the same manner as previously described with an addition 0.017, 0.033, and 0.05 %wt of FMWNT together with GSA–SDS composites. A total of 16 composite blocks comprising of 48 specimens of various granule sizes were tested for contact angle measurements as per ASTM D-7334 using Attension Theta Optical Tensiometer. Contact angle, $\boldsymbol{\theta}$, is a quantitative measure of wetting of a solid by a liquid. It is defined geometrically as the angle formed by a liquid at the three-phase boundary where a liquid, gas, and solid intersect (Scientific 2015).

The tip of the hypodermic needle is set at a distance approximately 3 mm above from the specimen's surface and deposit a drop of test liquid (distilled water is used throughout the experiments) of about 3–7 μL in size on the specimen. The tiled angle shall be adjusted accordingly. The instrument has inbuilt software based on Young/Laplace fitting method to calculate the contact angle on both sides of the water droplet. The camera is focused to capture the image and the results are tabulated once the 'compute' icon is activated. An average of six measurements on each specimen was taken to determine the contact angle. Figure 6.16 shows the typical measurement taken for GSA–SDS and GSA–SDS/FMWNT specimen. If the contact angle is less than 90° it is said to be hydrophilic and zero contact angle representing complete wetting. Generally, contact angle measurements that show more than 90° indicate that the material is hydrophobic. For superhydrophobic materials the contact angles are greater than 150°.

Figure 6.17 shows the contact angles measured with response to various granules sizes. Generally, all the composites, including GSA–SDS are hydrophobic ($\theta > 90°$). The variations in the contact angle are insignificant in terms of granule

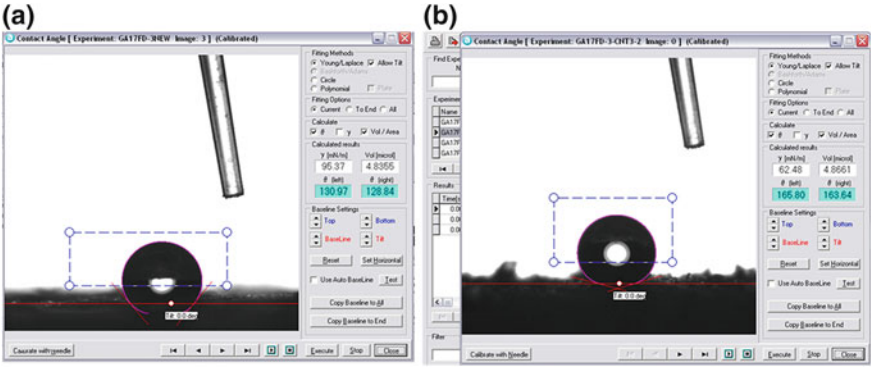


**Fig. 6.16** Contact angle measurement. **a** GSA–SDS [0.2/0.8/0.56]; **b** GSA–SDS/FMWNT [0.2/0.8/0.56/0.050]

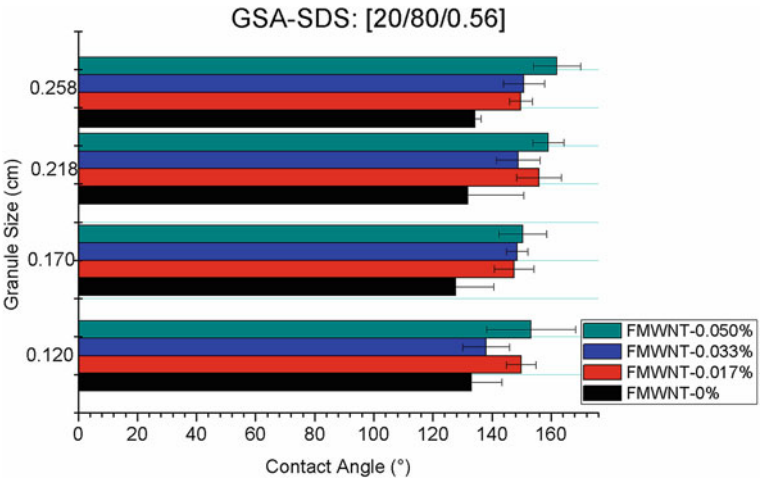


**Fig. 6.17** Variations in contact angle of GSA–SDS due to various silica aerogel granule sizes and FMWNT

sizes. Thus it can be concluded that the size of the granules have very negligible impact on the contact angle. However, in Fig. 6.18, the influence of FMWNT is significant as there is an increase of almost 30°–40° in contact angle. At 0.05 %wt FMWNT, the composites exhibited contact angle of 155° ± 10°. The increase associated with the doping of FMWNT has given composites 'superhydrophobic' quality. Superhydrophobicity is a desirable quality especially for cryogenic insulation blanket materials where condensation of water is prevalent.

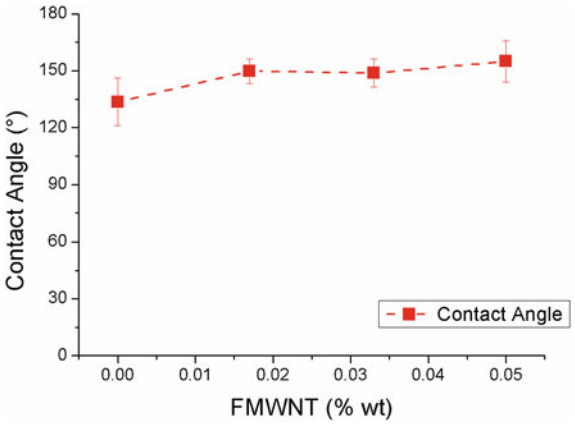


**Fig. 6.18** Superhydrophobicity in GSA–SDS composites associated with doping of FMWNT

## 6.10 Concluding Remarks

Thermal Conductivity of the silica aerogels, GSA, GSA–SDS, and GSA–SDS/FMWNT composites was determined using the Lee's Disc method as described in this chapter. The thermal conductivity of the aerogel granules (1.00–2.80 mm) were in the range from 0.021 to 0.038 W/m-K for temperature profile of 310–3670 K. The thermal conductivity generally increased with the increase in the granule size and it was also the same for the GSA–SDS composite blocks with various granules sizes. A predictive model based on the distribution of the aerogel granules in a given sample was developed using the two-term Gaussian function and showed extremely good estimation. The model was validated with mixed granules and was found close to be within 98 % accuracy.

For the composite blocks, the varying thickness was first converted to equivalent copper thickness by equating the thermal mass equations and also accounted for heat loss from the side area of the blocks. The heat loss due to side area of the composite blocks is approximately 2.77 ± 1.53 %. The thermal conductivities of GSA and GSA–SDS composite blocks were observed to be in the range of 0.025 ± 0.005 W/m-K which is approximately 0.006 W/m-K higher than the of silica aerogel granules. The results between the FM and FD specimens showed insignificant difference, although the FD specimens show an overall increase of 0.003 ± 0.001 W/m-K. The lowest thermal conductivity is obtained when no SDS is added at around 10–20 % of gelatin mass fraction. The terms $T_f$ and $T_c$ account for the influence of SDS and FMWNT in the predictive model respectively. The coupled effects of both $T_f$ and $T_c$ exhibit converging trends indicating that both the FMWNT and SDS are interdependent on the thermal conductivity response. A coupled function, $T_cT_f$ based on second-order polynomial function were derived from these experimental data and included in the predictive model.

The predictive models were developed from the numerous experiments carried out with gelatin, SDS, and FMWNT in various proportions and in terms of the granule sizes. It was noted previously that the $T_cT_f$ is lower when FMWNT is between 0.033 and 0.042 %wt, and SDS is below 0.33 %wt. The model was validated and showed that a reduction of 7 % in thermal conductivity was achieved using GSA–SDS/FMWNT over the GSA composites. The predictive models developed in this chapter offer good estimation to the experimental values within approximately 94.3 ± 2.4 % accuracy. The predictive models derived in Eqs. 6.11–6.14 can be tabulated as a data sheet in a number of ways and presented in terms of temperature profile, granule size, various composition of gelatin, SDS, and FMWNT.

Hydrophobic behavior of the GSA, GSA–SDS, and GSA–SDS/FMWNT was evaluated by means of water contact angle. From the experimental results, it was concluded that the size of the granules have very negligible impact on the contact angle. However, the doping of FMWNT into the GSA–SDS composites showed a transformation from hydrophobic to superhydrophobic quality corresponding with an increase of almost 30°–40° in contact angle. At 0.05 %wt. FMWNT, the

composites exhibited contact angle of 155° ± 10°. Superhydrophobicity is a desirable quality especially for cryogenic insulation blanket materials where condensation of water is prevalent. The swelling of gelatin was observed to be hindered by the addition of FMWNTs when the viscosity of the solution reduced. Thus, FMWNTs being nanosized attached themselves to the end group of gelatin chain preventing them from creating intramolecular bonding and at the same time occupied the spaces between water molecules. By doing so, the hydrophobicity increases with a decrease in the chain strength resulting in the lower strength and modulus. The composites developed have wide operating temperature from −196 to 180 °C.

## Appendix 6A—Granule Size Distribution

See Table 6.3

**Table 6.3** Granule size distribution

| Granule size (mm) | Particle size distribution | | | | | | Max aspect ratio |
|---|---|---|---|---|---|---|---|
| | 1st set (%) | 2nd set (%) | 3rd set (%) | 4th set (%) | 5th set (%) | Average (%) | |
| $3.35 \leq x < 3.75$ | 0.28 | 0.00 | 0.45 | 1.11 | 0.14 | 0.40 | 1.12 |
| $2.8 \leq x < 3.35$ | 0.57 | 0.84 | 0.89 | 1.59 | 1.88 | 1.15 | 1.19 |
| $2.36 \leq x < 2.8$ | 5.67 | 5.25 | 7.61 | 6.52 | 6.50 | 6.31 | 1.18 |
| $2.00 \leq x < 2.36$ | 14.45 | 22.69 | 23.27 | 26.39 | 23.99 | 22.16 | 1.18 |
| $1.40 \leq x < 2.00$ | 73.37 | 65.34 | 60.63 | 58.51 | 57.51 | 63.07 | 1.42 |
| $1.00 \leq x < 1.40$ | 3.40 | 5.46 | 6.26 | 3.50 | 6.79 | 5.08 | 1.39 |
| $0.50 \leq x < 1.00$ | 2.27 | 0.42 | 0.89 | 1.27 | 2.02 | 1.38 | 1.98 |
| $x < 0.5$ | 0.00 | 0.00 | 0.00 | 1.11 | 1.16 | 0.45 | – |
| Granule size (mm) | Particle size distribution | | | | | | Max aspect ratio |
| | 6th set (%) | 7th set (%) | 8th set (%) | 9th set (%) | 11th set (%) | Average | |
| $3.35 \leq x < 3.75$ | 0.00 | 0.16 | 0.00 | 0.16 | 0.00 | 0.04 | 1.12 |
| $2.8 \leq x < 3.35$ | 0.99 | 1.29 | 1.48 | 1.27 | 1.41 | 1.29 | 1.19 |
| $2.36 \leq x < 2.8$ | 4.96 | 5.83 | 5.75 | 5.71 | 6.01 | 5.61 | 1.18 |
| $2.00 \leq x < 2.36$ | 15.04 | 27.51 | 19.05 | 17.78 | 16.96 | 17.21 | 1.18 |
| $1.40 \leq x < 2.00$ | 66.78 | 55.02 | 61.74 | 64.29 | 60.07 | 63.22 | 1.42 |
| $1.00 \leq x < 1.40$ | 9.59 | 7.12 | 8.54 | 8.10 | 9.54 | 8.94 | 1.39 |
| $0.50 \leq x < 1.00$ | 2.15 | 2.43 | 2.79 | 2.22 | 4.06 | 2.81 | 1.98 |
| $x < 0.5$ | 0.50 | 0.65 | 0.66 | 0.48 | 1.94 | 0.89 | – |

## Appendix 6B—Optimization of Coupled Function

### *Derivation of Optimal Values for Coupled Function of SDS and FMWNT*

$$f(\alpha, \mathrm{CNT}) = T_{\mathrm{c}} * T_{\mathrm{f}}$$
$$f(\alpha, \mathrm{CNT}) = 1.023 - 0.8528\alpha + 3.158c + 1.241\alpha^2 + 1.722\alpha c - 61.26c^2$$

### *1st Derivation Test*

$$\frac{\partial f}{\partial \alpha} = 0$$
$$-0.8528 + (2 * 1.241)\alpha + 1.722c = 0 \tag{6.16}$$
$$\frac{\partial f}{\partial c} = 0$$
$$3.158 + 1.722\alpha - (2 * 61.26)c = 0 \tag{6.17}$$

Solving the two equations simultaneously will yield four pairs of values:

| $\alpha$ | $c$ |
|---|---|
| 0.3225 | 0.0303 |

### *2nd Derivation Test*

| $(\alpha, c)$ | $\frac{\partial^2 f}{\partial \alpha^2}$ | $\frac{\partial^2 f}{\partial c^2}$ | $\frac{\partial^2 f}{\partial \alpha \partial c}$ | $\lvert H\rvert = \left[\left(\frac{\partial^2 f}{\partial \alpha^2}\right)\left(\frac{\partial^2 f}{\partial \mathrm{cnt}^2}\right) - \left(\frac{\partial^2 f}{\partial a \partial c}\right)^2\right]$ |
|---|---|---|---|---|
| (0.3225, 0.0303) | 2.482 | −122.52 | 1.722 | −307.05 |

# References


Alnaief, M., and I. Smirnova. 2010. Effect of surface functionalization of silica aerogel on their adsorptive and release properties. *Journal of Non-Crystalline Solids* 356(33–34): 1644–1649.

Ashby, M.F., and L.J. Gibson. 1997. *Cellular solids—Structure and properties*. Cambridge: Cambridge University Press.

Baxter, S., and T.T. Jones. 1972. The physical properties of foamed plastics and their dependence on structure. *Plastic and Polymer* 40(146):69–76.

Bernasconi, A., T. Sleator, D. Posselt, J.K. Kjems, and H.R. Ott. 1992. Dynamic properties of silica aerogels as deduced from specific-heat and thermal-conductivity measurements. *Physical Review B* 45(18): 10363–10376.

Chen, X., Y. Jia, S. Sun, L. Feng, and L. An. 2009. Performance inhomogeneity of gelatin during gelation process. *Polymer* 50(25): 6186–6191.

Cheng, S.C., and R.I. Vachon. 1969. The prediction of the thermal conductivity of two and three phase solid heterogeneous mixtures. *International Journal of Heat and Mass Transfer* 12(3): 249–264.

Chibowski, E. 2007. On some relations between advancing, receding and Young's contact angles. *Advances in Colloid and Interface Science* 133(1): 51–59.

Ge, D.T., L.L. Yang, Y. Li, and J.P. Zhao. 2009. Hydrophobic and thermal insulation properties of silica aerogel/epoxy composite. *Journal of Non-Crystalline Solids* 355(52–54): 2610–2615.

Hunt, A.J., C.A. Jantzen and W. Cao. 1991. Aerogel. A high performance insulating material at 0.1 bar. Insulation Materials: Testing and Applications, Gatlinburg, TN, USA, Publ by ASTM, 10–12 Oct 1991.

Lee, K.-H., S.-Y. Kim, and K.-P. Yoo. 1995. Low-density, hydrophobic aerogels. *Journal of Non-Crystalline Solids* 186: 18–22.

Pradhan, N.R. 2010. Thermal conductivity of nanowires, nanotubes and polymer-nanotube composites. Doctor of Philosophy, Worcester Polytechnic Institute.

Qin, G., Y. Yao, W. Wei, and T. Zhang. 2013. Preparation of hydrophobic granular silica aerogels and adsorption of phenol from water. *Applied Surface Science* 280: 806–811.

Rao, A.P., G.M. Pajonk, and A.V. Rao. 2005. Effect of preparation conditions on the physical and hydrophobic properties of two step processed ambient pressure dried silica aerogels. *Journal of Materials Science* 40(13): 3481–3489.

Reim, M., W. Körner, J. Manara, S. Korder, M. Arduini-Schuster, H.P. Ebert, and J. Fricke. 2005. Silica aerogel granulate material for thermal insulation and daylighting. *Solar Energy* 79(2): 131–139.

Reim, M., G. Reichenauer, W. Körner, J. Manara, M. Arduini-Schuster, S. Korder, A. Beck, and J. Fricke. 2004. Silica-aerogel granulate—Structural, optical and thermal properties. *Journal of Non-Crystalline Solids* 350: 358–363.

Sachithanadam, M., and S.C. Joshi. 2013. High strain recovery with improved mechanical properties of gelatin–silica aerogel composites post-binding treatment. *Journal of Materials Science* 49(1): 163–179.

Sachithanadam, M., and S.C. Joshi. 2014. A new phenomenon of compressive strain recovery in gelatin-silica aerogel composites with SDS. *Procedia Engineering* 75: 51–55.

Schmidt, M., and F. Schwertfeger. 1998. Applications for silica aerogel products. *Journal of Non-Crystalline Solids* 225: 364–368.

Scientific, B. 2015. Theory note 1 static and dynamic contact angles and their measurement techniques.

Smirnova, I., S. Suttiruengwong, and W. Arlt. 2004. Feasibility study of hydrophilic and hydrophobic silica aerogels as drug delivery systems. *Journal of Non-Crystalline Solids* 350: 54–60.

van Bommel, M.J., C.W.D. Engelsen, and J.C. van Miltenburg. 1997. A thermoporometry study of fumed silica/aerogel composites. *Journal of Porous Materials* 4(3): 143–150.

Woignier, T., and J. Phalippou. 1988. Mechanical strength of silica aerogels. *Journal of Non-Crystalline Solids* 100(1–3): 404–408.

Zeng, S.Q., A. Hunt, and R. Greif. 1995. Transport properties of gas in silica aerogel. *Journal of Non-Crystalline Solids* 186: 264–270.

Zeng, S.Q., A.J. Hunt, W. Cao, and R. Greif. 1994. Pore size distribution and apparent gas thermal conductivity of silica aerogel. *Journal of Heat Transfer* 116(3): 756–759.

# Chapter 7
# Acoustic Performance of Silica Aerogel Composites

## 7.1 Introduction

Acoustics is the interdisciplinary science that deals with the study of mechanical waves and vibrations in the three states of matter with the aid of a medium to propagate. Sound is often described as audible waves and vibrations in the spectrum of 20–20 kHz (Dowling and Williams 1983). The sound source creates vibrations in the surrounding medium. As the source continues to vibrate the medium, the vibrations propagate away from the source at the speed of sound, thus forming the sound wave. At a fixed distance from the source, the pressure, velocity, and displacement of the medium vary in time. At an instant in time, the pressure, velocity, and displacement vary in space. The particles of the medium do not travel with the sound wave but the relative displacement or vibration from the fixed positions that result in wave propagation (Dowling and Williams 1983). These waves can be reflected, refracted, or attenuated by the medium.

Sound waves propagate fastest in solids; however, the phenomenon in a highly porous solids such as SAs, the sound velocities were observed to be of the order of 100 $ms^{-1}$ (Fricke and Reichenauer 2011), which is about 1/3 the velocity of sound in air. Gross et al. (1992) noted that the lowest sound velocity achieved to be in the range of 80–100 $ms^{-1}$ for nonevacuated SA with a density of approximately 20 kg $m^{-3}$. It was determined that variation of density follows a simple scaling law. Direct measurements were also taken in the form of impedance tube filled with aerogel granules of uniform sizes. Forest et al. (2001) revealed that smaller granules of 80 μm have a sound velocity of approximately 60–70 $ms^{-1}$ achieving sound attenuation of 10 dB compared to glass wool. Caponi et al. (2004) investigated that by growing the density of gels up to values close to that of dense vitreous silica, the acoustic attenuation shows a strongly temperature-dependent behavior, due to the scattering of phonons by pores in the aerogels. Similarly, Bheekhun et al. (2013) reviewed that the low modulus of silica aerogels, which is highly dependent on the



M. Sachithanadam and S.C. Joshi, *Silica Aerogel Composites*,
Engineering Materials, DOI 10.1007/978-981-10-0440-7_7

synthesis is attributable to the acoustics absorption performance as a promising material for airborne ultrasonic transducers.

Acoustic performance of silica aerogel granules previously reported by Forest et al. (2001) achieved sound velocity of approximately 60–70 $ms^{-1}$. The acoustic transmission loss of silica aerogels granules of two sizes, 80 μm and 3.5 mm, by impedance matching technique was evaluated to be at least 10 dB higher than a glass wool of the same thickness (Forest et al. 2001). On-field investigations by Cotana et al. (2014) on glazing system filled with aerogel granules for thermal, acoustics, and lighting performance of a prototype building revealed high corelation among the three properties. The promising results further elevate the diverse applicability of silica aerogels for various economic sectors and industries as highlighted by Buratti and Moretti (2013) in the book titled "Nanotechnology in Eco-Efficient Construction." The acoustic properties of silica aerogels are greatly influenced by various parameters such as; (a) different chemical reactions during gelation stage of aerogel formation (Forest et al. 1998); (b) gas pressure and Young's modulus of the silica aerogel skeleton structure (Gross et al. 1992); (c) and the change in the ratio characteristics impedance between the medium and absorption material that determines the variation in the magnitude of reflection and transmission wave (Kim 2010a, b). Besides these factors, the type of reinforcement can also significantly enhance the acoustic absorption of silica aerogel granules as revealed by Riffat and Qiu (2013).

Several methods have been used in determining the transmission loss (TL). Vigran (2012) used two different approaches using the full transfer matrix (TM method) and another based on the wave field decomposition method. However, to implement both techniques, it is necessary to use the 4-microphone impedance tube. Smith and Parrott (1983) proposed the use of surface methods in determining the acoustic properties; in this case, the propagation constant, by exploiting the changes in surface impedance of specimens. However, this method requires unwrapping of phase information, which resides in the imaginary part of the propagation constant to be carried out before any subsequent calculations can be done. In addition, two-thickness method mentioned previously is more inclined towards well-behaved impedance data where the extraction can be easily automated (Palumbo et al. 2004).

In the previous chapters, we had developed a low cost binder-treated silica aerogel composites using gelatin as the main binder that exhibited high strain recovery with superior mechanical properties than silica aerogels (Sachithanadam and Joshi 2013, 2014) accompanied with super-insulation performance (Mahesh and Joshi 2015). This work is an extension of our previous works to study the effects of the silica aerogel granule sizes on the acoustic properties of the GSA–SDS composites with the following objectives in mind. First, the acoustic properties of the silica aerogel granules of various sizes from 0.50 to 3.35 mm, distributed into six groups of nominal sizes, measured via 2-microphone impedance tube are presented. In addition, GSA–SDS specimens comprising of 1.2 and 1.7 mm granules are fabricated and compared with silica aerogel granules for variations in acoustic behavior. Second, a simplified novel approach to measure TL by 'inferential' principle is proposed and the results are validated with the sound meter

measurements. Third, a comparative study of the GSA–SDS acoustic absorption coefficient with traditional absorption material is carried out.

## 7.2 Experimental Procedure

Acoustics measurement for the silica aerogel granules and GSA–SDS variant composites were carried out as per ASTM E1050 using the Bruel and Kjaer (B&K) Type 4206 Impedance Tube Kit coupled with Digital Frequency Analysis System (International 2012) and in conjunction with an integrated software package called PULSE. Random noise or white noise as it is commonly known, is generated by using a B&K generator module Type 3107 that is equipped with 4-channel microphone module type 3028 and amplified using power amplifier type 2718 set at 1 ampere RMS with zero degree phase input/output. B&K Pulse testing program type 7758 is the integrated software that interfaces the signals into experimental data. The experimental setup for the measurement is shown in Fig. 7.1.

### *7.2.1 Transfer Function Method (2-microphone)*

Figure 7.2 shows the mechanism of the plane waves generated from the sound source within the impedance tube. A source sound usually a loudspeaker is mounted at one end of the impedance tube and a sample of the material is placed at the other end. The speaker generates broadband, stationary random sound waves which will propagate as plane waves hitting the sample and reflect. The decomposition of the stationary sound waves pattern into forward and backward traveling components inside the tube and produces a standing wave interference pattern. By simultaneously measuring the sound pressures at two fixed locations (mic 1 and 2) and calculating the complex transfer function, it is possible to determine the

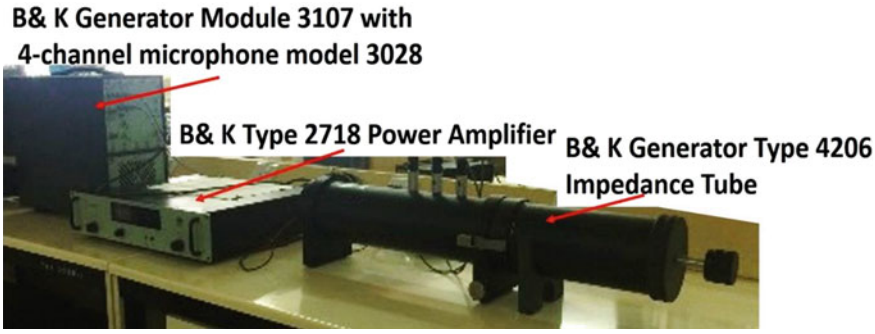


**Fig. 7.1** Experimental setup using the B&K type 4206 impedance tube kit as per ASTM E1050

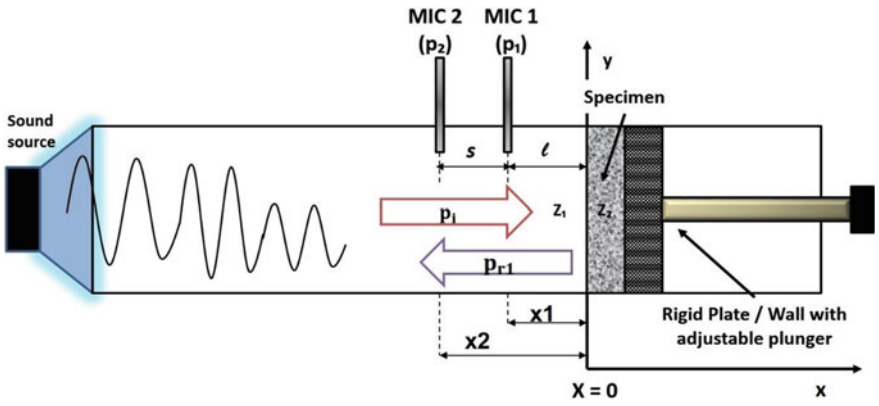


**Fig. 7.2** Schematic of plane wave generation for acoustic measurement using 2-microphone impedance tube

complex reflection coefficient, the sound absorption coefficient and the normal acoustic impedance of the specimen. The reference plane ($x = 0$) is taken as the front surface of the specimen as indicated in Fig. 7.2. The usable frequency range depends on the diameter of the tube and the spacing between the microphone positions. B&K 4206 Impedance Tube Kit comes with a large tube of 100 mm and a small tube of 29 mm, which measures the frequency range from 50 to 1600 Hz and 500 to 6400 Hz respectively.

Silica aerogel granules, being highly porous solids, have the potential to be a sound absorbent material. Sound absorbers are usually characterized by surface impedance and absorption coefficient. A one-dimensional plane wave in the tube is assumed to be $pe^{j(\omega t - kx)}$ (Sung Soo et al. 2008). The total acoustic pressures about the fixed locations at the two microphones, $p_1$ and $p_2$ can be expressed as follows in Eqs. (7.1a) and (7.1b). The time-dependent term that represents the pressure perturbations in a traveling waves with respect to $x$ direction, is eliminated since the microphones are at the fixed location.

$$p_1 = p_\mathrm{i} e^{-jkx1} + p_\mathrm{r1} e^{jkx1} \tag{7.1a}$$

$$p_2 = p_\mathrm{i} e^{-jkx2} + p_\mathrm{r1} e^{jkx2} \tag{7.1b}$$

where:

(a) $p_\mathrm{i}$ and $p_\mathrm{r1}$ are the sound amplitude of the incident and reflected pressure respectively.
(b) $k$ is the wavenumber of the incident sound pressure, therefore $k = \frac{2\pi f}{c}$.
(c) $f$ is the frequency and $c$ is the speed of sound.
(d) $x1 = -l$ and $x2 = -s - l$ are the distances from the specimen to the microphones 1 and 2, respectively.

The complex reflection coefficient $R_1$ is the ratio of the reflected wave to the incident wave. The transfer function $H$ is defined as the ratio between the acoustic measurements of $p_1$ to $p_2$. Equations (7.1a) and (7.1b) can be rearranged as shown in Eqs. (7.2a)–(7.2c):

$$p_{\mathrm{i}} = \frac{j\left(p_1 e^{jkx2} - p_2 e^{jkx1}\right)}{2\sin k(x_1 - x_2)} \tag{7.2a}$$

$$p_{\mathrm{r1}} = \frac{j\left(p_2 e^{-jkx1} - p_1 e^{-jkx2}\right)}{2\sin k(x_1 - x_2)} \tag{7.2b}$$

$$R_1 = \frac{p_{\mathrm{r1}}}{p_{\mathrm{i}}} = \frac{\left(p_2 e^{-jkx1} - p_1 e^{-jkx2}\right)}{\left(p_1 e^{jkx2} - p_2 e^{jkx1}\right)} \tag{7.2c}$$

Substituting $H = p_1/p_2$, $x1 = -l$ and $x2 = -s - l$ will yield the complex reflection coefficient, $R_1$.

$$R_1 = e^{j2k(s+l)} * \frac{\left(e^{-jks} - H\right)}{\left(H - e^{jks}\right)} \tag{7.3}$$

Equation (7.3) is the reflection coefficient for the two microphone transfer function method. When the specimen is backed by a rigid back wall, there will be no transmitted waves and thus by conservation of energy, all the incident waves are reflected and absorbed. Thus the absorption coefficient ($\alpha_1$), can be expressed as in Eq. (7.4).

$$\alpha_1 = 1 - |R_1|^2 = 1 - R_{\mathrm{r1}}^2 - R_{\mathrm{i1}}^2 \tag{7.4}$$

### 7.2.2 *Inferential Transmission Loss (InTLM)*

One of the drawbacks of the two-microphone transfer function method is that the absorption coefficient determined may not be a true representation of the material's characteristic. In the case of a porous material, such as silica aerogels, the reflected wave from the rigid wall could contribute to a rise in the absorbed energy by the material. To account for this uncertainty, the four-microphone impedance tube setup is usually used to determine the transmission loss (TL) and absorption coefficient (Feng 2013). In the absence of additional microphones downstream of the specimen, a sound meter could be used instead to measure the TL of the specimen under test. However, the sound meter picks up discrete transmitted signals at periodic interval, which could result in a mismatch with the generated signals from the source.

In Fig. 7.3, a novel approach to measuring the TL is proposed using InTLM. The incident sound wave is absorbed by the specimen, transmitted through the specimen, and reflected since the rigid wall is shifted to the end of the impedance tube instead of at the back of the specimen. Thus, one would expect variations in the absorption coefficients as there is space behind the specimen for the sound waves to propagate through the specimen. The energy conservation would mean that the total acoustics pressures on both sides of the specimen would be the same as shown in Eq. (7.5a). Equation (7.5b) represents the new absorption coefficient in the absence of the rigid wall backing behind the specimen.

$$E_I = E_{R2} + E_T + E_{\alpha 2} \tag{7.5a}$$

$$\alpha_2 = 1 - |R_2|^2 - |T_r|^2 \tag{7.5b}$$

Subtracting Eq. (7.4) from Eq. (7.5b), an inferred expression for transmission coefficient can be derived without the use of 4-microphone setup.

$$\alpha_2 - \alpha_1 = 1 - |R_2|^2 - |T_r|^2 - (1 - |R_1|^2)$$

$$|T_r|^2 = \left(|R_1|^2 - |R_2|^2\right) + (\alpha_1 - \alpha_2) \tag{7.6}$$

$$\mathrm{TL} = 10 \log_{10} |T_r|^2 \tag{7.7}$$

The expression in Eq. (7.6) shows that the 'Inferential Method' of determining transmission loss coefficient, $T_r$ is simply the sums of the difference between measured reflected coefficients and the absorption coefficients. It makes perfect sense since one would expect the reflected pressure and absorbed pressure to be lesser without the rigid wall. The change in values of the two terms would then be

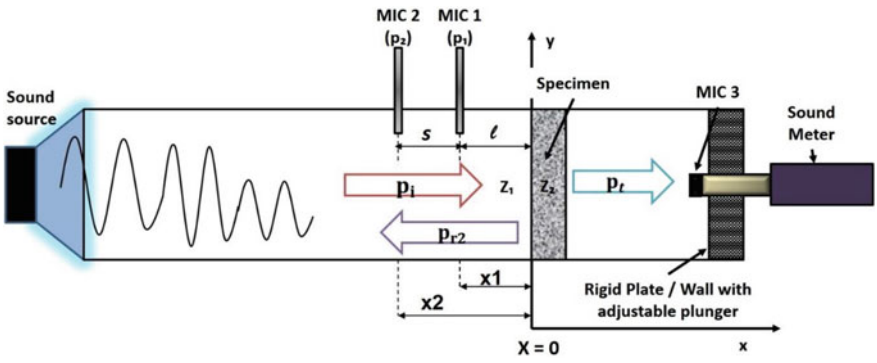


**Fig. 7.3** Schematic of 'InTLM' experimental setup for transmission loss measurement using 2-microphone and sound meter without the rigid wall backing

defined as TL as shown in Eq. (7.7). The word 'inferential' often appears in the literature across many fields of research. However, it should not be confused with the works of Xiang et al. (Robinson and Xiang 2010; Azevedo et al. 2011; Botts and Xiang 2012; Fackler et al. 2012; Henderson et al. 2013) that were developed from Bayesian-model-based framework to determine the conditional probabilities co-relating theory with new and supporting evidences.

### 7.2.3 Sound Meter Measurements

In order to validate the accuracy of the TL determined via 'InTLM', a sound meter is utilized during the experiments. The adjustable plunger was removed and a sound meter is placed at the end cap. The sound meter is turned on concurrently together with the impedance tube measurements. The sound meter captures the noise level detected at a distance of 200 mm from the specimen. The impedance tube generates approximately 106.3 dB sound waves. The difference in the values between the sound meter and the source is the transmission loss. However, the sound meter captures discrete data periodically at 20 ms. However, the data may not match the frequencies generated by the impedance tube, which are from 50 to 1600 Hz for the large tube. Thus, the most practical way of validating the results is to compare the average TL between the sound meter and the 'InTLM'.

## 7.3 Silica Aerogel Granules Optimization

Table 7.1 shows the classification, sample distribution, and their physical properties for each granule size. Figure 7.4 shows how the silica aerogel granules are prepared for the experiment. First, the acoustics absorption of an appropriate thin porous ply is evaluated. Then, silica aerogel granules of various sizes are filled in the impedance tube to the depths of 10 and 15 mm covered with a layer of porous ply held

**Table 7.1** Classification and physical properties of silica aerogel granules sizes

| Classification | Size range | Median | Density | Distribution | Aspect ratio |
|---|---|---|---|---|---|
| | $d$ (mm) | $d$ (cm) | $\rho$ (g/cm$^3$) | (%) | |
| AG1 | $0.50 \le x < 1.00$ | 0.075 | 0.0682 | 2.10 | 1.98 |
| AG2 | $1.00 \le x < 1.40$ | 0.12 | 0.0693 | 7.01 | 1.39 |
| AG3 | $1.40 \le x < 2.00$ | 0.17 | 0.0719 | 63.15 | 1.42 |
| AG4 | $2.00 \le x < 2.36$ | 0.218 | 0.0727 | 19.69 | 1.18 |
| AG5 | $2.36 \le x < 2.8$ | 0.258 | 0.0732 | 5.96 | 1.18 |
| AG6 | $2.8 \le x < 3.35$ | 0.307 | 0.0748 | 1.22 | 1.19 |
| AGMX | $0.10 < x \le 4.0$ | 0.200 | 0.0723 | 100.0 | 1.35 |

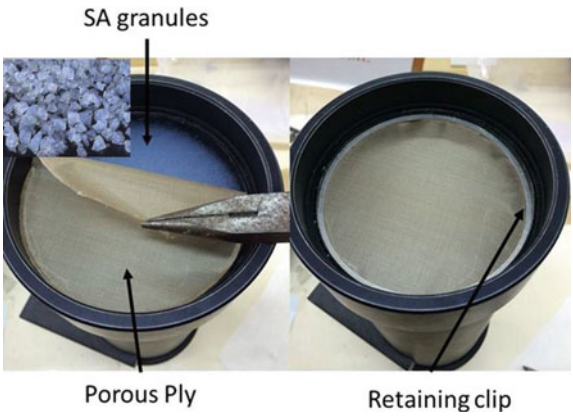


**Fig. 7.4** Filling of silica aerogel granules in impedance tube

using a retaining clip. The absorption coefficients of different silica aerogel granules with the porous ply are determined. Three measurements for each depth size are taken. The average measurement is then subtracted from the porous ply results to give the absorption coefficient of the granules as plotted in Fig. 7.5.

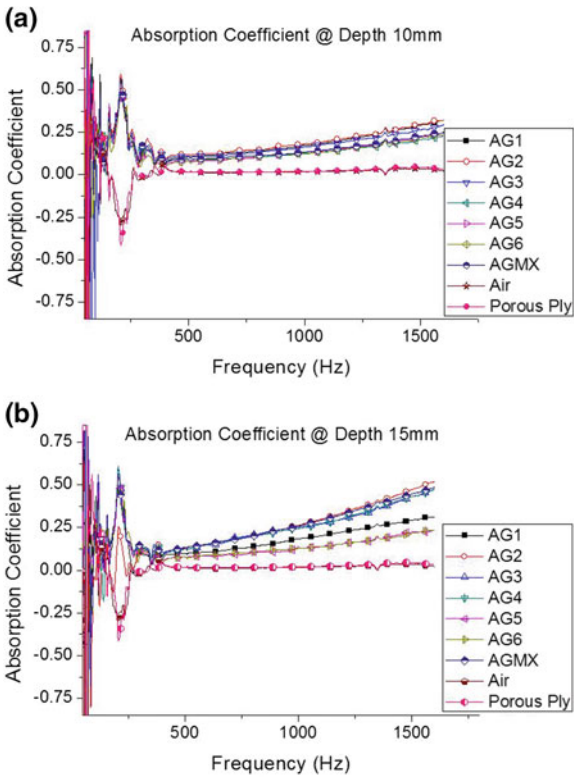


**Fig. 7.5** Sound absorption coefficient of silica aerogel granules (**a**) at 10 mm depth and (**b**) at 15 mm depth

The two-microphone impedance tube determines the ratio of absorption coefficient and complex reflection coefficient based on the transfer function between the two microphones. The integrated PULSE software that calculates the various data ensures that the sum of the two coefficients shall always conform to unity. The plots in Fig. 7.5b show that AG2 and AG3 have the best absorption coefficients of 0.52 and 0.48, respectively, compared to the other sizes when measured at 15 mm thickness. The absorption coefficients lowered to 0.32 and 0.29, respectively, when the thickness is reduced to 10 mm as shown in Fig. 7.5a. Naturally it can be seen that mixed granules, AGMX, for which 70 % of the composition come from the two sizes mentioned, has an absorption coefficient that is close to both the 1.2 and 1.7 mm sizes. The porous ply shows negligible absorption similar to air. Table 7.2 lists the absorption coefficients abstracted from Fig. 7.5 at the center and maximum frequency.

The absorption coefficient values at low frequencies from 50 to 200 Hz show erratic response for all the granule sizes. One possible reason is that the superpositions of incident and reflected waves at very low frequencies create a region of maximum particle velocity. This usually occurs at ¼ wavelength and it is common practice among acoustics engineers who design noise attenuation panels.

For a porous material like silica aerogel, absorption is achieved by impeding the air particle movement or vibrations and it is most effective in the region of the wave with the maximum particle velocity. Thus, the minimum thickness is inversely proportional to frequency and can be written as $\Lambda = \frac{c_{\max}}{4\text{freq}}$. This equation suggests that for a frequency of 200 Hz, a minimum thickness of 40 cm is required to absorb the noise. On the contrary, the minimum thickness is approximately 5.2 cm for higher frequency at 1600 Hz. However, Fig. 7.5a, b shows similar behavior from 200 to 250 Hz where all the granules had one distinct peak before declining, which is analogous to Helmholtz resonators where the pressure perturbations at the neck produce large velocities into pores of the aerogel granules. These large velocities in a narrow passage result in considerable viscous dissipation, producing high attenuation experiencing resonance (Dowling and Williams 1983; Kim 2010a, b).

**Table 7.2** Absorption coefficient of silica aerogel granules, air, and porous ply

| Classification | Absorption coefficient (10 mm) | | Absorption coefficient (15 mm) | |
|---|---|---|---|---|
| | 800 Hz | 1600 Hz | 800 Hz | 1600 Hz |
| AG1 | 0.14 | 0.31 | 0.14 | 0.31 |
| AG2 | 0.14 | 0.32 | 0.20 | 0.52 |
| AG3 | 0.14 | 0.29 | 0.21 | 0.48 |
| AG4 | 0.10 | 0.23 | 0.20 | 0.47 |
| AG5 | 0.10 | 0.25 | 0.10 | 0.24 |
| AG6 | 0.11 | 0.24 | 0.11 | 0.24 |
| AGMX | 0.11 | 0.25 | 0.20 | 0.48 |
| Air | 0.00 | 0.00 | 0.00 | 0.00 |
| Porous ply | 0.01 | 0.01 | 0.01 | 0.01 |

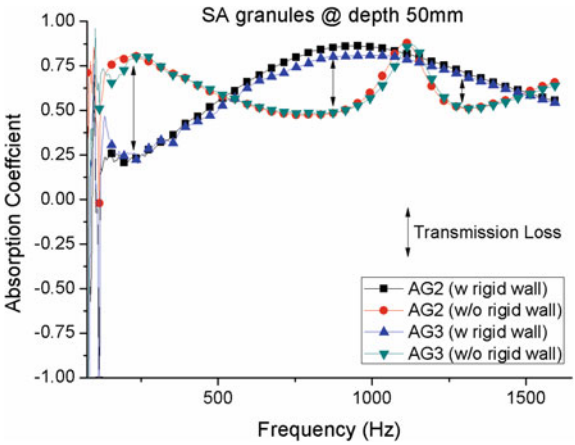


**Fig. 7.6** Comparison of AG2 and AG3 granules' absorption coefficients @ 50 mm thickness (with and without rigid wall)

The aerogel granules tested have pore sizes in the range of 20 nm. However, the absorption coefficients are varied across the various granule sizes. The absorption coefficient tends to decrease with increase in granule size. The larger granules, AG4 to AG6, registered low absorption coefficients than AG1 to AG3. There is greater amount of space and void between the larger granules for the same volume, which leads to lower acoustic attenuation and is another reason for the behavior shown in Fig. 7.5. The best absorbing silica aerogel granules of 1.2 and 1.7 mm (AG2 and AG3) with specimen thickness of 5 cm are further evaluated for the ¼ wavelength theory for optimization. The absorption coefficients and regions of transmission loss of AG2 and AG3 granules of 5 cm thickness are plotted in Fig. 7.6 according to the experimental setup in Figs. 7.2 (with rigid wall) and 7.3 (without rigid wall). The absorption coefficient between the two granule sizes is marginal with 1.2 mm granule size having better response, but showed similar response peaks (with rigid wall) peaked at 980 Hz with values of 0.86 and 0.81 for 1.2 and 1.7 mm granules respectively. Likewise, the responses from both granules are also similar when the rigid wall is shifted.

### *7.3.1 Transmission Loss of Silica Aerogel Granules*

The absorption coefficient, when tested without the rigid wall, peaked at low frequencies from 100 to 300 Hz for both the AG2 and AG3 granules, suggesting part of pressure wave have been transmitted as loss. Between 300 and 950 Hz, the absorption coefficient begins to decrease, indicating that more waves are being reflected. However, on the contrary, the absorption coefficient with rigid wall is seen increasing for the same range. Again, the difference in the responses shows that transmission loss is evident. Similarly, the difference in complex reflection

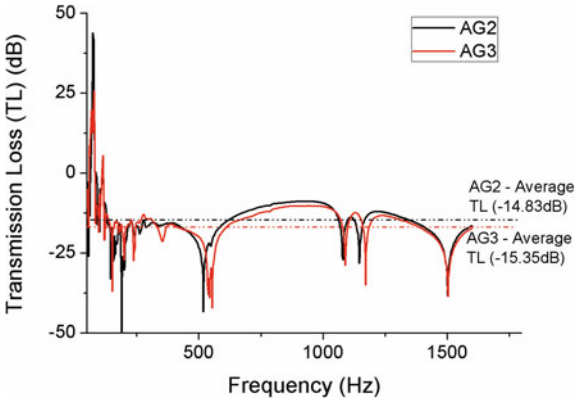


**Fig. 7.7** Evaluation of TL for AG2 and AG3 via proposed 'inferential method' using 2-microphone impedance tube

coefficient, although small, also contributes to the ratio of transmission loss. The absorption coefficient of the granules generally stabilized at lower frequencies with increasing thickness. However, increase of thickness does not necessarily increase the absorption at higher frequencies (>1000 Hz), where decline is observed for both AG2 and AG3 granules compared to Fig. 7.5.

The proposed 'InTLM' from Eqs. (7.6) and (7.7) is used to determine the transmission loss (TL) of the two aerogel granules, as shown in Fig. 7.7. The average TL for AG2 and AG3 granules is −14.83 and −15.35 dB respectively. The 'Inferential Method' results showed similar findings reported by Forest et al. (2001), who presented that the TL is lowered by 15 dB for frequency range from 300 to 1700 Hz for silica aerogel granules. The granules in Fig. 7.7 show TL having several down-peaks for frequencies up to 500 Hz. The TL starts to reduce from 500 to 1100 Hz which corresponds to the increase in absorption and reflection coefficients as shown in Fig. 7.6. Subsequently, the granules experienced another two down-peaks for frequencies above 1100 Hz. Based on the results obtained in Figs. 7.6 and 7.7, the AG2 and AG3 granules are selected to fabricate the GSA composite to determine the variations in the absorption coefficient and transmission loss.

## 7.4 Acoustic Performance GSA–SDS Composites and Other Materials

GSA–SDS and GSA–SDS/FMWNT specimens of 100 and 29 mm diameter in varying thicknesses are fabricated via FD method described in the same manner as previously reported (Mahesh and Joshi 2015) comprising of 1.2 and 1.7 mm silica aerogel granule sizes (GSA-AG2 and GSA-AG3) as shown in Table 7.3.

**Table 7.3** Overview of specimens tested

| Type | Specimen diameter (mm) | Granule size (mm) | No of layers | Thickness (mm) |
|---|---|---|---|---|
| GSA-SDS | 100 | 1.2 | 1 | 5 |
| | | | 1 | 10 |
| | | | 1 | 15 |
| | | | 4 | 40 |
| | | 1.7 | 1 | 5 |
| | | | 1 | 10 |
| | | | 1 | 15 |
| | | | 4 | 40 |
| | 29 | 1.7 | 1 | 20 |
| | | | 1 | 30 |
| | | | 1 | 40 |
| GSA-SDS/FMWNT | 100 | 1.7 | 1 | 10 |
| | | | 1 | 15 |
| | 29 | 1.7 | 1 | 20 |
| | | | 1 | 40 |
| Gray sponge | 100 | NA | 1 | 15 |
| Arylic | | | 1 | 15 |
| Magnesite | | | 1 | 15 |

The composition of GSA–SDS specimen is 20 wt% gelatin; 80 wt% silica aerogels; 0.56 wt% SDS as shown in Fig. 7.7. The composition of GSA–SDS/FMWNT is the same as above with the addition of 0.025 wt%. In addition, other materials were also tested for comparative analysis. In addition, other materials were also tested for comparative analysis. The preparation for the acoustic measurements for GSA–SDS specimens is the same as granules described in the above paragraph.

### *7.4.1 GSA–SDS*

The acoustic absorption coefficients and the TL of the GSA–SDS composites under various configurations are shown in Table 7.4.

Figure 7.8 shows the absorption coefficients of GSA–SDS for the silica aerogel granule size and thickness range listed in Table 7.4. The absorption coefficients for GSA-AG3 show better response than GSA-AG2. Interestingly, the response reported earlier in terms of aerogel granules was the reverse. The GSA-AG3-T15 composites show better absorption at lower frequencies than the GSA-AG2-T15 blocks. It steadily rises to a maximum of 0.6 from 1300 to 1450 Hz before declining

**Table 7.4** Densities, absorption coefficient and transmission loss of GSA-SDS composites

| Granule size (mm) | No of Layers | Thickness, $T$ (mm) | Frequency (Hz) | Absorption coefficient | Transmission loss (dB) | TL (avg) (dB) | Sound meter TL (avg) (dB) |
|---|---|---|---|---|---|---|---|
| GSA-AG2 (1.2 mm) | 1 | 5 | 800/1600 | 0.11/0.29 | −26.0/−11.2 | −11.3 | −11.0 |
| | 1 | 10 | 800/1600 | 0.14/0.41 | −12.0/−15.5 | −11.7 | −12.8 |
| | 1 | 15 | 800/1600 | 0.22/0.43 | −15.2/−12.6 | −14.6 | −11.3 |
| | 4 | 40 | 800/1600 | 0.61/0.28 | −15.7/−18.6 | −16.4 | −15.2 |
| GSA-AG3 (1.7 mm) | 1 | 5 | 800/1600 | 0.10/0.34 | −16.1/−12.5 | −10.7 | −10.9 |
| | 1 | 10 | 800/1600 | 0.17/0.49 | −16.9/−13.3 | −11.8 | −12.6 |
| | 1 | 15 | 800/1600 | 0.36/0.57 | −11.4/−15.8 | −14.5 | −13.3 |
| | 4 | 40 | 800/1600 | 0.43/0.42 | −33.0/−42.9 | −20.3 | −18.6 |
| GSA-AG3 (1.7 mm) | 1 | 20 | 3200/6400 | 0.29/0.43 | −19.2/−19.4 | −22.5 | −15.5 |
| | 1 | 30 | 3200/6400 | 0.42/0.52 | −18.1/−20.1 | −24.5 | −19.9 |
| | 1 | 40 | 3200/6400 | 0.45/0.62 | −23.5/−25.0 | −25.4 | −15.2 |

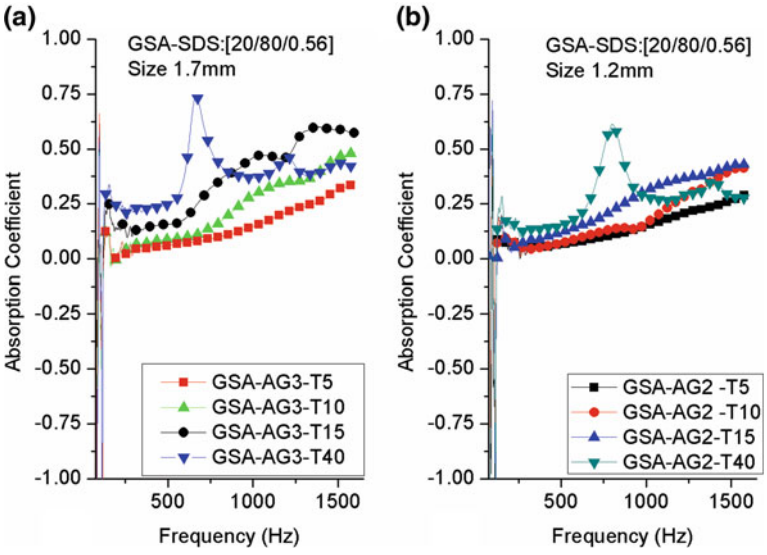


**Fig. 7.8** Absorption coefficients for GSA–SDS composites thickness T5-T40 (**a**) size 1.7 mm; (**b**) size 1.2 mm for frequency (50–1600 Hz)

to 0.57 at 1600 Hz. Generally, the GSA–SDS composites also showed better absorption for the same thickness at the center frequency and maximum frequency as compared to granules The variations in densities between the silica aerogel granules and GSA–SDS composites in general is in the negligible range between 0.003 and 0.005 g/cm$^3$ , suggesting that the gelatin network as a whole contributed to a very marginal increase to the overall density. Certainly, the gelatin foam that encompassed around the granules would have provided an additional tortuous path for the sound to travel by reducing the sizes of the voids between the granules and thus increase in the absorption coefficient.

The 4-layered GSA-SDS composites comprising the AG2 and AG3 with 40 mm depth are evaluated for absorption coefficient. The response of both the granules sizes is similar. However, the frequency at which the peak occurred is different. For the composites with AG3 granules, the maximum absorption of 0.74 occurred at 670 Hz. But, for the composites with AG2 granules, the maximum peak 0.61 resided at the centre frequency of 800 Hz. However, both the 4-layered composites showed a rapid rise from 500 to 800 Hz in absorption as shown in Fig. 7.8a, b, which is different from the granules that have a gradual slope from 500 to 1100 Hz.

The results showed an interesting behavior in the response between the single block layer and the 4-layered composite. The 4-layered GSA–SDS composites have better absorption at lower frequencies compared to the single GSA–SDS blocks and vice versa at higher frequencies. The TL for the GSA-AG2 and—AG3 composites is shown in Fig. 7.9. Generally, the average TL increases with increasing thickness

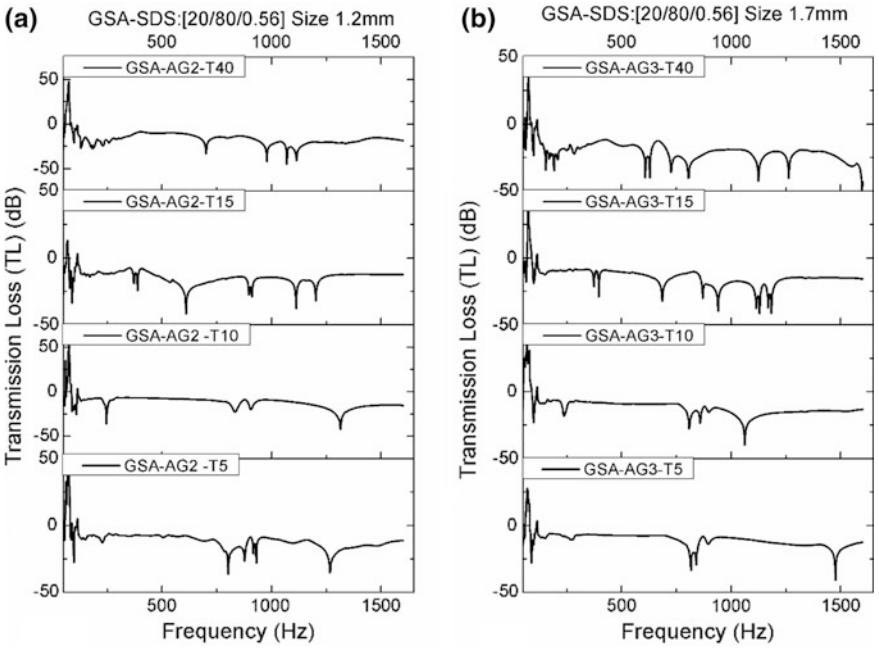


**Fig. 7.9** Transmission loss (TL) for GSA-AG2/AG3 composites thickness T5-T40 (**a**) size 1.2 mm; (**b**) size 1.7 mm

of the composites. As the thickness increases, more peaks start to appear with narrowing bands, especially the 4-layered GSA–SDS composites However, the GSA-AG2 and—AG3 composites of 10 mm thickness have showed better stability as there are lesser peaks than the rest. In terms of magnitude, there is not much difference between 1.2 and 1.7 mm granules and remains inconclusive as to which is better at reducing TL with the exception of the 4-layered GSA–SDS composite. The average TL is between −10.7 and −20.3 decibels (dB).

Smaller GSA–SDS specimens (29 mm diameter) comprising 1.7 mm aerogel granules are tested for acoustic performance in the small impedance tube for frequencies from 500 to 6400 Hz. The absorption coefficients and the TL in the higher frequency range are shown in Fig. 7.10a, b.

The absorption coefficients of GSA–SDS composites are reasonable high when evaluated at higher frequencies as shown in Fig. 7.10a. The peaks seem to concentrate around the region of 2300–2700 Hz for all the thicknesses tested. As expected, the increase in thickness resulted in higher absorption by the composites. The absorption coefficient for the GSA–SDS composites with 1.7 mm granules at 3200 Hz ranges from 0.29 to 0.45 and at 6400 Hz ranges from 0.43 to 0.62 respectively. The average TL at higher frequencies is between −22.5 and −25.4 dB which is higher than the larger specimens evaluated at lower frequencies.

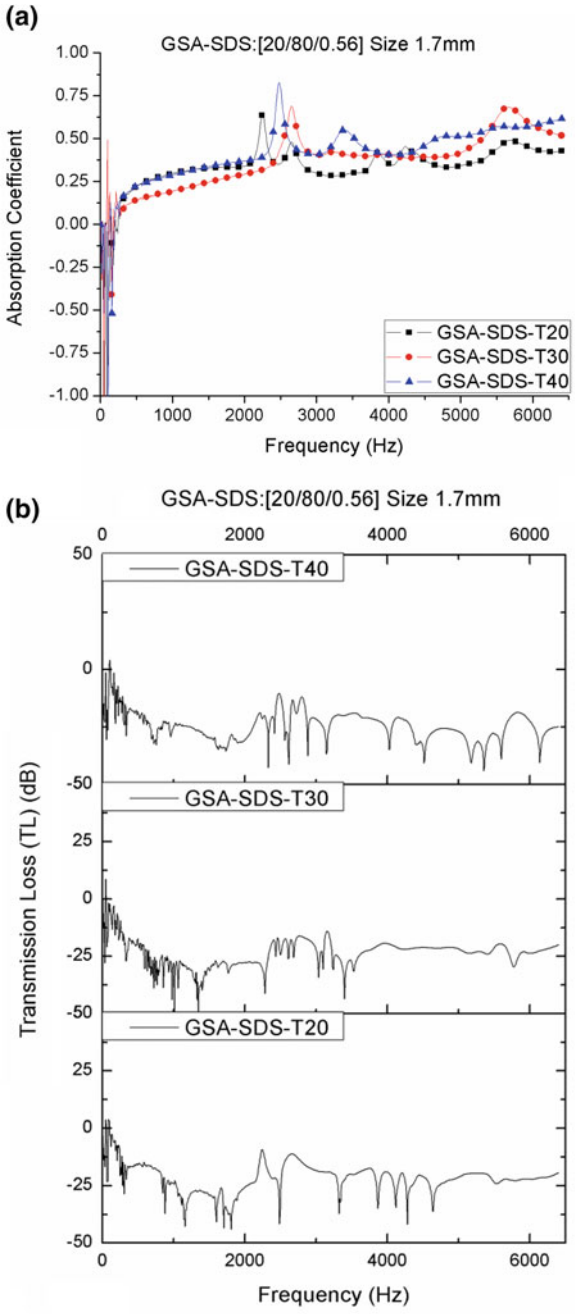


**Fig. 7.10** **a** Absorption coefficients; **b** transmission loss (TL) for GSA–SDS (size 1.7 mm) composites thickness T20-T40 @ frequency (500–6400 Hz)

### 7.4.2 GSA–SDS/FMWNT Composites

GSA–SDS/FWMNT composites comprising of 1.7 mm granules doped with 0.025 wt%. FMWNT were evaluated for acoustic performance. The main objective was to determine whether the addition of FMWNT enhance the absorption coefficient of the composites, similar to improving the thermal conductivity, strain recovery and hydrophobicity of composites. Table 7.5 shows the snapshot of the results obtained for absorption coefficient and TL of the GSA-SDS/FMWNT composites. The addition of FMWNT in the GSA-SDS composites shows contrasting response in the absorption coefficient in Fig. 7.11 for both the low and high frequency range. It can be observed from Fig. 7.11a that the absorption coefficients of the GSA–SDS/FMWNT composites are below that of GSA–SDS for lower frequency. But at higher frequencies, the absorption coefficients with FMWNT are drastically better than the GSA–SDS composites.

GSA–SDS/FMWNT composite of 20 mm thickness registered the maximum absorption of 0.84 at 2950 Hz while the 40 mm thick composite's maximum absorption is 0.85 at 2420 Hz. The observed shift in the absorption peak toward higher frequencies, as also noted in the previous figures of GSA–SDS composites could be attributed to the density variations of composites as suggested by Verdejo et al. (2009). A similar response was observed for low loadings of FMWNTs from 0.05 to 0.02 wt% as reported by Basirjafari et al. (2012), who reported increased absorption over the pure polyurethane foam. The human hearing is the most sensitive in the frequency from 2000 to 4000 Hz (Verdejo et al. 2009; Bandarian et al. 2011; Basirjafari et al. 2012) and thus GSA–SDS/FMWNT composites have shown to provide better acoustic damping than GSA–SDS composites. The possible increase in the acoustic absorption could be due to two possible reasons; (a) additional micro-voids generated due to presence of well-dispersed FMWNTs that lead to the increase in tortuous paths and (b) damping of the elastic stress waves increases via propagation through the composite transforming them to thermal energy (Basirjafari et al. 2012). Tortuosity is influenced by the pore or the cell size. In the case of silica aerogel granules, which are nanomaterials, the pore size is the influencing factor. However, since the commercial grade of the granules has been used throughout in this research and experiments, pore size is one of the many variables that could not be controlled.

**Table 7.5** Absorption coefficient and transmission loss of GSA-SDS/FMWNT composites

| Size *d* (mm) | Diameter (mm) | Thickness (mm) | Frequency (Hz) | Absorption coefficient | Transmission loss (dB) | TL (avg) (dB) |
|---|---|---|---|---|---|---|
| 1.7 | 100 | 10 | 800/1600 | 0.22/0.37 | −11.7/−10.1 | −12.3 |
| | | 15 | 800/1600 | 0.33/0.36 | −9.8/−12.5 | −12.4 |
| 1.7 | 29 | 20 | 3200/6400 | 0.69/0.75 | −16.5/−28.8 | −19.6 |
| | | 40 | 3200/6400 | 0.42/0.63 | −18.6/−11.2 | −17.4 |

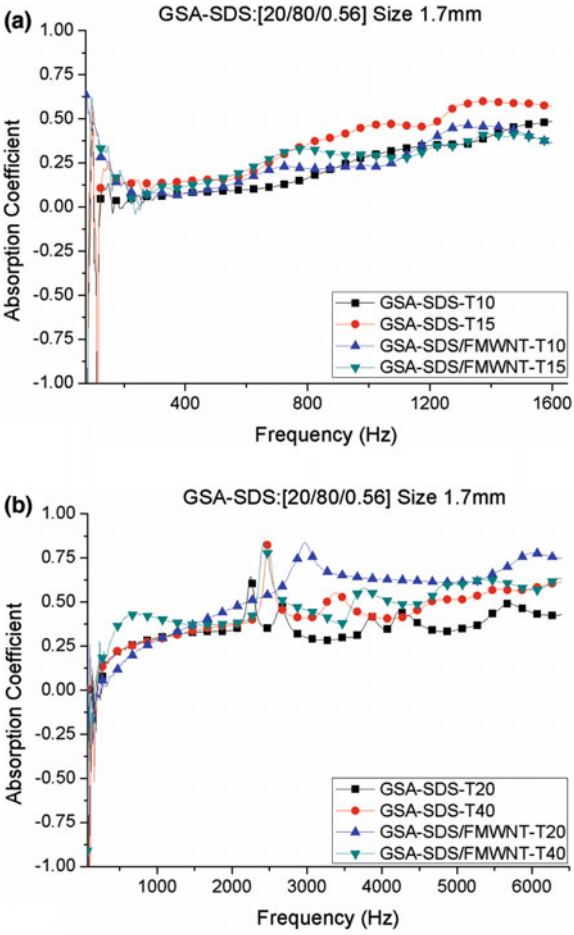


**Fig. 7.11** Absorption coefficient for GSA-SDS/FMWNT (size 1.7 mm; 0.025 wt% FMWNT) composites (**a**) T10-T15 @ 50–1600 Hz; (**b**) T20-T40 @ 75–6400 Hz

Figure 7.12 shows the TL of the GSA–SDS/FMWNT composites of various thicknesses for both low and high frequency ranges. The trends look similar to the GSA–SDS composites but the transmission loss is lesser when compared pointing to the fact that composites with FMWNTs have better absorption at higher frequencies. The TL of a material is a measure of the material's ability to block sound or act as sound barriers. Sound barriers are usually dense and have high reflection. For a material that is light and porous, it is usually used as an acoustic absorber. The GSA–SDS and GSA–SDS/FMWNT composites tested thus far have shown the capacity to act as an acoustics absorber and barrier material displaying reasonable absorption at lower frequencies and blocking sound pressure waves at higher frequencies.

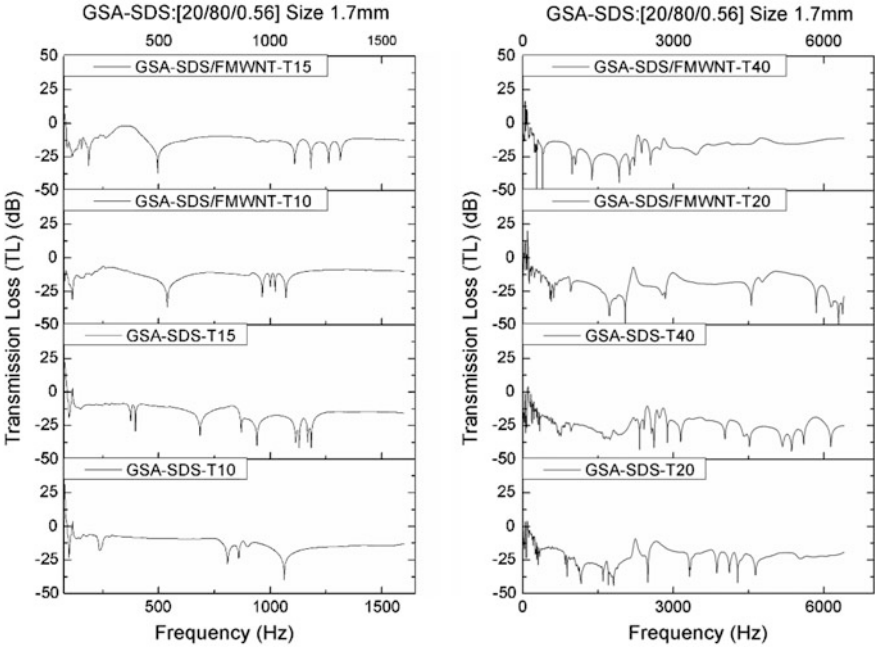


**Fig. 7.12** TL for GSA-SDS/FMWNT (size 1.7 mm; 0.025 wt% FMWNT) composites (**a**) T10-T15 @ 50–1600 Hz; (**b**) T20-T40 @ 75–6400 Hz

### *7.4.3 'InTLM' and Sound Meter*

The 'InTLM' derived values seem to be closer to the sound meter measured values for the 100 mm diameter disks with relative tolerance from −0.2 to −3.3 dB. However, for the smaller tube comprising of 29 mm disk the differences are greater from −4.6 to −10.2 dB compared to the sound meter values. One of the reasons could be the number of data points captured over the entire run, which last approximately 35 s. Given that the period of capturing one discrete data in sound meter is 20 ms, which effectively captures about 1750 discrete data over the entire run. Therefore, it is closer to the large tube setup for the frequency range up to 1600 Hz, assuming that one data captured per Hz in the impedance tube. However, the small tube measures the specimen up to 6400 Hz, which the sound meter is not able to generate more data points as 20 ms is the lowest selectable period. Thus, the 'Inferential Method' can be applied for specimens at the lower frequency range using the larger tube.

## 7.5 Comparative Analysis with Other Traditional Materials

The absorption coefficient of GSA-SDS composites were compared with other materials ranging from rigid and hard surface to porous and flexible foams. Figure 7.13a shows the materials evaluated for comparative analysis and Fig. 7.13b the absorption performance of the materials. The gray sponge and acrylic perspex are taken from the in-house laboratory. The magnesite wood wools are acquired from Hera design Inc., a company that produces acoustic panels. Three types were tested; (a) normal panel bonded with layers of 2 mm fiber wood wool, (b) same as (a) but coated with a layer of gray and smooth micro ceramic coating and (c) same as (a) but coated with a layer of white and rough micro ceramic coating.

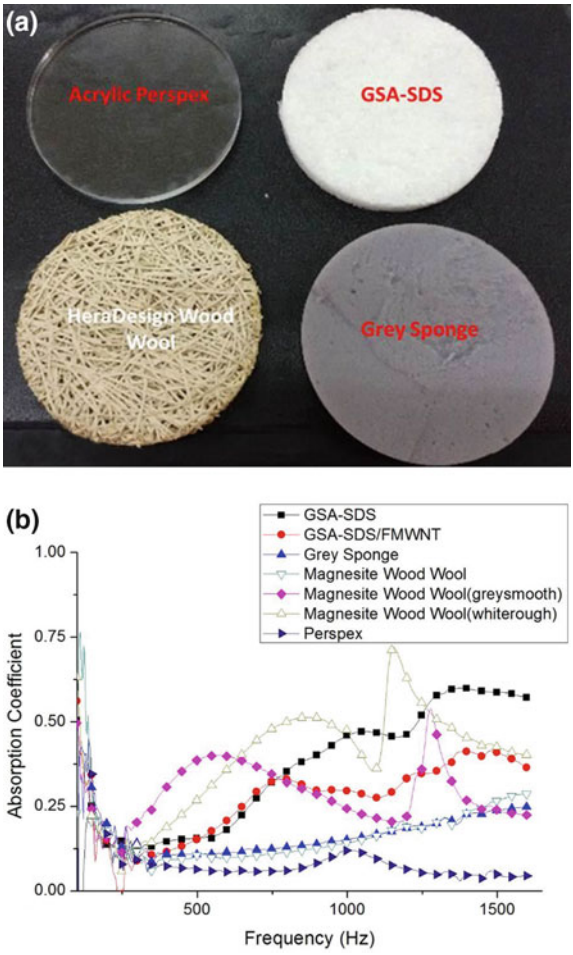


**Fig. 7.13** **a** Various types of materials tested. **b** Comparison of absorption coefficients of GSA–SDS with other materials for 15 mm thickness @ 50–1600 Hz

The GSA–SDS and GSA–SDS/FMWNT composites when compared with acrylic panel, gray sponge and the magnesite wood wool (normal) have superior acoustic absorption throughout the entire range of frequencies. However, when compared with the magnesite coated wood wools (gray/smooth and white/rough); the GSA–SDS-related composites were inferior at low frequencies from 300 to 750 Hz. After 750 Hz, only the white/rough magnesite wood wool showed better acoustic absorption up to 1150 Hz. Thereafter, the GSA-SDS exhibited superior performance until 1600 Hz. The micro-coating on the wood wool definitely enhanced their absorptive capacity at certain bandwidths as the micro-beads of the ceramic created a tortuous path as compared to the bigger gaps in normal ones. Similarly, if the pore size in the silica aerogel granules is reduced, debilitating the paths undertaken by the sound waves, the GSA–SDS composites would have better acoustic performance. In addition, if the addition pores induced in the gelatin network around the granules can be reduced or controlled, then chances of better absorption could be realized.

### 7.5.1 Acoustic Activity

Acoustic activity (Verdejo et al. 2009; Basirjafari et al. 2012) is defined as the area under the absorption curve normalized over the frequency range and is determined as shown in Eq. (7.8) where, $f_1$ is the lower frequency at 50 Hz and $f_2$ is the upper frequency at 1600 Hz.

$$\alpha_{\text{normalized}} = \frac{1}{(f_2 - f_1)} \int_{f_1}^{f_2} \alpha(f) \mathrm{d}f \tag{7.8}$$

The acoustic activity of the various material experimented in the preceding section has been determined and shown in Fig. 7.14. The results showed interesting revelation about the materials tested. The values would give a visible and quick identification on the best absorbing materials over the entire range of frequency to be operated. The GSA–SDS displayed the highest acoustic activity amongst the material tested and almost 45 % higher than GSA–SDS/FMWNT. The two magnesite coated wood wool are the next highest at approximately 0.5 and undoubtedly Perspex has the lowest acoustic activity. The values showed that GSA–SDS is the best option if one wants to use a material that is capable of maintaining high absorption in a wide frequency range. On the other hand, low acoustic activity with the addition of FMWNT once again supports the argument that they are not as promising for lower range frequencies.

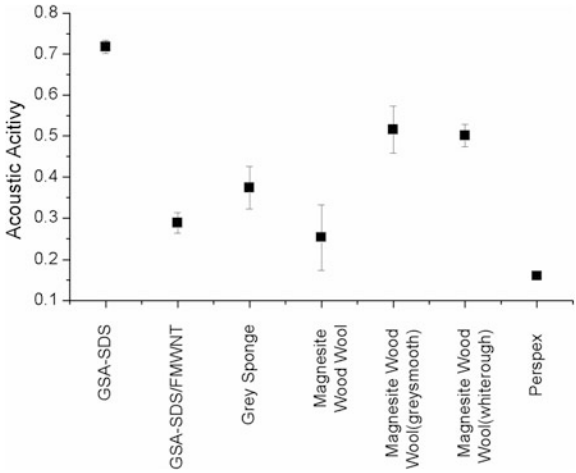


**Fig. 7.14** Normalized acoustic absorption coefficient (acoustic activity) of selected materials

## 7.6 Concluding Remarks

There are two key aspects to this acoustic study. First, a comparative study on the acoustic absorption coefficient and TL of aerogel granules of various sizes and GSA–SDS composite are evaluated at low frequency range from 50 to 1600 Hz. It was noted that AG2 and AG3 granules result in the best absorption coefficients peaking at 980 Hz with the values of 0.86 and 0.81 when tested with 5 cm depth with an average TL of −14.83 dB and −15.35 dB respectively. It was also noted that as a composite block, the GSA-AG3 composites have better absorption coefficient than GSA-AG2 for the same corresponding thickness reaching the peak of 0.6 from 1300 to 1450 Hz. Overall, the GSA–SDS composites with 10 mm thickness exhibited superior absorption over the granules and better stability in terms of TL. It was revealed that the 4-layered GSA-SDS composites configuration is suitable for acoustic absorption in narrow band application. The GSA–SDS composites comprising of silica aerogel granules are suitable for both as acoustic absorption and acoustic barrier material. In addition, the acoustic activity has shown that GSA–SDS have better absorption than other traditional materials over a wider range of frequencies.

The second aspect is the proposed novel 'Inferential Transmission Loss method' (InTLM) in determining TL using 2-microphone impedance tube. The approach is a modification to the usual transfer method that infers transmission coefficient with and without the rigid wall. The calculated results showed high accuracy from −0.2 to −3.2 dB compared with sound meter measurements. Thus, the 'InTLM' can be applied for 100 mm diameter specimens which use the large tube in estimating the TL without the need to use 4-microphone impedance tube

Most porous materials absorb incident and airborne sound waves well. A small change in pressure perturbations can generate loud noise, which dissipates into heat as it travels through the tortuous path in these materials. On the other hand,

absorbers are usually not good as acoustic insulators or barriers, a property that is directly related and proportional to the mass of the wall. The heavier the mass of a wall, the better it acts as a sound insulation, especially against airborne noise. However, GSA–SDS and GSA–SDS/FMWNT composites through the experiments, have shown to possess a balanced feature both as a sound absorber and a barrier despite being lightweight. This is significant especially in buildings where lightweight walls are designed for thermal insulation but not for sound insulation. GSA–SDS composites are able to fulfill both criteria to support both as an acoustic and thermal insulation material. Future works shall include in situ measurements and field experiments on GSA–SDS impregnated windows and wall panels.

## References

Azevedo, M.N., N. Xiang and C. Fackler. 2011. Low frequency absorption and attenuation of granular aerogel composites. 40th International Congress and exposition on noise control engineering 2011, INTER-NOISE 2011, INCEJ and ASJ, September 4–7, in Osaka, Japan.

Bandarian, M., A. Shojaei, and A.M. Rashidi. 2011. Thermal, mechanical and acoustic damping properties of flexible open-cell polyurethane/multi-walled carbon nanotube foams: effect of surface functionality of nanotubes. *Polymer International* 60(3): 475–482.

Basirjafari, S., R. Malekfar, and S. Esmaielzadeh Khadem. 2012. Low loading of carbon nanotubes to enhance acoustical properties of poly(ether)urethane foams. *Journal of Applied Physics* 112(10): 104312.

Bheekhun, N., A.R. Abu Talib, and M.R. Hassan. 2013. Aerogels in aerospace: an overview. *Advances in Materials Science and Engineering* 2013: 18.

Botts, J., and N. Xiang. 2012. Bayesian inference for acoustic impedance boundaries in room-acoustic finite difference time-domain modeling. *AIP Conference Proceedings* 1443(1): 306–313.

Buratti, C., and E. Moretti. 2013. 10—Silica nanogel for energy-efficient windows. In *Nanotechnology in Eco-Efficient Construction,* eds. F. Pacheco-Torgal, M.V. Diamanti, A. Nazari and C.G. Granqvist, 207–235. Cambridge: Woodhead Publishing.

Caponi, S., G. Carini, G. D'Angelo, A. Fontana, O. Pilla, F. Rossi, F. Terki, G. Tripodo, and T. Woignier. 2004. Acoustic and thermal properties of silica aerogels and xerogels. *Physical Review B* 70(21): 214204.

Cotana, F., A.L. Pisello, E. Moretti, and C. Buratti. 2014. Multipurpose characterization of glazing systems with silica aerogel: In-field experimental analysis of thermal-energy, lighting and acoustic performance. *Building and Environment* 81: 92–102.

Dowling, A.P., and J.E.F. Williams. 1983. *Sound and Sources of Sound.* Chichester: E. Horwood.

Fackler, C., N. Xiang, G. Churu, D.P. Mohite, N. Leventis, C. Sotiriou-Leventis and H. Lu. 2012. Experimental investigation of the acoustic attenuation by monolithic polyurea aerogels. 41st International Congress and Exposition on Noise Control Engineering 2012, INTER-NOISE 2012, August 19–22. New York: Institute of Noise Control Engineering of the USA.

Feng, L. 2013. Modified impedance tube measurements and energy dissipation inside absorptive materials. *Applied Acoustics* 74(12): 1480–1485.

Forest, L., V. Gibiat, and A. Hooley. 2001. Impedance matching and acoustic absorption in granular layers of silica aerogels. *Journal of Non-Crystalline Solids* 285(1–3): 230–235.

Forest, L., V. Gibiat, and T. Woignier. 1998. Evolution of the acoustical properties of silica alcogels during their formation. *Ultrasonics* 36(1–5): 477–481.

Fricke, J., and G. Reichenauer. 2011. Thermal. acoustical and structural properties of silica aerogels. In *MRS Proceedings.* Vol. 73.

Gross, J., J. Fricke, and L.W. Hrubesh. 1992. Sound-propagation in $Sio_2$ aerogels. *Journal of the Acoustical Society of America* 91(4): 2004–2006.

Henderson, W., P. Goggans, N. Xiang, and J. Botts. 2013. Bayesian inference approach to room-acoustic modal analysis. *AIP Conference Proceedings* 1553(1): 38–45.

International, A. 2012. ASTM E1050-12, Standard Test Method for Impedance and Absorption of Acoustical Materials Using a Tube, Two Microphones and a Digital Frequency Analysis System. West Conshohocken: ASTM International.

Kim, Y.-H. 2010a. *Acoustic Wave Equation and Its Basic Physical Measures. Sound Propagation*, 69–128. NJ: John Wiley & Sons, Ltd.

Kim, Y.-H. 2010b. *Vibration and Waves. Sound Propagation*, 1–68. NJ: John Wiley & Sons, Ltd.

Mahesh, S., and S.C. Joshi. 2015. Thermal conductivity variations with composition of gelatin-silica aerogel-sodium dodecyl sulfate with functionalized multi-walled carbon nanotube doping in their composites. *International Journal of Heat and Mass Transfer* 87: 606–615.

Palumbo, D.L., M.G. Jones, and J. Klos. 2004. Improvements to the two-thickness method for derviring acoustic properties of materials. NOISE Conference. Baltimore: National Technical Information Service.

Riffat, S.B., and G. Qiu. 2013. A review of state-of-the-art aerogel applications in buildings. *International Journal of Low-Carbon Technologies* 8(1): 1–6.

Robinson, P., and N. Xiang. 2010. On the subtraction method for in-situ reflection and diffusion coefficient measurements. *The Journal of the Acoustical Society of America* 127(3): EL99–EL104.

Sachithanadam, M., and S.C. Joshi. 2013. High strain recovery with improved mechanical properties of gelatin–silica aerogel composites post-binding treatment. *Journal of Materials Science* 49(1): 163–179.

Sachithanadam, M., and S.C. Joshi. 2014. A new phenomenon of compressive strain recovery in gelatin-silica aerogel composites with SDS. *Procedia Engineering* 75: 51–55.

Smith, C.D., and T.L. Parrott. 1983. Comparison of three methods for measuring acoustic properties of bulk materials. *The Journal of the Acoustical Society of America* 74(5): 1577–1582.

Sung Soo, J., K. Yong Tae, L. Yong Bong, C. Seung Il, and L. Jong Kyu. 2008. Measurement of sound transmission loss by using impedance tubes. *Journal of the Korean Physical Society* 53(2): 596–600.

Verdejo, R., R. Stämpfli, M. Alvarez-Lainez, S. Mourad, M.A. Rodriguez-Perez, P.A. Brühwiler, and M. Shaffer. 2009. Enhanced acoustic damping in flexible polyurethane foams filled with carbon nanotubes. *Composites Science and Technology* 69(10): 1564–1569.

Vigran, T.E. 2012. Normal incidence sound transmission loss in impedance tube—measurement and prediction methods using perforated plates. *Applied Acoustics* 73(4): 454–459.

# Appendix
# Useful MATLAB Codes

## Strain Recovery

```
GCpercent=({'0%<C<10%' '10%<C<20%' '20%<C<30%' '30%<C<40%'
'40%<C<50%' '50%<C<60%' '60%<C<70%'});
boxplot(GCpercent,Cpercent)
boxplot(Cpercent,GCpercent)
GCSpercent=repmat({'0%<C<10%' '10%<C<20%' '20%<C<30%' '30%<C<40%'
'40%<C<50%' '50%<C<60%' '60%<C<70%'},1,3);
SDS = [repmat({'S-0%'},1,7),repmat({'S-0.33%'},1,7),repmat({'S-
0.67%'},1,7)];
SDS = [repmat({'S-0%'},1,5),repmat({'S-0.33%'},1,5),repmat({'S-
0.67%'},1,5)];
SDSpercent = [repmat({'S-0%'},1,7),repmat({'S-
0.33%'},1,7),repmat({'S-0.67%'},1,7)];
boxplot(Cpercent,{GCSpercent,SDSpercent},'colors',repmat('rbg',1,7
),'factorgap',[5 2],'labelverbosity','minor');
GCSpercent=repmat({'0%<C<20%' '20%<C<30%' '30%<C<40%' '40%<C<50%'
'50%<C<60%' '60%<C<70%'},1,3);
SDSpercent = [repmat({'S-0%'},1,6),repmat({'S-
0.33%'},1,6),repmat({'S-0.67%'},1,6)];
boxplot(Cpercent,{GCSpercent,SDSpercent},'colors',repmat('rbg',1,6
),'factorgap',[5 2],'labelverbosity','minor');
GCSpercent1=repmat({'0%<C<20%' '20%<C<40%' '40%<C<60%'
'60%<C<70%'},1,5);
GRpercent =
[repmat({'0.05G'},1,4),repmat({'0.10G'},1,4),repmat({'0.20G'},1,4)
,repmat({'0.30G'},1,4),repmat({'0.50G'},1,4)];
boxplot(Cpercent1,{GCSpercent1,GRpercent},'colors',repmat('rbg',1,
4),'factorgap',[5 2],'labelverbosity','minor');
boxplot(Cpercent1,{GCSpercent1,GRpercent},'colors',repmat('rbgyw',
1,4),'factorgap',[5 2],'labelverbosity','minor');
boxplot(Cpercent1,{GCSpercent1,GRpercent},'colors',repmat('rbgybl'
,1,4),'factorgap',[5 2],'labelverbosity','minor');
boxplot(Cpercent1,{GCSpercent1,GRpercent},'colors',repmat('rbgyo',
1,4),'factorgap',[5 2],'labelverbosity','minor');
boxplot(Cpercent1,{GCSpercent1,GRpercent},'colors',repmat('rbgyb',
1,4),'factorgap',[5 2],'labelverbosity' 'minor');
```



M. Sachithanadam and S.C. Joshi, *Silica Aerogel Composites*,
Engineering Materials, DOI 10.1007/978-981-10-0440-7

```
                                                    ,
boxplot(Cpercent1,{GCSpercent1,GRpercent},'colors',repmat('rbgyv',
1,4),'factorgap',[5 2],'labelverbosity','minor');
boxplot(Cpercent1,{GCSpercent1,GRpercent},'colors',repmat('rbgy',1
,4),'factorgap',[5 2],'labelverbosity','minor');
GRpercent=repmat({'0.05G' '0.10G' '0.20G' '0.30G' '0.50G'},1,4);
GRpercent =
[repmat({'0%<C<20%'},1,5),repmat({'20%<C<40%'},1,5),repmat({'40%<C
<60%'},1,5),repmat({'60%<C<70%'},1,5)];
GRpercent=repmat({'0.05G' '0.10G' '0.20G' '0.30G' '0.50G'},1,4);
GCSpercent1 =
[repmat({'0%<C<20%'},1,5),repmat({'20%<C<40%'},1,5),repmat({'40%<C
<60%'},1,5),repmat({'60%<C<70%'},1,5)];
boxplot(Cpercent1,{GRpercent,GCSpercent1},'colors',repmat('rbgy',1
,5),'factorgap',[5 2],'labelverbosity','minor');
GCSpercent1 = [repmat({'0-20%'},1,5),repmat({'20-
40%'},1,5),repmat({'40-60%'},1,5),repmat({'60-70%'},1,5)];
boxplot(Cpercent1,{GRpercent,GCSpercent1},'colors',repmat('rbgy',1
,5),'factorgap',[5 2],'labelverbosity','minor');
```

# ANOVA

```
Gelatin1=repmat(1:3,12,2)
SDS1=repmat(1:4,3,6)
Compression1=[ones(1,24);2*ones(1,24);3*ones(1,24)]
load strainrecovery
strainrecovery=strainrecovery(:);
Gelatin1=Gelatin1(:);
SDS1=SDS1(:);
Compression1=Compression1(:);
[strainrecovery Gelatin1 SDS1 Compression1]
varnames={'Gelatin';'SDS';'Compression'};
anovan(strainrecovery,{Gelatin1 SDS1 Compression1},3,3,varnames)
[pvals,tbl,stats] = anovan(strainrecovery,{Gelatin1 SDS1
Compression1},'model',2,'random',1,varnames);

%SDS-Gelatin (4mm)
Gelatin3=repmat(1:3,4,2)
SDS3=[ones(1,6);2*ones(1,6);3*ones(1,6);4*ones(1,6)]
varnames={'Gelatin' 'SDS'}
load strainrecovery3
strainrecovery3=strainrecovery3(:);
Gelatin3=Gelatin3(:);
SDS3=SDS3(:);
[strainrecovery3 Gelatin3 SDS3]
[pvals,tbl,stats] = anovan(strainrecovery3,{Gelatin3
SDS3},3,3,varnames);
 [h,atab,ctab,stats] = aoctool(Gelatin3,strainrecovery3,SDS3);
multcompare(stats,0.05,'on','','s')
```

# Index





M. Sachithanadam and S.C. Joshi, *Silica Aerogel Composites*,
Engineering Materials, DOI 10.1007/978-981-10-0440-7